

AN ABSTRACT OF THE DISSERTATION OF

Hamutcuoglu Osman Murat for the degree of Doctor of Philosophy in
Civil Engineering presented on May 3, 2010.

Title: Parametric Uncertainties in Reliability Analysis of Bridge Structures

Abstract approved: _____

Michael H. Scott

Probability-based reliability methods have placed an increased emphasis on realistic simulation of structural behavior in bridge engineering. Uncertainty is present in every aspect of structural analysis. Aleatory uncertainties in the loading and load-carrying capacities, and epistemic uncertainties in mathematical idealization of bridge systems are the major contributors to uncertain structural response. However, the range of possible response and resistance of bridge components can be predicted in probabilistic means.

The objective of this study is to develop efficient reliability analysis methods for bridge components using existing concepts of probability, structural reliability and finite element analysis. A finite element reliability procedure is proposed to evaluate the probability of failure while accounting for both aleatory and epistemic uncertainties in bridge girders subjected to live loads as well as columns to extreme seismic loadings. OpenSees, the Open System for Earthquake Engineering Simulation, an object-oriented open source framework for finite element analysis, is used to implement in the proposed methodology.

For this probabilistic analysis approach, a gradient based first order reliability method (FORM) that provides importance measures of uncertain parameters is used instead of approximate integral solutions such as Monte-Carlo simulations. The uncertain parameters are treated as random variables with continuous probability density functions. The random variables are ranked to determine which parameters have the most influence on the structural response to applied loadings.

Force-based elements whose integration points coincide with critical locations are ideal for moving load simulations of bridge girders. Moving vehicle loads are taken into account as the part of the element, rather than nodal, equilibrium equations and it is straightforward to link section forces to a constitutive model rather than relying on rigid body equilibrium. However, FORM requires explicit formulations for the derivative of the structural response to be obtained with respect to each uncertain parameter. For sensitivity formulations in force-based finite elements, the direct differentiation method (DDM) is adopted in the framework for evaluating the function and its gradient at the same precision. The numerical examples verify DDM response sensitivity equations are correct and reliability analysis setup is prepared for continuous reinforced concrete bridge girders.

As a unique contribution to the reliability assessments of bridge girders, the interaction of moment and shear is considered on both the demand and resisting sides of the limit state function. A new material model based on Modified Compression Field Theory (MCFT) is implemented in OpenSees to represent moment-shear interaction. For performance limits placed on girder members, the moment-shear capacity is defined using a multi-line closed curve adapted from the AASHTO design code implementation of MCFT.

To contribute safety measurements of bridge girders, the framework runs fully

probabilistic reliability analyses while treating aleatory and epistemic uncertainties simultaneously. Sensitivity formulations for new implementations in the proposed methodology is another important contribution to reliability analysis of bridge components with force-based elements. The numerical examples indicate the moment-shear interaction is significantly high in most probable failure modes of bridge girders. The limit state definitions in the proposed methodology is recommended to use instead of uncoupled shear and moment capacity that can lead to non-conservative estimates of reliability. The importance measures highlights the axle loads and distribution factors have significant influence on the most probable failure mode.

Another important source of uncertainty in bridge systems is due to modeling approaches of column members subjected to extreme load cases such as seismic. The methodology provides an approach for the reliability analysis of bridge columns using the formulated response sensitivity of force-based elements. One force-based element represents bridge columns under lateral loading to avoid discretization uncertainty of meshing displacement-based elements. However, the choice of an integration method in the state determination of force-based finite elements has a significant influence on the computed element response.

Recent advances in the literature regularize the strain-softening response of force-based frame elements by either modifying the constitutive parameters or scaling selected integration weights. While the former case maintains numerical accuracy for strain-hardening behavior, the regularization requires a tight coupling of the element constitutive properties and the numerical integration method. In the latter case, objectivity is maintained for strain-softening problems; however, there is a lack of convergence for strain-hardening response. To resolve the dichotomy

between strain-hardening and strain-softening solutions, a numerically consistent regularization technique is developed for force-based frame elements using interpolatory quadrature with two integration points of prescribed characteristic lengths at the element ends.

To assess the modeling uncertainty associated with integration methods in force-based elements, analytical sensitivity of one-dimensional interpolatory quadrature is developed via direct differentiation of the locations and weights of integration points. Using the analytical sensitivity formulations, the additional integration parameters in the new regularization technique are considered as epistemic uncertainty in reliability analysis of bridge columns. The numerical examples quantify the epistemic uncertainty of selecting a force-based integration method as well as permitting integration points and weights to be treated as random variables in a probabilistic structural analysis.

©Copyright by Hamutcuoglu Osman Murat
May 3, 2010
All Rights Reserved

Parametric Uncertainties in Reliability Analysis of Bridge Structures

by

Hamutcuoglu Osman Murat

A DISSERTATION

submitted to

Oregon State University

in partial fulfillment of
the requirements for the
degree of

Doctor of Philosophy

Presented May 3, 2010
Commencement June 2010

Doctor of Philosophy dissertation of Hamutcuoglu Osman Murat presented on
May 3, 2010.

APPROVED:

Major Professor, representing Civil Engineering

Head of the School of Civil and Construction Engineering

Dean of the Graduate School

I understand that my dissertation will become part of the permanent collection of Oregon State University libraries. My signature below authorizes release of my dissertation to any reader upon request.

Hamutcuoglu Osman Murat, Author

ACKNOWLEDGEMENTS

This dissertation would not have been possible without help and support of numerous people. First of all, I would like to thank my advisor, Dr. Michael H. Scott, for all his guidance and encouragement throughout my doctoral studies. He taught me many important lessons that shaped and widened my engineering vision during all the years we worked together. Next, I would like to thank the doctoral committee members: Dr. Christopher Higgins, Dr. Timothy Kennedy, Dr. Irem Tumer and Dr. Peter Ruggiero for their precious time and suggestions regarding my dissertation.

This dissertation is a derivative of research sponsored by the Oregon Department of Transportation (ODOT) into efficient methods of load rating bridge girders. I would like to thank ODOT for providing support to my doctoral studies.

Finally, I would like to give my special and deepest appreciations to my family to whom I owe so much. I thank my parents, my sister and my grandmother for all their love, prayers, patience and endless support throughout all the years I stayed thousands of miles away from home. Also my special thanks goes to my uncle, Dr. Haluk Bukan MD, for believing in me and all his support from the beginning of my bachelors studies.

TABLE OF CONTENTS

	<u>Page</u>
1 Background	1
2 Literature Review	4
2.1 Probability-Based Engineering Applications	4
2.2 Reliability Methods	7
2.3 Uncertainty Modeling	14
2.3.1 Aleatory Uncertainty	14
2.3.2 Epistemic Uncertainties	16
2.4 Sensitivity Analysis	19
2.5 Finite Element Reliability	20
2.6 OpenSees Software Framework	21
2.7 Flexural-Shear Interaction Material Models	23
3 Methodology	26
3.1 Limitations and Objectives	26
3.2 Bridge Member Modeling in OpenSees	28
3.3 Reliability Method: FORM	34
3.3.1 Aleatory Uncertainty	38
3.3.2 Epistemic Uncertainty	38
3.3.3 Performance Function	41
3.4 Response Sensitivity: DDM	44
3.4.1 Global Response Sensitivity	45
3.4.2 Force-Based Element Response Sensitivity	47
4 Reinforced Concrete Bridge Girder Sensitivity and Reliability	51
4.1 Section Response Sensitivity	51
4.1.1 Uniaxial Section Model Sensitivity	52
4.1.2 Biaxial Section Model Sensitivity	53
4.2 Biaxial MCFT Material Model	54
4.2.1 Strain Compatibility	57
4.2.2 Constitutive Behaviors	58
4.2.3 Equilibrium Condition	59
4.2.4 Angle Search Algorithm	60

TABLE OF CONTENTS (Continued)

	<u>Page</u>
4.2.5 Tangent Stiffness	63
4.2.6 Sensitivity Formulations	65
4.3 T-Beam Section	68
4.3.1 T-Beam Fiber Discretization	68
4.3.2 T-Beam Section Shape Sensitivity Equations	71
4.4 Software Design for The Methodology Tools	72
4.4.1 Implementation of Fiber Section	74
4.4.2 Analysis Setup	78
4.4.3 Model Builder	81
4.4.4 Reliability Analysis Setup	82
4.5 Material Modeling Verifications	82
4.5.1 Simply-Supported Beams with Flexure and Shear Failure Modes	84
4.5.2 Cantilever Test Specimens with Axial Loading	88
4.5.3 Simply-Supported T-Beam Girder Specimen	90
4.6 Verification of DDM Equations	95
4.6.1 Elastic Section Sensitivity Verifications	97
4.6.2 MCFT Material Sensitivity Verifications	100
4.6.3 T-beam Geometry Sensitivity Verifications	106
4.7 Reliability Analysis Examples	106
4.7.1 Bridge Girder with Uniaxial and Biaxial Material Models	110
4.7.2 Bridge Girder with T-Section Model	120
4.7.3 The Framework for Live Load Reliability Analysis of Bridge Girders	128
5 Reinforced Concrete Bridge Column Sensitivity and Reliability	134
5.1 Interpolatory Quadrature Sensitivity	134
5.2 Regularization Approaches	136
5.2.1 Regularization Based on Scaling Integration Weights	138
5.2.2 Regularization Based on Interpolatory Quadrature	141
5.2.3 Proposed Regularization Method	144
5.2.4 Software Design of Regularized Integration Method	148
5.3 Regularized Integration Verifications	149
5.3.1 Sensitivity of ξ Parameters	152

TABLE OF CONTENTS (Continued)

	<u>Page</u>
5.3.2 Reinforced Concrete Columns With Hardening and Softening Behavior	156
5.4 Reliability Analysis of Bridge Column with Regularized Method . .	160
5.4.1 Verification of DDM Equations	162
5.4.2 Column Reliability Example	163
 6 Conclusions	 169
 Appendices	 175
A AASHTO-MCFT Capacity Function	176
B Multi-Beta (MB) Capacity Function	183
C OpenSees Uniaxial Material: Concrete02	188
D OpenSees Uniaxial Material: Steel02	189
E McKenzie River Bridge Girder Section Properties	190
 Bibliography	 190

LIST OF FIGURES

<u>Figure</u>	<u>Page</u>
2.1 Limit state definition with probability density function.	8
2.2 Hasofer and Lind (1974) reliability index	12
3.1 Modeling hierarchy for structural analysis in OpenSees [130]	29
3.2 Simply-supported basic system for beam finite elements	31
3.3 Bending moment and shear force developed in the basic system due to a moving transverse point load.	32
3.4 MB performance functions	41
3.5 LC performance function	44
3.6 Derivative of bending moment and shear force in the basic system with respect to point load.	49
4.1 Section mechanics and strain fields	55
4.2 Principal strain-stress model	58
4.3 Angle search procedure	61
4.4 T-beam fiber section	69
4.5 Design strategy for MCFT fiber section class.	75
4.6 Design strategy for section integration class.	76
4.7 Tcl procedure for moving load reliability analysis.	77
4.8 Parameter entries in reliability analysis scripts	79
4.9 Custom setup parameters	79
4.10 Tcl capacity procedures	80
4.11 Tcl codes for model builder and moving load simulation	83
4.12 Tcl code to assign random variables and performance functions . . .	84
4.13 Simply-supported beams: Material and geometry configurations. . .	85
4.14 Load-displacement behavior of Beam No.1 with flexural failure mode	86

LIST OF FIGURES (Continued)

<u>Figure</u>	<u>Page</u>
4.15 Load-displacement behavior of Beam No.2 with shear failure mode .	87
4.16 Double-cantilever test setup and reinforcement details	89
4.17 Load-displacement behavior of test specimens	91
4.18 T-beam specimen setup and crack propagation map	92
4.19 T-beam specimen section details	92
4.20 Load-displacement behavior of T-beam girder	93
4.21 Fiber principal axes compression directions	94
4.22 Span lengths and critical locations for an interior girder of the McKenzie River Bridge.	96
4.23 Axle weights and spacings of vehicles used in sensitivity and reliability analyses: (a) HS-20 truck; (b) OR-STP-4D single trip permit truck.	98
4.24 Typical reinforcing layout and details for an interior girder of the McKenzie River Bridge.	99
4.25 Verification of DDM moment response sensitivity computations for moving load analysis of an interior girder of the McKenzie River Bridge with elastic materials and rectangular sections.	101
4.26 Verification of DDM shear response sensitivity computations for moving load analysis of an interior girder of the McKenzie River Bridge for elastic material and rectangular section parameters. . . .	102
4.27 Verification of DDM moment response sensitivity computations for moving load analysis of an interior girder of the McKenzie River Bridge for vehicle load parameters.	103
4.28 Verification of DDM shear response sensitivity computations for moving load analysis of an interior girder of the McKenzie River Bridge for vehicle load parameters.	104

LIST OF FIGURES (Continued)

<u>Figure</u>		<u>Page</u>
4.29	Verification of DDM moment-shear response sensitivity computations for moving load analysis of an interior girder of the McKenzie River Bridge for biaxial material parameters.	105
4.30	Verification of DDM moment response sensitivity computations for moving load analysis of an interior girder of the McKenzie River Bridge for T-beam section parameters.	107
4.31	Verification of DDM shear response sensitivity computations for moving load analysis of an interior girder of the McKenzie River Bridge for T-beam sections parameters.	108
4.32	MB and LC capacities at mean values of resistance variables	110
4.33	Reliability analysis for moment-shear interaction at rectangular section 17: (a) M-V capacity by LC, (b) M-V capacity by MB, (c) All curves	115
4.34	Reliability analysis for moment-shear interaction at rectangular section 14: (a) M-V capacity by LC, (b) M-V capacity by MB, (c) All curves	116
4.35	Reliability analysis for moment-shear interaction at T-beam section 17: (a) M-V capacity by LC, (b) M-V capacity by MB	124
4.36	Reliability analysis for moment-shear interaction at T-beam section 14: (a) M-V capacity by LC, (b) M-V capacity by MB	125
4.37	Reliability analysis at all sections on an interior girder of the McKenzie River Bridge: Reliability index for load increments 0-100. . . .	131
4.38	Reliability analysis at all sections on an interior girder of the McKenzie River Bridge: (a) Critical reliability index for load increments 0-100; (b) Importance measures of the random variables at the critical load location with RV numbers on the x-axis.	132
5.1	Force-based element regularization methods based on scaling integration weights in the plastic hinge regions: (a) Gauss-Lobatto over the plastic hinge and interior regions; and (b) Gauss-Radau in the plastic hinge regions and Gauss-Legendre over the interior.	140

LIST OF FIGURES (Continued)

<u>Figure</u>		<u>Page</u>
5.2	Simply-supported beam in a state of anti-symmetric bending and with a bilinear moment-curvature relationship.	140
5.3	Computed moment-rotation relationship of regularization methods based on scaling integration weights compared with standard five-point Gauss-Lobatto rule for (a) strain-hardening and (b) strain-softening section behavior.	142
5.4	(a) Standard five-point Gauss-Lobatto integration rule; (b) Five-point Gauss-Lobatto rule regularized by addition of two integration points just inside the element ends.	145
5.5	UML diagram for implementation of proposed regularization method in an object-oriented finite element framework.	150
5.6	Comparison of beam response between standard and regularized five-point Gauss-Lobatto for strain-hardening section behavior. . . .	151
5.7	Comparison of beam response between standard and regularized five-point Gauss-Lobatto for strain-softening section behavior. . . .	153
5.8	Sensitivity of beam response for increasing values of parameters ξ_I and ξ_J for regularized five-point Gauss-Lobatto integration and strain-hardening section behavior.	154
5.9	Sensitivity of beam response for various combinations of parameters ξ_I and ξ_J and load steps for regularized five-point Gauss-Lobatto integration and strain-softening section behavior.	155
5.10	Dimensions of specimen 430 in the test of Lehman and Moehle [78].	159
5.11	Computed global response and local moment-curvature relation at the support section of specimen 430.	159
5.12	Dimensions of specimen BG-8 in the tests of Saatcioglu and Grira [128]	161
5.13	Computed global response and local moment-curvature relation at the support section of specimen BG-8.	161
5.14	One degree indeterminate beam and the integration parameters . . .	162

LIST OF FIGURES (Continued)

<u>Figure</u>	<u>Page</u>
5.15 Sensitivity of end rotation to regularized integration parameters. . .	164
5.16 Sensitivity of reaction moment to regularized integration parameters.	165
5.17 Comparison of end rotation sensitivity to plastic hinge length for strain-hardening and strain-softening behavior.	166

LIST OF TABLES

<u>Table</u>	<u>Page</u>
3.1 Parameter variations in documented measurements	39
4.1 Shape Sensitivity Parameters for T-Beam Section	73
4.2 Material and Geometry Properties of Test Specimens	89
4.3 Material models used in live load reliability of girders.	111
4.4 Random variable descriptions for the finite element reliability analysis of an interior girder of the McKenzie River Bridge using uniaxial materials and rectangular sections	112
4.5 Random variable descriptions for the finite element reliability analysis of an interior girder of the McKenzie River Bridge using biaxial concrete material and rectangular sections	113
4.6 Importance measures (γ -values) of the random variables for uniaxial elastic material at the critical load increment.	118
4.7 Importance measures (γ -values) of the random variables for nonlinear nDMaterial at the critical load increment.	119
4.8 Random variable descriptions for the finite element reliability analysis of an interior girder of the McKenzie River Bridge using uniaxial material and T-sections.	121
4.9 Random variable descriptions for the finite element reliability analysis of an interior girder of the McKenzie River Bridge biaxial material and T-sections.	122
4.10 Importance measures of the random variables for Uniaxial elastic material at the critical load increment	126
4.11 Importance measures of the random variables for Nonlinear nDMaterial at the critical load increment	127
4.12 Random variable descriptions in the multiple section FERA.	129
4.13 Ranking of random variables with importance measure exceeding 0.1 in the McKenzie Bridge girder example.	133

LIST OF TABLES (Continued)

<u>Table</u>		<u>Page</u>
5.1	Random variable distributions assigned to the uncertain parameters in reliability analysis and their values and importance measures at most probable failure point (MPP).	167

LIST OF APPENDIX FIGURES

<u>Figure</u>	<u>Page</u>
A.1 AASHTO ultimate shear-moment calculation procedure	177
A.2 $\beta^* - \theta^*$ values for longitudinal strain ε_x	178
A.3 The level of required Stirrups for each $\beta^* - \theta^*$ cell	178
A.4 The interpolation of $\beta^* - \theta^*$ values	179
A.5 Computation of M-V points of interaction diagram	181
A.6 Shear cap computation: Interpolation of M-V points	182
B.1 The body of function <i>getMV</i>	183
B.2 Calculation of the effective depth for positive and negative moment	185
B.3 The Tcl code combining M^+V and M^-V capacity	186
B.4 The Tcl code computing parameters of limit state line equations . .	187
C.1 Constitutive model of uniaxial Concrete02 material	188
D.1 Constitutive model of uniaxial Steel02 material	189
E.1 Tcl arrays containing section properties	190

DEDICATION

To my family.

Chapter 1 – Background

Uncertainties are inevitable in any estimate of structural engineering problems. Properties of the structural system such as fabrication and material parameters, external stimuli such as loads, imperfect modeling, lack of experience and human factors are uncertain and cannot be determined exactly. In the presence of uncertainties, neither loadings acting on systems nor component resistance can be treated as deterministic when simulating structural response. The probability of failure is always greater than zero and absolute safety for structures is impossible to achieve. However, the possible range of demand and resistance can be predicted and idealized. Consequently, a probabilistic design philosophy can ensure a level of safety for engineered structures by predicting the probability of failure.

The study of reliability is concerned with prediction of the probability of failure in any stage of a structure's lifetime. In the last quarter century, conventional structural design procedures have been replaced with risk- and reliability-based approaches that have found acceptance throughout the world. By combining statistical knowledge with engineering procedures, reliability analysis has become a popular area of interest in structural engineering. Ensuing research studies have given birth to new design codes and have started to replace deterministic design concepts with novel reliability-based design. Probabilistic structural analysis treats system properties and external stimuli as uncertain random variables [32]. Early research led to the adoption of load combination factors in the current generation of structural design codes. American Institute of Steel Construction Load and Re-

sistance Factor Design (LRFD) [7], Eurocode 3 [20] and Ontario Highway Bridge Design Code (OHBDC) [110] are design codes in different stages of reliability-based development.

Uncertain strength and load parameters may show statistically regular behavior; so that probability theory should be considered for specifying limits of acceptable structural performance. Reliability analysis must account for a number of uncertainties to predict probability of failure under prescribed limit states. Hacking [50] classified the source of uncertainties in probability approaches as either aleatory or epistemic.

Aleatory uncertainty is due to the natural randomness and inherent variability of complex phenomena. As a result, these are uncertainties that can not be reduced. Repeated measurements of a physical quantity may not yield the same value due to fluctuations in the environment, test procedures and instruments. Structural parameters such as material properties, geometry and loads are treated as aleatory uncertainties.

Conversely, epistemic uncertainty is due to limitations in knowledge or data and can be reduced with improved mathematical modeling or increased data collection. Structural analysis models are idealized representations of systems using mathematical solutions and numerical approximations. The model uncertainty within the mathematical formulation of the relevant limit state is considered as epistemic uncertainty.

The finite element method (FEM) has become a widely used tool to simulate structural response with non-linear behavior. In the presence of uncertainties, structural response can be predicted by a methodology that combines probabilistic approaches and finite element modeling. Finite element reliability analysis (FERA)

provides such opportunity by tracking variation of structural response when every quantity during the deterministic analysis is uncertain. [51].

The objective of this study is to develop efficient probabilistic analysis approaches for bridge components using existing concepts of probability, structural reliability and finite element analysis. The sensitivity to uncertain parameters is computed in order to investigate their influence on possible failure modes. Live load reliability of bridge components such as girders will be investigated using the proposed methodology. In addition, the modeling uncertainty associated with numerical evaluations of finite element formulations will be investigated on bridge columns subjected to excessive load cases such as seismic loading.

Chapter 2 – Literature Review

The current literature on probabilistic approaches and bridge engineering procedures is reviewed to build up efficient finite element reliability analysis methods for bridge members.

2.1 Probability-Based Engineering Applications

Allowable Stress Design (ASD) is the conventional design procedure in structural engineering. The uncertainty in demand and resistance is represented by a single safety factor and the material behavior is limited to the elastic region. On the other hand, Load and Resistance Factor Design (LRFD) incorporates a methodology with multiple load and resistance factors based on known variability of applied loads and material properties. These factors are calibrated using probabilistic approaches and statistical data to ensure a uniform level of safety.

The first examples concerning probabilistic approaches in design codes were the code calibrations and the selections of load and resistance factors for the new edition of the Ontario Highway Bridge Design Code (OHBDC) [108]. Ellingwood et al. [36] presented code calibrations using reliability-based partial factors on load and resistance instead of conventional safety factors. Tabsh and Nowak [139] investigated the reliability of girder bridge systems considering the two extreme cases of full correlation and no correlation between girder strengths. Their results indicated that reliability of bridges designed according to American Association of State Highway and Transportation Officials (AASHTO) specifications vary depending

on span and type of material. Mori and Ellingwood [101] presented a probability-based method to evaluate time-dependent reliability of components and systems and the sensitivity of the reliability index to various parameters describing load occurrence and strength degradation. Moses [102] presented fundamental aspects of design specifications based on reliability modeling that concerns highway bridge applications.

The basic philosophy in searching the optimum safety of structures was accepted in structural engineering area. However, until the last decade there has been no standard adopted to comprise all of the available information for the purposes of developing reliability-based criteria for design. AASHTO presented load and resistance factors in design specifications for highway bridges that introduced a limit state design philosophy in order to achieve a uniform level of reliability throughout the system [1].

Optimum safety is the ultimate goal not only in the design of new bridge structures but also in assessments of existing bridges designed under previous design standards. A considerable number of existing bridges in the United States has required repair or replacement [109]. Thus, accurate assessment techniques are also needed to evaluate the current load-carrying capacity of existing bridges. In particular, National Cooperative Highway Research Program (NCHRP) project 12-46 was initiated in 1997 to develop a new AASHTO load and resistance factor rating (LRFR) manual that introduces reliability-based evaluation methods [79] for highways. The objective of this evaluation is not to build a new bridge but to use an existing bridge safely and economically. Minervino et al. [96] introduced the AASHTO New Guide Manual for Condition Evaluation and LRFR of Highway Bridges. This manual extends the provisions of the LRFD specifications to

the areas of the inspections, load rating, permit rules, fatigue evaluation and load testing of existing bridges.

In reliability-based study of bridge structures, the aim has been to assemble a statistical database and to evaluate the probable bridge loads and the strength of system components. Attempts to develop assessments out of traditional deterministic safety evaluations such as load-ratings were necessary because the current approaches were insufficient to account for uncertainties. Stewart et al. [135] presented a practical application of reliability-based safety assessment which relates the effects of bridge age, current and future traffic volume and loads, and deterioration on the reliability and safety of aging reinforced concrete bridges. Higgins et al. [60] have used risk-based approaches to rank bridges for repair or retrofit decision making, where girder capacities were defined by a multi-linear limit state function based on Modified Compression Field Theory (MCFT) [152].

For reliability of bridges under seismic loading, the Transportation Research Board published a report concerning design of highway bridges for extreme events [44]. The recommended load combinations for extreme cases such as earthquake, vessel collision effect and hydraulic extremities have been implemented in the new edition of the AASHTO LRFD bridge design specifications [3]. For the extreme event case, live load factors were calibrated in the presence of seismic loads. Frangopol et al. [40] proposed reliability estimation of short and slender columns under random loads formulated by Monte Carlo simulation in the load space. Lupoi et al. [85] developed a seismic fragility method based on simulation involving non-linear dynamic analyses and general system reliability with correlated demands and capacities. Nielson and DesRoches [105] provided an analytical methodology for developing seismic fragility curves for highway bridges. The methodology

considered the uncertain response of all major bridge components in assessing seismic vulnerabilities. Kim et al. [75] provided a seismic performance assessment of reinforced concrete bridge columns under variable axial load.

2.2 Reliability Methods

In all probabilistic efforts, the essential output is the probability of failure of a structure relative to a limit-state criterion that divides the structural performance space into safe and failure states. Thoft-Christensen and Baker [144] defined structural reliability as the probability that a structure will not attain each specified limit state during a reference period. The limit state is the boundary between safety and failure. Statistical models have been established on the basis of experiments, measurements, analyses and judgment while structural safety is quantified by mathematical formulations such as limit states.

For a structural component, the load carrying capacity, R , and the load effect, S , formulate the basic limit state function, g (performance function):

$$g(R, S) = R - S \quad (2.1)$$

where $g > 0$ denotes that the structure is safe and the boundary limit state occurs for $g = 0$. The probability of failure, PF , can be expressed in terms of the performance function:

$$PF = P(R - S < 0) \quad (2.2)$$

Both R and S contain a set random variables and the occurrence of these variables is defined using the basic statistical distribution functions such as probability

density function (PDF). The limit state function $g(\mathbf{X}) < 0$ is checked regarding to the model distribution of random variables, \mathbf{X} . The probability of failure, PF , is formulated as the multi-fold integral:

$$PF = \int \dots \int_{g < 0} f_x(\mathbf{X}) d\mathbf{X} \quad (2.3)$$

where $f_x(\mathbf{X})$ is the joint probability density function for the basic random variables and the integration is evaluated over the failure region as shown in Fig. 2.1. However, the integral is cumbersome to evaluate and various methods have been developed to compute the probability of failure. The diversity of statistical distributions to model randomness and the number of random variables can make Eq. (2.3) complex to evaluate using integration methods. On the other hand, simulation techniques and second-moment methods are favorable to use in structural reliability problems.

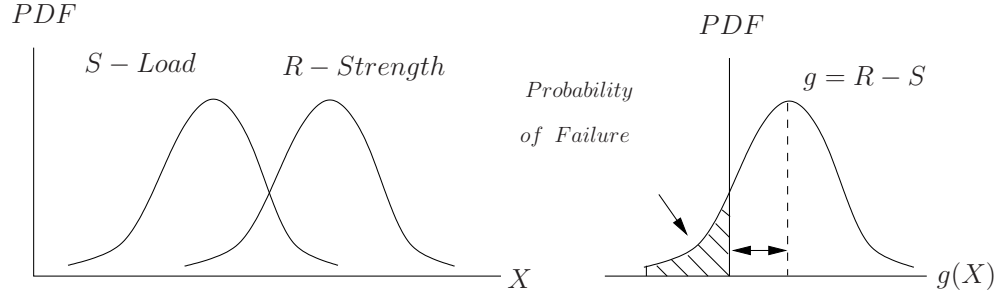


Figure 2.1: Limit state definition with probability density function.

Early applications of structural reliability use sampling and trial methods such as Monte Carlo Simulation (MCS) that consists of the direct realization of events. For N number of trials, the approximate probability of failure is calculated:

$$PF \approx \frac{n(g < 0)}{N} \quad (2.4)$$

where the ratio of the number of failure trials, n , to the total trials, N , gives the probability of failure.

The key feature in MCS is the generation of random variables with specified probability distributions. The common method for generating random variables is to create numerical values in the interval $[0, 1]$ and use the inverse cumulative distribution function (CDF) of the variable while assuming a uniformly distributed number. The random number generator produces discrete numbers in the interval based on arbitrarily selected seed values. However, the generator algorithms based on a recursive mathematical formula are completely deterministic. In addition, a drawback for this method can be the high number of simulations which must be carried out to obtain meaningful results. For the case that the probability of failure is relatively small, MCS loses accuracy using the same number of runs.

Several researchers have used reliability methods based on MCS as an assessment tool for highway bridges [8, 37, 109, 135]. In addition, several techniques have been developed to improve the efficiency of MCS such as importance sampling, Latin Hypercube sampling and directional simulation. McKay et. al [92] presented the Latin Hypercube sampling method which generates multivariate samples of statistical distributions. The directional simulation method defines a set of directions forming a unit hyper-sphere to evaluate the probability integral and reduces the dimension of the limit state [17, 73, 94, 100, 104].

Second-moment methods consider the special case of reliability estimation in which variables are represented by their first two moments: mean value and standard deviation. Higher order moments such as skewness and flatness are ignored. The simple reliability analysis based on second-moment representations leads to effective calculation methods applicable in reliability analyses that use

fully-probabilistic information [32]. The method has been attractive with its mathematical formulations defining uncertain parameters as continuous random variables in structural engineering.

For the case that quantities are normally distributed and statistically independent, the limit state function, g , is also normally distributed as shown in Fig. 2.1. The characteristic properties, mean value μ and standard deviation σ of the limit state distribution can be obtained in terms of load S and resistance R parameters.

$$\mu_g = \mu_R - \mu_S \quad (2.5)$$

$$\sigma_g^2 = \sigma_R^2 - \sigma_S^2 \quad (2.6)$$

The probability of failure is expressed in the form

$$\Phi \left[\frac{-\mu_g}{\sigma_g} \right] = \Phi(-\beta) \quad (2.7)$$

where Φ is the inverse normal cumulative density function. The reliability index, β , is simply the number of standard deviations from the mean of the safety margin to the failure state [26]. Indices below the target level are not acceptable while the higher ones are not practically feasible. The selection of target reliability index is a multi-disciplinary task that comprises structural, statistical and economical analyses.

In structural reliability problems, variations in parameters can be in non-normal distributions. Moreover, the limit state function is generally non-linear and contains more than two basic random variables. To overcome these problems, techniques incorporating transformation, linearization and iterative approaches have

been developed. For non-linear limit state functions, a linear approximation can be obtained applying Taylor expansion around a linearization point. Since first-order derivatives are used in Taylor series expansion, the method is known as the first-order reliability method (FORM). For the case that the mean values of the random variables is selected as linearization point, the method takes the name First-Order Second-Moment (FOSM) reliability and the limit state has the form:

$$g(x_1, \dots, x_n) \approx g(\mu_{x_1}, \dots, \mu_{x_n}) + \sum_{i=1}^n (x_i - \mu_{x_i}) \left. \frac{\partial g}{\partial x_i} \right|_{\mu_{\mathbf{x}}} \quad (2.8)$$

The reliability index expressed in terms of mean values has the form:

$$\beta = \frac{g(\mu_{x_1}, \dots, \mu_{x_n})}{\sqrt{\sum_{i=1}^n \left[\left. \frac{\partial g}{\partial x_i} \right|_{\mu_{\mathbf{x}}} \sigma_{x_i} \right]^2}} \quad (2.9)$$

However, FOSM method has an invariance problem that the reliability index values depend on the specific form of the limit state function. Hasofer and Lind [54] presented a reliability method (HL) that did not suffer from ambiguity problems. The approach was based on the linearization of the limit state function at a design point on failure surface. The limit state surface was approximated with a tangent hyperplane using first-order gradients in Taylor expansion. The distance between the limit state function linearized at design point and the origin of reduced variables is analytically calculated. The design point is the solution to a constrained optimization problem where gradient-based iterative search algorithms are suggested to find the design point. HL method proposed a mapping of random

variables, \mathbf{X} , into a standard space of uncorrelated reduced variables, \mathbf{Y} .

$$g(\mathbf{Y}) = g(\sigma_{x_1}y_1 + \mu_{x_1}, \dots, \sigma_{x_n}y_n + \mu_{x_n}) = 0 \quad (2.10)$$

The most probable failure point is the one that minimizes the distance from the origin of standard space of random variables to the limit state surface. Having the same formulation as given in Eq. (2.9), the reliability index is described as the minimum distance from the origin of the random variables to the design point as shown in Fig. 2.2. However, this point is not a priori; so that an iterative method needs to be used to locate the design point and to solve for the reliability index.

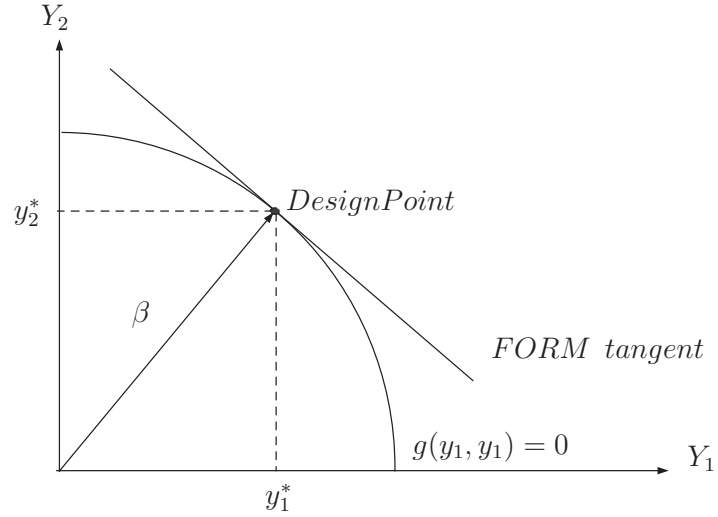


Figure 2.2: Hasofer and Lind (1974) reliability index

The distance between the limit state function linearized at design point and the origin of reduced variables is analytically calculated. The design point is the

solution to the constrained optimization problem [58]:

$$\mathbf{Y}^* = \operatorname{argmin}\{\|\mathbf{Y}\| \mid g(\mathbf{Y}) = 0\} \quad (2.11)$$

where \mathbf{Y}^* is the design point and *argmin* denotes the argument of a minimum of a function.

In the HL method, random variables are assumed to be normally distributed. Rackwitz and Fiessler [124] modified HL method by incorporating the transformation of non-Gaussian random variables into normally distributed equivalent variables (HLRF Method). The HLRF algorithm is similar to the HL iteration method except the transformation steps need to be implemented to calculate the mean and standard deviation of the equivalent normal variables using transformation techniques. Liu and Der Kiureghian [81] proposed a multi-variable Nataf distribution model consistent with prescribed covariance and capable of describing a wide range of correlation coefficients. Rosenblatt [127], Gurley et al. [49] and Isukapalli [66] provided other techniques to transform non-Gaussian variables into standard normal random variables.

FORM has been the most popular second-moment reliability method in structural engineering; however, the accuracy of FORM has been examined for limit states with high-nonlinearity, [29]. The second-order reliability method, SORM, improves the approximation of failure space using a quadratic limit state surface at the design point. Recent studies have helped in the development of higher order moment assessments for structural reliability [156, 158, 56, 157]. When compared to the high computational effort of MCS, second-moment method which directly propagates parameter uncertainty into the result is an alternative and computationally efficient approach. On the other hand, this method requires ex-

plicit formulations of probability problem in order to obtain first- and second-order gradients of the limit state formulated in terms of structural response. Thus, a response sensitivity analysis is required to compute the gradients in second-moment methods.

2.3 Uncertainty Modeling

Reliability analysis requires information about uncertain parameters in the structural system. Defining sources of uncertainties and variety of quantities is important. Many researchers have studied both aleatory and epistemic uncertainties in reliability problems.

2.3.1 Aleatory Uncertainty

Statistical models have been established on the basis of measurements, surveys, tests, analysis and judgment. Mirza [98] measured the variations in depth and width of beam elements due to construction. The variation of mechanical and material properties of reinforcement and concrete such as area of reinforcing steel and concrete compressive strength has been detected [99, 97]. Using available test data, Ellingwood et al. [36] provided statistical parameters such as bias factors, coefficient of variation for steel, concrete modulus of elasticity and dimensions. Euro-International Committee for Concrete (CEB) [33] provided empirical equations to compute mean value and coefficient of variation of concrete material properties. Haukaas and Der Kiureghian [57] treated nodal coordinates as aleatory uncertainty due to fabrication and modeled these parameters as random variables.

Quantifying live loads used in design procedure is difficult because load model

to represent critical demand is a combination of relative positions of vehicles on the bridge. Usually as a result of field observations or weight-in-motion (WIM) studies, a large number of bridge live load models have been proposed. ASTM (2002) described WIM, the process of measuring the dynamic forces of a moving vehicle and estimating the loads of the static vehicle. WIM measuring systems are classified according to the performance levels and device setups. Since required performance is indicated in terms of tolerance of measurements, WIM systems create uncertainty on load measurements. Consequently, required performance level can be considered as coefficient of variation. For example, the standard indicates that Type I,II and III WIM data collecting systems provide single axle weight measurement with the performance of $\pm 20\%$, $\pm 30\%$ and $\pm 15\%$, respectively, in a tolerance of 95% conformity. Variance of the applied traffic load must be based on a statistical model obtained from a WIM study.

Nowak and Lind [108] proposed statistical parameters of live loads using heavy commercial survey results while developing a reliability-based code calibration for Ontario highways. Ghosn and Moses [43] proposed a random truck loading based on generalizations of renewal processes where axle weights, axle spacings, speed and can be accounted for as random variable.

Nowak [106] proposed a live load model from truck surveys and weigh-in-motion measurements. The model contained the mean value and coefficient of variation of bending moments and shear forces for each truck in terms of HS20 truck for various span lengths. Extrapolating the short-term observations, 75 year loads were determined in the model. However, since HS20 truck provides a conservative and deterministic representation of typical truck on the highway, it does not account for the cumulative effect of a large number of trucks passing over a bridge over a

period of time [38]. Nowak [107] calibrated the nominal HL93 design truck loading model to match a projected expected 75-year maximum live load effect for all span ranges. All these previous studies have been essential for development of live load models and a rational bridge evaluation code.

2.3.2 Epistemic Uncertainties

The structural analysis is based on idealization of reality in a form of mathematical problem and the finite element model analysis is an approximate numerical analysis technique employed to solve the problem. Since idealizations and approximations are used to model the reality, uncertainties in the representation is inevitable.

Koduru and Haukaas [77] considered the finite element discretization of meshing displacement-based formulations to be epistemic uncertainty in reliability analysis. For the case that force-based elements are used, numerical integration of element compatibility equations converges to a unique solution as high-order integration methods such as Gauss-quadratures are employed or the number of integration points is increased. The analysis results can be sensitive to weight and location of element integration points. Therefore, the accuracy of numerical integration methods can be treated as analysis uncertainty in finite element reliability. In FORM analysis, locations and weight of the integration points can be modeled as random variables.

Simulating localized response of structural systems using strain-softening constitutive model causes several computational challenges since the equilibrium solution becomes ill-posed and the results are mesh-dependent. This is important for evaluating the resistance of the bridge components that show highly inelastic

behavior due to extreme loadings such as earthquakes. In particular, methods suitable for spread plasticity of hardening are not sufficient to ensure localized deformations observed in experiments can be simulated objectively. The difference between two behaviors makes the selection of integration rule dependent to the type of behavior. The analyst must know a priori on which method to use when the answer may not be obvious based on the material properties and loading. Consequently, a regularization for force-based frame elements is needed to evaluate the compatibility equations regardless of the section constitutive behavior. Several studies have provided integration rules and regularization methods to accurately integrate spread plasticity under hardening or localized deformations under softening; but not a method that can represent both cases.

Bazant and Oh [14] proposed the crack band theory for strain-softening behavior of heterogeneous aggregate material where properties were defined by fracture energy, uniaxial strength limit and width of the crack band. The method was implemented in solid finite element codes and has received successfully matching analysis results for various experimental data. In addition, Bazant et al. [15] presented an efficient discretization procedure by layered finite element approach and a direct iteration method for step-by-step loading. This approach provided well-behaved convergent solution for beam and frame element with strain-softening. However, numerical solutions were highly sensitive to the finite element mesh size so that, the problem leads the analysis to non-objective global response output. In order to overcome the drawback of strain-softening in finite element analysis, De Borst and Muhlhaus [27] proposed a plasticity theory based on higher-order spatial gradients of plastic strains. Wells et al. [155] presented a regularized continuum method comprising discontinuous displacement functions implemented in standard

finite element procedure. This method represented highly localized deformations due to strain-softening behavior, independent of the finite element mesh structure. Using the concept of strong discontinuities in displacement field for beam elements, Armero and Ehrlich [12] presented a localized model incorporating hinge theory. Several approaches to simulating the localized response of frame members have been proposed in literature [22, 35, 45, 65, 68, 88, 118, 122].

For force-based beam-column elements, Coleman and Spacone [23] provided a regularization method to predict objective local and global responses applying the constant fracture energy criterion for compression behavior of concrete. However, this approach required modification in material properties and tied significantly modified parameters to the integration rule. Addessi and Ciampi [6] proposed a regularized Gauss-Lobatto (GL) quadrature for force-based finite elements in order to simulate localized plasticity by mapping locations of two- and three-point GL rules over prescribed plastic hinge lengths at the element ends. Scott and Fenves [129] apply two-point Gauss-Radau quadrature [5] over the plastic hinge regions and scale the integration weights by four in order to regularize the element response. While this approach ensures regularized response for strain-softening behavior without modifying the element constitutive properties, the response is too flexible when these integration methods are used to simulate strain-hardening response. As a result, an analyst must know a priori whether to use a standard or a regularized integration approach when the answer may not be obvious from the given material properties and loading conditions.

2.4 Sensitivity Analysis

The computation of response sensitivities is an essential component to various engineering problems such as optimization, system identification, reliability applications, system health monitoring, and finite element model updating procedures [67, 147, 160]. Tabsh and Nowak [139] developed sensitivity functions relating the reliability with nominal values of load components and resistance parameters. To obtain accurate reliability assessments, response sensitivity is required to rank the parameters according to their importance on structural performance [59]. Furthermore, as a stand-alone product, response sensitivity can be useful in structural design by indicating the sensitivity of structural response to changes in the design parameters. Patrick et al. [114] performed a set of sensitivity analyses to measure uncertainty in load properties and to determine the influence of live load parameters on force distributions. Padgett and Des Roches [113] assessed the sensitivity of seismic demand to varying parameters in a range of structural systems.

There are several techniques to compute response sensitivity. Finite difference methods (FDMs) consist of repeated system analyses with perturbed parameters. The FDM procedure can easily be performed in any finite element analysis program. Since it requires full re-analysis for each parameter, the FDM procedure can be computationally inefficient and the accuracy depends on size of perturbations. The direct differentiation method (DDM) is based on the differentiation of structural equilibrium, compatibility and constitution equations with respect to the uncertain parameters [76]. For the case that response sensitivity equations are implemented alongside the ordinary finite element response equations, DDM provides accuracy, efficiency and consistency by computing the response and the response sensitivity at the same precision rate without repeated analyses. Due to

its efficiency, the DDM has been the ideal tool to compute required gradients in several finite element reliability efforts [59, 30, 57].

2.5 Finite Element Reliability

FERA merges finite element methods with reliability analysis. However, the major shortcoming is that the computational time can be extremely high since the structural analysis needs to be repeated many times to obtain the gradient of the limit state equation to random variables while computing gradients with FDM. Thus, the formulation of gradients of performance function provides the foundation of FERA.

For deterministic evaluation, various finite element software is available in the structural engineering community, including ABAQUS [4], ANSYS [10], DIANA [145], FEAP [140], LS-DYNA [83], OpenSees [93], SAP [24] and STAAD [126]. On the other hand, a limited number of software having reliability analysis module has been developed. Regarding the adopted reliability analysis method, several researchers performed FERA in software frameworks using the second-moment approach because simulation methods require more evaluations of limit state function and more executions of finite element analysis when compared the gradient-based methods.

Der Kiureghian and Ke [31] were among the first to combine FEM and probabilistic structural parameters. A finite element procedure for first-order reliability analysis structures having uncertain properties and subjected to random static loads was presented in this study. Furthermore, Liu and Der Kiureghian [82] proposed a general framework for finite element reliability analysis for geometrically

nonlinear uncertain structures in which the limit surface was approximated using FORM and SORM. Teigen et al. [143] presented the theory and application of probabilistic FEM for nonlinear structures under random loads. Val et al. [148] adopted a finite element model in which material properties are random variables and a basic form of model uncertainty was implemented. Borri and Speranzini [19] provided a numerical procedure that could be implemented in any finite element code having an internal optimization rule. Since the design point in structural problems was determined by calculating the minimum distance from the origin to the failure surface in a set of normalized problems by using a minimization routine of the code in use. In the numerical examples, the minimization function of ANSYS was used to minimize reliability index. Other FE programs such as Cosmos [138] and Nastran [133] have also optimization modules.

2.6 OpenSees Software Framework

The work of Haukaas and Der Kiureghian [58] was important in the context of FERA. The authors provided a detailed reliability analysis manual for OpenSees in a report for performance-based earthquake engineering. The C++ language [28, 137] was employed in the development of OpenSees framework that contained a wide range of structural simulation components including material and geometric nonlinear beam-column elements and solid elements.

First- and second-order finite element reliability analysis methods have been implemented in OpenSees where several algorithms are available such as improved HLRF [56] and Polak-He [119] iterative methods that utilize the gradient of the limit state function. For bridge structures, the OpenSees framework is suitable to

the repetitive nature of moving load analysis since users build and analyze models via commands added to the fully programmable Tcl scripting language [112, 154].

Several researchers made contributions OpenSees providing sensitivity and reliability modules. Scott et al. [131] implemented the DDM sensitivity formulations for force- and displacement-based elements in OpenSees to compute the response gradients with respect to constitutive and geometry parameters. The response gradients provide information needed in structural engineering applications such as optimization, finite element model updating and reliability. Haukaas and Der Kiureghian [55] obtained the response sensitivities with respect to nodal coordinates and global shape parameters in the presence of material and geometric nonlinearity. Employing the sensitivity results, example applications were presented to enable the investigation of the relative importance of uncertainty in the parameters of a finite element model. Haukaas and Scott [59] provided response sensitivity gradients with respect to the dimensions and reinforcing details of fiber-discretized cross-sections of frame members. The implemented gradient formulations yielded parameters such as depth and width of beams, location and area of reinforcement to be characterized by random variables in reliability analysis of reinforced concrete beam-column structures. Koduru and Haukaas [77] investigated the quantification, representation and propagation of epistemic uncertainty by the Bayesian probabilistic approach and explored the fuzzy randomness approach. The proposed novelty was the implementations in rapidly advancing OpenSees software that could produce an uncertain reliability index from which point estimates or confidence bounds are extracted.

OpenSees provides the analyst several formulation options, force-, displacement-based and mixed elements to model beam-column members in FERA. In general

finite element setting of bridge girders, the common approach is to subdivide each span into multiple finite elements with node placed at critical locations. Moving loads are considered as statically equivalent nodal forces. On the other hand, an alternative approach can be that the span was considered as one force-based element whose integration points coincide with critical locations. Using integration approaches, it is straightforward to link bending moment and shear forces to a constitutive model rather than relying on rigid body equilibrium [71].

A displacement-based beam-column element model that includes flexure and shear interaction was incorporated in OpenSees [90]. The original element based on linear interpolation of the curvature and constant axial strain was modified with a third strain component included to account for shear flexibility. However, a similar flexure-shear interaction model is not available for force-based elements. To overcome this problem, the framework can combine several uniaxial materials to increase the number of stress resultants including shear in the element [91]. Regardless of axial behavior of the element, a linear elastic shear constitution model can be applied to the element to monitor shear stress-strain in the section. However, a coupled shear and flexural strain in constitution has not been implemented to establish a non-linear constitutive model for concrete.

2.7 Flexural-Shear Interaction Material Models

Simulating the response of reinforced concrete members subjected to significant shear is not a straightforward task in finite element analysis. The formation and propagation of cracks, stress variations along the vertical and horizontal reinforcing steel, and transmission of forces along the contact locations complicate modeling

and prediction. For shear critical members, uniaxial materials with uncoupled shear- flexural models at the constitution level are not capable of providing a shear dominant behavior accurately and anticipated strength level stays non-conservative in finite element simulations [39].

Timoshenko formulations providing the shear-flexural interaction requires correction factors regarding the shape of sections. However, the interaction is limited in the equilibrium level and the strain fields are not coupled in the constitution for nonlinear-inelastic material cases. Recent studies have developed simulation models that are able to predict shear behavior when compared to the classic Euler-Bernoulli and Timoshenko formulations.

The Modified Compression Field Theory (MCFT) [151] was proposed as a new approach capable of predicting the response of reinforced concrete elements to in-plane shear and axial stresses by considering equilibrium conditions, compatibility requirements, and stress-strain relationships. The concepts of MCFT was incorporated into an analytical model in finite element analysis of reinforced and prestressed concrete beams subjected to combined axial, flexural and shear loads [152]. The original formulations for two dimensional membrane elements are adapted to fiber representation of beam cross sections and an iterative algorithm was developed to predict the lateral and shear strains while establishing force equilibrium of two adjacent sections.

Bentz [16] coded the software framework Vector for the nonlinear analysis of two-dimensional reinforced concrete membrane structures incorporating a finite element algorithm based on a smeared, rotating crack model and a secant stiffness approach. Aquino and Erdem [11] implemented the MCFT using a tangential stiffness formulation into a finite element software and verified the analytical so-

lutions using experimental data in literature. In addition, a new material model was proposed to represent post-cracked concrete behavior easily programmed into finite element analysis [63].

However, beam-column elements have been more practical rather than solid finite elements due to computational efforts. Petrangeli et al. [117] proposed a new model that presents a local constitutive behavior for concrete a macromodel developed for fracture mechanics applications while still using a new methodology for fiber section model in beam-column elements. Mixed formulations for beam and frame element has been developed to couple shear and flexure while using variational strain and stress fields [141].

Chapter 3 – Methodology

To assemble the reliability analysis of the bridge components, methods adopted in the proposed procedure are detailed in this section.

3.1 Limitations and Objectives

Based on the literature review, several limitations in different disciplines are identified. The following objectives to remove these limitations define the aim of the study.

- Simulation methods require more evaluations of the performance function and more executions of finite element analysis when compared to FORM analysis. In addition, FORM is advantageous with importance measures of random variables in reliability analysis of bridge components. Therefore, a FORM analysis method will be considered to assess the effect of uncertain component properties and loads in reliability analysis of bridge components.
- FDM can lead to inaccurate search directions depending on the size of the parameter perturbations and cause computational effort while computing gradients in FORM. In order to provide accuracy and consistency in calculations, the DDM sensitivity, which does not require repetitive finite element analyses, will be adopted in the framework evaluating the limit state and its gradient at the same precision.

- The finite element framework, OpenSees, provides open-source approach to perform reliability applications. However, the DDM sensitivity formulations need to be verified for aleatory uncertainties in material, geometry and moving load parameters and epistemic uncertainties in integration methods.
- Meshing displacement-based elements yield discretization uncertainty in FERA. In addition, the moving load simulations on the coarse mesh of force-based finite elements is straightforward using integration approaches rather than relying on rigid body equilibrium in displacement-based elements. Thus, force-based frame element that ensures the force equilibrium without discretization error is chosen in reliability assessments. The objective is to use one force-based element whose integration points coincide with critical locations.
- OpenSees material library is currently limited to represent shear and flexural interaction in finite element analysis with force-based elements. Existing models such as linear elastic or non-linear uniaxial materials can not represent the behavior of shear dominant reinforced concrete bridge girders. Thus, a new simplified material model based on Modified Compression Field Theory will be implemented in the framework to couple axial and shear deformations in reinforced concrete girders. Material properties such as compressive strength of concrete will be treated as uncertain in finite element response and the derivative of constitutive equations will be implemented to OpenSees.
- While conservative in design, treating moment and shear separately can lead to non-conservative estimates of reliability. In order to define coupled moment-shear resistance boundaries for live loads, MCFT interaction surface

will be adopted in analyses.

- In force-based column elements, a single integration method is inadequate to represent both strain-softening and -hardening behavior of reinforced concrete columns subjected to extreme load cases. The existing integration methods and regularization methods needs a priori on the type of behavior. A new regularization technique will be proposed in order to represent strain-softening and -hardening behaviors without knowing a priori whether plasticity is localized or spread. However, the method introduces additional parameters to standard integration rules and contributes to modeling uncertainty. To assess the importance of the integration parameters relative to common sources of aleatory uncertainty, additional parameters will be considered as epistemic uncertainties in the reliability analysis of bridge columns.

3.2 Bridge Member Modeling in OpenSees

In finite element analysis, there are several formulations for frame elements such as displacement-based element [159], force-based element [21, 134], and the mixed formulations [9]. Comparisons by Hjelmstad and Taciroglu [62] show there is no clear winner among the three formulations; however, each has distinct advantages and disadvantages. Displacement-based formulation requires mesh refinement to maintain accuracy while using approximate displacement field along the element. However, since the length of a single element depends on the mesh geometry, discretization errors may lead to non-objective results. On the contrary, the force-based element does not require mesh refinement while interpolating section forces in terms of basic element forces. The element equilibrium equations are satisfied

even in nonlinear problems exactly and discretization errors are prevented in this approach [103].

The formulation of the force-based element implementations is given in [103] and the modeling hierarchy from general structure to fiber level in OpenSees Software Framework is shown in Fig. 3.1.

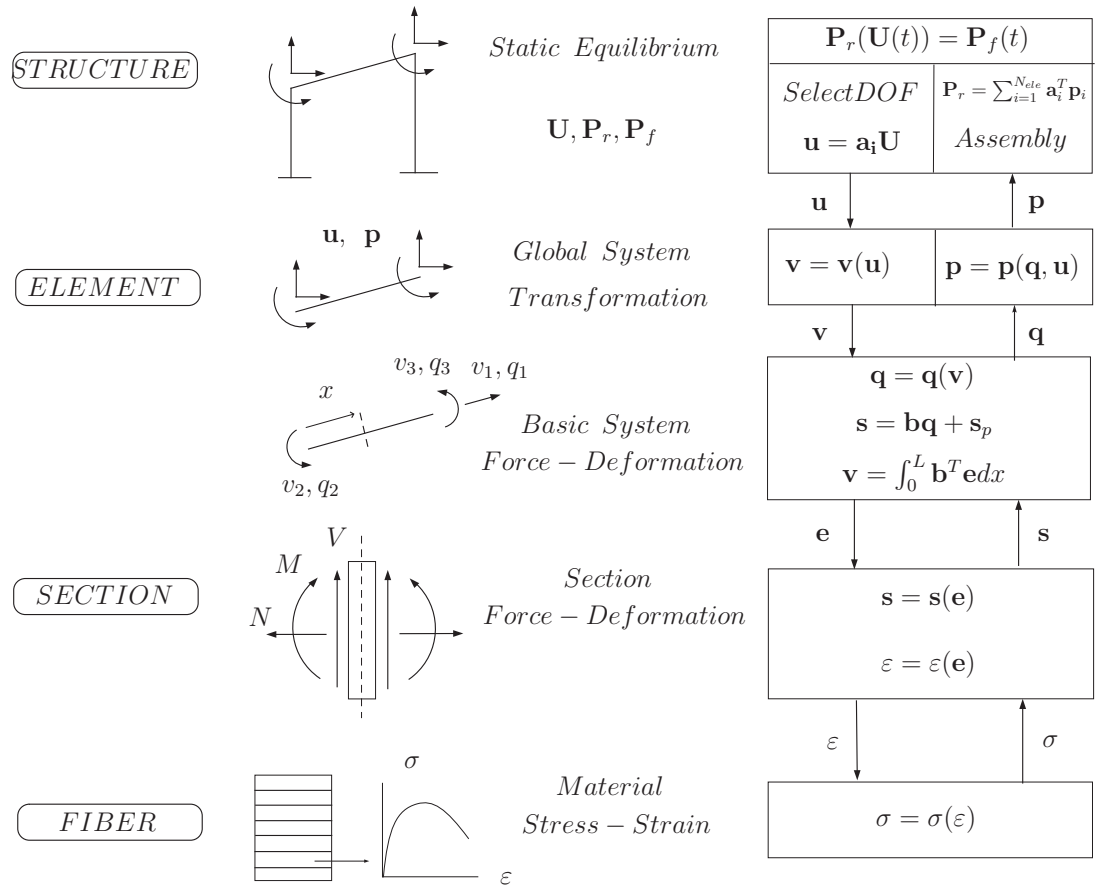


Figure 3.1: Modeling hierarchy for structural analysis in OpenSees [130]

The equilibrium and kinematic equations flow from the global system level to the fiber level through elements and sections. The resisting forces and nodal dis-

placements of elements in global system are contained in vectors \mathbf{p} and \mathbf{u} , respectively. In a basic system of beam-column elements, free of rigid body displacement modes, the element forces and corresponding deformations are contained in vectors \mathbf{q} and \mathbf{v} , respectively. The transformation of forces and displacements between basic and global systems are defined by the matrix \mathbf{a} of each element. The matrix \mathbf{a} represents the linear compatibility relationship between nodal displacements and basic system deformations when small displacement approach is assumed. At element level, the matrix \mathbf{b} describes the equilibrium relationship within the basic system. The compatibility relationship is obtained by integration of section deformations over the element. The section forces and deformations require the assembly of fiber constitution relationship. As the basic calculation order is summarized, the attention turns to the details of formulation in force-based elements subjected to moving loads.

In a general finite element setting, the most common approach to compute the moment and shear response of bridge girders is to subdivide each span into multiple elements with nodes corresponding to critical locations defined as sections where the failure due to moment-shear interaction may possibly occur and the response should be monitored. Using meshing displacement-based elements, moving loads are taken into account as statically equivalent nodal forces and the bending moment and shear force at each critical location are determined from rigid body equilibrium at the element ends. An alternative approach will be taken in this study, where each span is considered as one force-based element whose integration points coincide with critical locations. Furthermore, moving loads are taken into account as parts of the element, rather than nodal, equilibrium equations.

Force-based beam elements are formulated in terms of vectors, $\mathbf{q} = [N \ M_I \ M_J]^T$

and $\mathbf{v} = [\delta\theta_I \theta_J]^T$, that represent the end forces and end deformations, respectively, of the beam, as shown in Fig. 3.2. At every section along the element, there is an axial force, bending moment and shear force, $\mathbf{s}(x) = [N(x) \ M(x) \ V(x)]^T$, and the corresponding axial deformation, curvature and shear deformation, $\mathbf{e}(x) = [\varepsilon(x) \ \kappa(x) \ \gamma(x)]^T$.

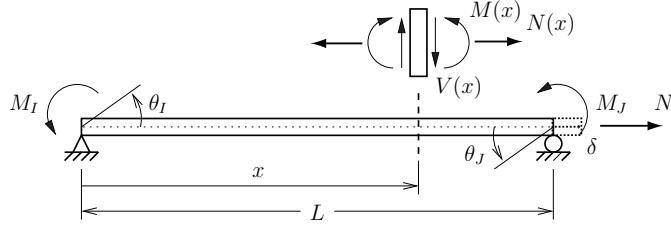


Figure 3.2: Simply-supported basic system for beam finite elements

Equilibrium between section forces, basic forces, and moving loads is satisfied in strong form:

$$\mathbf{s}(x) = \mathbf{b}(x)\mathbf{q} + \mathbf{s}_p(x) \quad (3.1)$$

The matrix, \mathbf{b} , contains interpolation functions for the moment and shear forces along the beam.

$$\mathbf{b}(x) = \begin{bmatrix} 1 & 0 & 0 \\ 0 & x/L - 1 & x/L \\ 0 & 1/L & 1/L \end{bmatrix} \quad (3.2)$$

The vector, \mathbf{s}_p , in Eq. (3.1) describes the section forces due to member loads. For the case of a moving point load, this vector is described in terms of the location and magnitude of the load in the basic system, as shown in Fig. 3.3.

Based on the principle of virtual forces, the element deformations, \mathbf{v} , are ob-

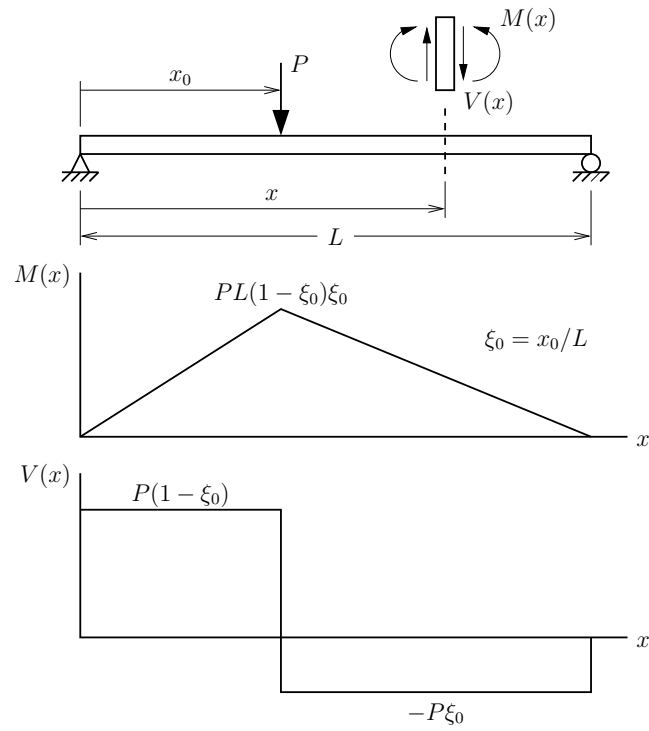


Figure 3.3: Bending moment and shear force developed in the basic system due to a moving transverse point load.

tained in terms of section deformations, \mathbf{e} , along the element.

$$\mathbf{v} = \sum_{j=1}^{N_p} \mathbf{b}_j^T \mathbf{e}_j w_j \quad (3.3)$$

where $\mathbf{b}_j \equiv \mathbf{b}(x_j)$ and $\mathbf{e}_j \equiv \mathbf{e}(x_j)$ are the interpolation function and the deformation evaluated at the j^{th} section along the element, with location, x_j , and integration weight, w_j .

The element flexibility matrix is obtained by linearization of Eq. (3.3) with respect to basic forces:

$$\mathbf{f} = \frac{\partial \mathbf{v}}{\partial \mathbf{q}} = \sum_{j=1}^{N_p} \mathbf{b}_j^T \mathbf{f}_{sj} \mathbf{b}_j w_j \quad (3.4)$$

where \mathbf{f}_s is the section flexibility matrix. The flexibility matrix in Eq. (3.4) is inverted to give the element stiffness matrix, $\mathbf{k} = \mathbf{f}^{-1}$, for subsequent assembly in the tangent stiffness matrix, \mathbf{K}_T . Eqs. (3.3) and (3.4) require numerical evaluations of integrals.

Several high order integration methods such as Gauss-Lobatto quadrature are available to evaluate the integrations. However, constructing integration methods via interpolatory quadrature [46] allows an analyst to control the location of sample points in force-based elements, which is advantageous for moving load analysis [72] and regularization [52]. For interpolatory quadrature, all integration point locations are specified and the corresponding integration weights are obtained from the following system of Vandermonde equations

$$\sum_{i=1}^N x_i^{j-1} w_i = \frac{L^j}{j} \quad (j = 1, \dots, N) \quad (3.5)$$

where $[0, L]$ is the interval of integration.

In addition to specifying all integration point locations, it is possible to specify the integration weights at selected points, e.g., to correspond to prescribed plastic hinge lengths. These N_c weights and their associated sample points are denoted w_{ci} and x_{ci} , respectively. The $N_f = N - N_c$ remaining integration points and weights are denoted x_{fi} and w_{fi} . Splitting the summation in Eq. (3.5) into separate sums over the N_c points with specified weights and the N_f points with unknown weights, then moving the known values to the right-hand side, leads to the following system of equations

$$\sum_{i=1}^{N_f} x_{fi}^{j-1} w_{fi} = \frac{L^j}{j} - \sum_{i=1}^{N_c} x_{ci}^{j-1} w_{ci} \quad (j = 1, \dots, N_f) \quad (3.6)$$

This reduced system of Vandermonde equations gives the remaining N_f weights required for evaluation of Eq. (3.3).

3.3 Reliability Method: FORM

A first-order reliability analysis will be carried out to assess the effect of uncertain girder properties and moving loads on the interaction of moment and shear force at critical girder locations.

The probability of failure, PF , in Eq. (2.3) is reformulated in terms of the uncertain parameters of finite element response [58]:

$$PF = \int \dots \int_{g < 0} f(\mathbf{\Phi}) d\mathbf{\Phi} \quad (3.7)$$

where $f(\mathbf{\Phi})$ is the joint probability density function for the random variables con-

tained in the vector Φ . The finite element response of bridge girders is contained in a response vector $\mathbf{U} = \mathbf{U}(\Phi)$. The limit state is defined in terms of the resistance \mathbf{R} and the demand \mathbf{S} that consist of uncertain parameters and structural response as:

$$g = \mathbf{R}(\Phi) - \mathbf{S}(\mathbf{U}(\Phi), \Phi) \quad (3.8)$$

Once mapping of random variables, Φ , having non-normal distributions and correlations, into a standard space of uncorrelated reduced variables, $\mathbf{Y}(\Phi)$ using the Nataf transformation [81], the integral is approximated by a hyperplane in the transformed space $\mathbf{Y} = \mathbf{Y}(\Phi)$ of uncorrelated and normally distributed random variables.

To compute the probability integral, the HLRF method [82] providing a line search scheme with a step size while optimizing design point will be used in the reliability analysis. The HLRF algorithm does not assume the trial point is located on the limit state surface. The distance between two successive iteration steps was defined in terms of directional cosines of the previous step [58]:

$$\mathbf{Y}_{k+1} = \mathbf{Y}_k + s\mathbf{d}_k \quad (3.9)$$

$$\mathbf{d}_k = \left[\frac{g(\mathbf{Y}_k)}{\|\nabla g(\mathbf{Y}_k)\|} + \alpha_k \mathbf{Y}_k \right] \alpha_k^T - \mathbf{Y}_k \quad (3.10)$$

where $\mathbf{Y}_k = \{y_i\}$; α_k is the direction cosine vector; and $\frac{g}{\|\nabla g\|}$ is the gradient norm vector. The factor, s , adjusts the step size at each iteration in the analysis where the Armijo rule can be employed to select a step size minimizing the value of a merit function along the search direction [84]. The iteration continues until a the step size converges to zero while the design point satisfies the limit state equation with enough tolerance.

For linearization of limit state and using the gradient-based search algorithms, the gradient of limit state functions, $\nabla g(\Phi) = \partial\Phi/\partial\mathbf{Y}$, needs to be computed. Using the chain rule of derivation is applied, the required gradient required in the improved HLRF algorithm [82] has the form:

$$\frac{\partial g}{\partial \mathbf{Y}} = \frac{\partial g}{\partial \mathbf{U}} \frac{\partial \mathbf{U}}{\partial \Phi} \frac{\partial \Phi}{\partial \mathbf{Y}}. \quad (3.11)$$

The derivative of limit state function with respect to response quantities, $\partial g/\partial \mathbf{U}$ is easy to compute algebraically. The gradient of uncertain parameters with respect to transformed variables is calculated as the Jacobian of Nataf transformation, $\partial\Phi/\partial\mathbf{Y}$ and the computational tools are already installed in OpenSees [81]. The gradient, $\partial\mathbf{U}/\partial\varphi$, is the response sensitivity and needs to be computed in the finite element analysis. The sensitivity formulation in element, section and fiber level of OpenSees needs to be implemented.

The optimization problem given in Eq. (2.11) will be taken care of using the design point search iteration solver already installed in OpenSees [58]. Once the design point is obtained the reliability index in the hyperplane of \mathbf{Y} is the defined as:

$$\beta = \| \mathbf{Y}^* \| \quad (3.12)$$

where the probability of failure is calculated by the standard normal CDF for $-\beta$. The gradient projection-based iterations continue until the reliability index, β , converges. In general, the mean value of original random variables are appropriate to start the first step. Using the gradient of limit state function, directional cosines, α_i , are evaluated for each variable at each step iteration of design point [58]; so that the first step of the iteration is concluded with the updated design point

coordinates. The alpha vector has the form:

$$\alpha_i = -\frac{\frac{\partial g(\mathbf{Y}^*)}{\partial y_i}}{\|\nabla g(\mathbf{Y}^*)\|} \quad (3.13)$$

and at design point reliability index can be written in terms of this vector:

$$\beta = \alpha \mathbf{Y}^* \quad (3.14)$$

The alpha vector contains the contribution of each random variable on β , however \mathbf{Y} contents are uncorrelated and normally distributed. For the correlated non-normal random variables, Haukaas and Der Kiureghian [58] computes the importance ranks as:

$$\gamma = -\frac{\partial g}{\partial \mathbf{Y}} \mathbf{J}_{\mathbf{Y}^*, \Phi^*} \sqrt{\text{diag}(\mathbf{J}_{\mathbf{Y}^*, \Phi^*}^{-1} \mathbf{J}_{\mathbf{Y}^*, \Phi^*}^{-T})} \quad (3.15)$$

where $\mathbf{J}_{\mathbf{Y}^*, \Phi^*}$ is the Jacobian of transformation at design point. The total of each vector is scaled to one, i.e. $\|\alpha\| = 1$ and $\|\gamma\| = 1$. In addition, the negative value of importance rank γ indicates the resistance variable.

The random variables in resistance and demand portion of limit state function is investigated according to the source of uncertainty and the importance ranks will be obtained. Eventually, a discussion on the influence of uncertainties on probability of failure will be started in the light of the output data from numerical examples.

3.3.1 Aleatory Uncertainty

In FERA of bridge structures, the characterization of uncertain parameters is an important task. As in the early sections of the proposed study, the uncertainty is divided into two groups according to its source. Since the major problem in non-seismic bridge safety applications occurs due to live loads, the safety of bridge components against the heavy truck loading will be considered. Aleatory uncertainty in bridge structures will be considered as geometry and material parameters and additionally the variation in axle weights is taken as uncertainty.

The proposed method of reliability analysis allows the analyst to use continuous probability density functions formulated by the mean value and the standard deviation of the uncertain variable. As listed in Table 3.1, the documented measurements will be the base to define second-moment parameters of variation while undocumented properties such as effective width, shear modulus and concrete tensile strength are assumed similar variations with related material and shape parameters. The influence of uncertain parameters on both finite element analysis demand and resisting side of performance function will be investigated. The model for uncertainty due to measurement and fabrication error is implemented as user-defined variations to OpenSees framework so that the random variables on parameters can be assigned to use in custom variations to represent conditions in deterioration, fatigue and retrofit analyses.

3.3.2 Epistemic Uncertainty

Since the force-based beam-column element is proposed to model bridge components, the numerical procedures to evaluate idealized mathematical relationship

Table 3.1: Parameter variations in documented measurements

	Parameter	Distribution	C.O.V	Reference
<i>Concrete</i>				
Young's modulus	E_c	lognormal	0.08	[36]
Compressive strength	f_c	normal	0.15	[97]
<i>Steel</i>				
Young's modulus	E_s	lognormal	0.06	[98]
Yield strength	f_y	lognormal	0.12	[98]
<i>Geometry</i>				
Section depth	d	normal	0.015	[99]
Section width	b_w	normal	0.015	[99]
Deck thickness	h_f	normal	0.015	[99]
Neg. r/f steel area	A_s^-	normal	0.024	[99]
Pos. r/f steel area	A_s^+	normal	0.024	[99]
Transverse steel area	A_v	normal	0.024	[99]
Stirrup spacing	s	normal	0.10	[146]
<i>Loads</i>				
Axle weight	P_i	lognormal	0.20	[13]
Dead load	DL	lognormal	0.10	[106]

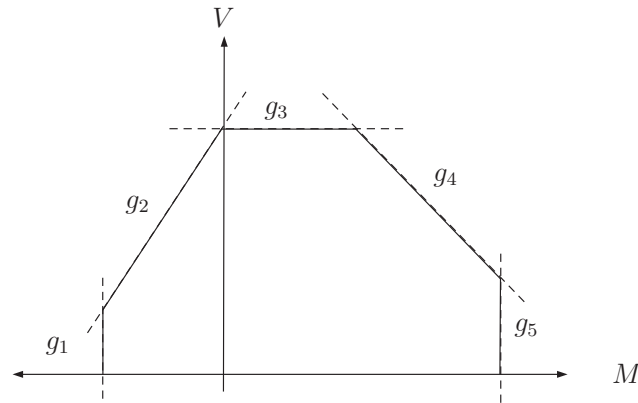
will generate the major modeling uncertainty in the proposed study. The global response of bridge components is dependent on the numerical integration parameters, weight w and location x of each Gauss point. This study develops analytic sensitivity by DDM for one dimensional interpolatory quadrature, which is a generalization of most integration methods proposed for force-based frame elements. These developments allow modeling uncertainty associated with numerical integration in force-based elements to be assessed via stand-alone sensitivity analysis. For the reliability analysis of the bridge columns, a regularized integration method that will be proposed in following sections treats plastic hinge length and point locations as uncertain parameters.

Furthermore, for the bridge girders, the integration points coincide with the user-defined critical girder sections so that, the point locations are selected as deterministic quantities. However, bending moment and shear force from the two dimensional finite element analysis modified by the impact factor, IF , the moment distribution factor DFM and the shear distribution factor DFV . These factors are treated as a modeling uncertainty represented by using random variables with normal distribution and mean values from LRFR specifications [2].

Using the importance measures, the epistemic and aleatory uncertainty parameters will be distinguished with respect to their influence on probability of failure. The uncertain parameters having negligible influence on the most probable failure mode can be ignored to decrease the computational effort. As a result, the measurement will help reducing the number of random variables.

3.3.3 Performance Function

The live load reliability software provides two performance function options in bridge girder analysis. The first approach for the limit state consists of multi-linear interaction diagram obtained by AASHTO-MCFT formulations [3]. The AASHTO code provides an accurate method to compute component resistance. The ultimate moment-shear couple that can be carried by a section is computed using the general procedure in AASHTO-LRFD Article (5.8.3.4.2). The shear-moment capacity of AASHTO-MCFT is represented by 6 critical points and a linear interpolation connecting these points. Each linearized portion of the closed curve will be considered as the limit values of moment and shear interaction as shown in Fig. 3.4.



Six – point Representation of AASHTO – MCFT

Figure 3.4: MB performance functions

This approach requires computation of multi reliability indices and consequently, the minimum index will be considered as the critical index that gives

the analyst information whether the failure mode is shear, flexural or combined. Using the Multi-Beta (MB) approach, five linear equations are considered as 5 limit states in reliability analysis. Each line analytically describes the limit state in a form:

$$g_i = cf_{m_i}M + cf_{v_i}V + cf_{n_i} \quad (3.16)$$

where cf_m , cf_v and cf_n are coefficients of line equations in moment (M) - shear (V) space. The failure occurs when a moment-shear demand stays outside of the capacity curve so that, the safety is ensured with a analytical inequality:

$$g_i < 0 \quad (3.17)$$

To compute the line coefficients, the ultimate shear-moment values are calculated in AASHTO as:

$$M_n = A_s f_{yt} d_v \quad (3.18a)$$

$$V_n = \beta^* \sqrt{f'_c} b_w d_v + \frac{A_v f_{yv} d_v}{s \tan(\theta^*)} \quad (3.18b)$$

where two important parameters are introduced by the code to calculate shear resistance of a reinforced concrete section. The factor, β^* , indicates the ability of diagonally cracked concrete to transmit tension stress while the diagonal compressive stresses are inclined with the angle θ^* . The computation steps and $\beta^* - \theta^*$ interactions are detailed in a coded procedure, *AASHTO_MCFT Capacity Function* given in Appendix section (A.1). The MB approach is implemented to OpenSees in this function where the MCFT parameters β^* and θ^* are interpolated for every realization of the uncertain material and geometry parameters. The MB function

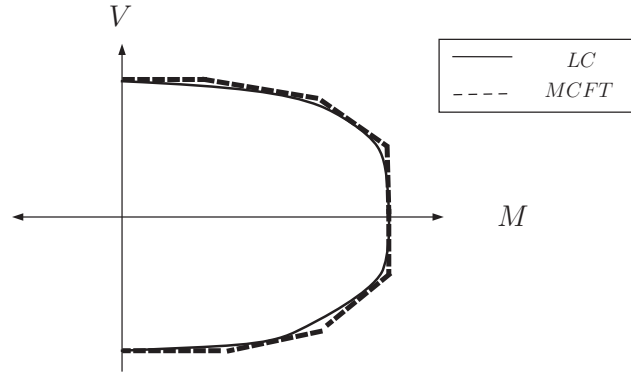
is employed as the section resistance in limit state to represent the probabilistic variation of line equation parameters, slope and constant, in M-V space for each portion.

The second approach in live load reliability examples will be the representation of the limit state using a Lamé curve (LC) that has a continuous closed form. Hamutcuoglu and Scott [52] proposed this capacity function for the live load reliability analysis of bridge girders considering coupled shear and moment. The approach taken herein is to define the limit state as a smooth Lamé curve [48]:

$$g = 1 - \left| \frac{M}{M_n} \right|^3 - \left| \frac{V}{V_n} \right|^3 \quad (3.19)$$

LC approach represents the simplified procedure for non-prestressed section given in AASHTO-MCFT Article (5.8.3.4.1). This procedure is recommended for concrete sections not subjected to axial tension and containing at least minimum amount of transverse reinforcement [3]. The nominal capacities, M_n and V_n , that describe the shape of the Lamé curve are given by peak values from MCFT analysis where β^* and θ^* are taken as 2.0 and 45°.

As shown in Fig. 3.5, the smooth Lamé curve approximates the general shape of a multi-linear MCFT interaction surface. The exponent in Eq. (3.19) can be adjusted to change the shape of the curve. All parameters that define M_n and V_n are treated as random variables with their distribution properties. For the mean values of material properties and reinforcing details of girder sections, the MCFT parameters $\beta^*-\theta^*$ in Eq. (3.18b) remain deterministic during the analysis; however, the moment and shear capacities, and accordingly the shape of the Lamé curve, will change during the analysis for every realization of the uncertain parameters



LC Approximation of MCFT

Figure 3.5: LC performance function

in Eq. (3.18).

LC approach simplifies the live load reliability analysis procedure reducing the total number of performance functions to be solved in FERA of reinforced concrete girders. When compared to MB approach using multi-line equations, LC reduces the computation effort using the closed form approximation.

3.4 Response Sensitivity: DDM

Several algorithms are available to solve reliability problems and their common characteristic is the need to compute the gradient of the structural response, or response sensitivity, in order to find the failure point. When finite element analysis is used to evaluate the performance function for reliability methods, it is often difficult to implement necessary gradient computations of the finite element response.

In this section of the methodology, the use of well-established response sensitivity modules of OpenSees will be proposed to obtain gradients in the reliability

assessments. Following the hierarchy of system equations, the response sensitivity will be derived in global, basic system and section level formulations.

3.4.1 Global Response Sensitivity

Response sensitivity calculations by the DDM consist of analytical differentiation of the equations that govern the structural response. In this study, the structural response is found by solving the equations of static equilibrium. Impact factors approximate dynamic load effects. The equilibrium equations are described in terms of the vector, Φ , which contains the uncertain material, geometric and load parameters of a structural model.

$$\mathbf{P}_r(\mathbf{U}(\Phi), \Phi) = \mathbf{P}_f(\Phi) \quad (3.20)$$

The nodal displacement vector, $\mathbf{U}(\Phi)$, depends on the parameters, Φ , and load history. The resisting force vector, \mathbf{P}_r , which is assembled from element contributions by standard finite element procedures, depends on the structural parameters explicitly, as well as implicitly via the nodal displacements. The vector, \mathbf{P}_f , contains nodal loads, which also may depend on the parameters in Φ which evolve as a function of time for moving loads.

Considering the chain rule of differentiation, the derivative of Eq. (3.20) with respect to a single parameter, φ , in Φ , is:

$$\mathbf{K}_T \frac{\partial \mathbf{U}}{\partial \varphi} + \frac{\partial \mathbf{P}_r}{\partial \varphi} \bigg|_{\mathbf{U}} = \frac{\partial \mathbf{P}_f}{\partial \varphi} \quad (3.21)$$

where the tangent stiffness matrix, $\mathbf{K}_T = \partial \mathbf{P}_r / \partial \mathbf{U}$, is the partial derivative of the

resisting force vector with respect to the nodal displacements. The derivative of the nodal load vector, $\partial \mathbf{P}_f / \partial \varphi$, is nonzero only if the parameter, φ , represents a nodal load. The vector, $\partial \mathbf{P}_r / \partial \varphi|_{\mathbf{U}}$, is the conditional derivative of the resisting force vector under the condition that the nodal displacements \mathbf{U} are held fixed. This vector is assembled from the conditional derivative of local forces, $\partial \mathbf{q} / \partial \varphi|_{\mathbf{v}}$, from each element in the structural model in the same manner as the resisting force vector itself.

The nodal response sensitivity is then found by solving the following system of linear equations:

$$\frac{\partial \mathbf{U}}{\partial \varphi} = \mathbf{K}_T^{-1} \left(\frac{\partial \mathbf{P}_f}{\partial \varphi} - \frac{\partial \mathbf{P}_r}{\partial \varphi} \Big|_{\mathbf{U}} \right) \quad (3.22)$$

This solution is repeated for each parameter in the vector Φ , reusing the factorization of \mathbf{K}_T . The assembly of element force sensitivity, $\frac{\partial \mathbf{P}_r}{\partial \varphi} \Big|_{\mathbf{U}}$, requires the derivative of force vector \mathbf{p} of each element.

$$\frac{\partial \mathbf{P}_r}{\partial \varphi} \Big|_{\mathbf{U}} = \bigcup_{Nele} \frac{\partial \mathbf{p}}{\partial \varphi} \Big|_{\mathbf{u}} \quad (3.23)$$

where the operation \cup is the assembly over elements and \mathbf{u} is the displacement vector of each element. The global element forces and displacements are derived through the transformation matrix:

$$\frac{\partial \mathbf{p}}{\partial \varphi} = \mathbf{a}^T \frac{\partial \mathbf{q}}{\partial \varphi} + \frac{\partial \mathbf{a}^T}{\partial \varphi} \mathbf{q} \quad (3.24)$$

$$\frac{\partial \mathbf{v}}{\partial \varphi} = \mathbf{a} \frac{\partial \mathbf{u}}{\partial \varphi} + \frac{\partial \mathbf{a}}{\partial \varphi} \mathbf{u} \quad (3.25)$$

The derivatives are completed when the conditional derivatives are calculated:

$$\frac{\partial \mathbf{p}}{\partial \varphi} = \frac{\partial \mathbf{p}}{\partial \mathbf{u}} \frac{\partial \mathbf{u}}{\partial \varphi} + \left. \frac{\partial \mathbf{p}}{\partial \varphi} \right|_{\mathbf{u}} \quad (3.26)$$

$$\frac{\partial \mathbf{q}}{\partial \varphi} = \frac{\partial \mathbf{q}}{\partial \mathbf{v}} \frac{\partial \mathbf{v}}{\partial \varphi} + \left. \frac{\partial \mathbf{q}}{\partial \varphi} \right|_{\mathbf{v}} \quad (3.27)$$

To reduce the unknowns, Eqs. (3.26) and (3.27) are inserted in the derivative of global element forces Eq. (3.24) and then combined with Eq. (3.25):

$$\mathbf{k}_g \frac{\partial \mathbf{u}}{\partial \varphi} + \left. \frac{\partial \mathbf{p}}{\partial \varphi} \right|_{\mathbf{u}} = \mathbf{a}^T \mathbf{k}_b \mathbf{a} \frac{\partial \mathbf{u}}{\partial \varphi} + \mathbf{a}^T \mathbf{k}_b \frac{\partial \mathbf{a}}{\partial \varphi} \mathbf{u} + \mathbf{a}^T \left. \frac{\partial \mathbf{q}}{\partial \varphi} \right|_{\mathbf{v}} + \frac{\partial \mathbf{a}^T}{\partial \varphi} \mathbf{q} \quad (3.28)$$

where $\mathbf{k}_g = \partial \mathbf{p} / \partial \mathbf{u}$ and $\mathbf{k}_b = \partial \mathbf{q} / \partial \mathbf{v}$ are global and basic system stiffness matrices, respectively. Considering $\mathbf{k}_g = \mathbf{a}^T \mathbf{k}_b \mathbf{a}$, Eq. (3.28) is simplified by canceling the terms with $\partial \mathbf{u} / \partial \varphi$ and the expression takes the form:

$$\left. \frac{\partial \mathbf{p}}{\partial \varphi} \right|_{\mathbf{u}} = \mathbf{a}^T \mathbf{k}_b \frac{\partial \mathbf{a}}{\partial \varphi} \mathbf{u} + \mathbf{a}^T \left. \frac{\partial \mathbf{q}}{\partial \varphi} \right|_{\mathbf{v}} + \frac{\partial \mathbf{a}^T}{\partial \varphi} \mathbf{q} \quad (3.29)$$

The sensitivity of transformation matrix is equal to zero when φ is any parameter other than a nodal coordinate. The conditional derivative $\partial \mathbf{q} / \partial \varphi|_{\mathbf{v}}$ is calculated through sections of basic system for material and sectional geometry parameters.

3.4.2 Force-Based Element Response Sensitivity

The DDM formulations will cover the gradient of section forces, fixed-end forces, force interpolation functions and integration weights. The section equilibrium

relationship of Eq. (3.1) will be differentiated with respect to a single parameter, φ :

$$\frac{\partial \mathbf{s}}{\partial \varphi} = \frac{\partial \mathbf{b}}{\partial \varphi} \mathbf{q} + \mathbf{b} \frac{\partial \mathbf{q}}{\partial \varphi} + \frac{\partial \mathbf{s}_p}{\partial \varphi} \quad (3.30)$$

Eq. (3.30) is expanded in terms of the derivatives $\partial \mathbf{q} / \partial \varphi = \mathbf{k} \partial \mathbf{v} / \partial \varphi + \partial \mathbf{q} / \partial \varphi|_{\mathbf{v}}$ and $\partial \mathbf{s} / \partial \varphi = \mathbf{k}_s \partial \mathbf{e} / \partial \varphi + \partial \mathbf{s} / \partial \varphi|_{\mathbf{e}}$ of the basic and section forces, respectively:

$$\mathbf{k}_s \frac{\partial \mathbf{e}}{\partial \varphi} + \frac{\partial \mathbf{s}}{\partial \varphi} \Big|_{\mathbf{e}} = \frac{\partial \mathbf{b}}{\partial \varphi} \mathbf{q} + \mathbf{b} \left(\mathbf{k} \frac{\partial \mathbf{v}}{\partial \varphi} + \frac{\partial \mathbf{q}}{\partial \varphi} \Big|_{\mathbf{v}} \right) + \frac{\partial \mathbf{s}_p}{\partial \varphi} \quad (3.31)$$

where $\mathbf{k}_s = \partial \mathbf{s} / \partial \mathbf{e}$ and $\mathbf{k} = \partial \mathbf{q} / \partial \mathbf{v}$ define the section and element stiffness matrix, respectively. The conditional derivative $\partial \mathbf{q} / \partial \varphi|_{\mathbf{v}}$ cannot be obtained directly from Eq. (3.31). To circumvent this restriction, the derivative of the element compatibility relationship in Eq. (3.3) is differentiated with respect to φ :

$$\frac{\partial \mathbf{v}}{\partial \varphi} = \sum_{j=1}^{N_p} \mathbf{b}_j^T \frac{\partial \mathbf{e}_j}{\partial \varphi} w_j \quad (3.32)$$

Then, the derivative of the section deformations is obtained from Eq. (3.31)

$$\frac{\partial \mathbf{e}}{\partial \varphi} = \mathbf{f}_s \mathbf{b} \mathbf{k} \frac{\partial \mathbf{v}}{\partial \varphi} + \mathbf{f}_s \left(\mathbf{b} \frac{\partial \mathbf{q}}{\partial \varphi} \Big|_{\mathbf{v}} + \frac{\partial \mathbf{s}_p}{\partial \varphi} - \frac{\partial \mathbf{s}}{\partial \varphi} \Big|_{\mathbf{e}} \right) \quad (3.33)$$

and combined with Eq. (3.32) to give the following expression:

$$\frac{\partial \mathbf{v}}{\partial \varphi} = \sum_{j=1}^{N_p} \mathbf{b}_j^T \mathbf{f}_{sj} \left(\mathbf{b}_j \mathbf{k} \frac{\partial \mathbf{v}}{\partial \varphi} + \mathbf{b}_j \frac{\partial \mathbf{q}}{\partial \varphi} \Big|_{\mathbf{v}} + \frac{\partial \mathbf{s}_{pj}}{\partial \varphi} - \frac{\partial \mathbf{s}_j}{\partial \varphi} \Big|_{\mathbf{e}} \right) w_j \quad (3.34)$$

From the definition of the element flexibility matrix in Eq. (3.4), the expression $(\sum \mathbf{b}^T \mathbf{f}_s \mathbf{b} w) \mathbf{k}$ is equal to the identity, and the conditional derivative of the basic

forces can be reduced to

$$\left. \frac{\partial \mathbf{q}}{\partial \varphi} \right|_{\mathbf{v}} = \mathbf{k} \sum_{i=1}^{N_p} \mathbf{b}^T \mathbf{f}_s \left(\left. \frac{\partial \mathbf{s}}{\partial \varphi} \right|_{\mathbf{e}} - \frac{\partial \mathbf{s}_{p_i}}{\partial \varphi} - \frac{\partial \mathbf{b}}{\partial \varphi} \mathbf{q} \right) w_i - \mathbf{k} \sum_{i=1}^{N_p} \left(\frac{\partial \mathbf{b}^T}{\partial \varphi} \mathbf{e} w_i + \mathbf{b}^T \mathbf{e} \frac{\partial w_i}{\partial \varphi} \right) \quad (3.35)$$

where $\partial \mathbf{s}_{p_i} / \partial \varphi$ contains the derivative of the axial force, bending moment and shear with respect to i^{th} point load parameter. The axial force sensitivity is equal to zero and the derivative of moment and shear functions in terms of section locations ξ_0 is shown in Fig. 3.6.

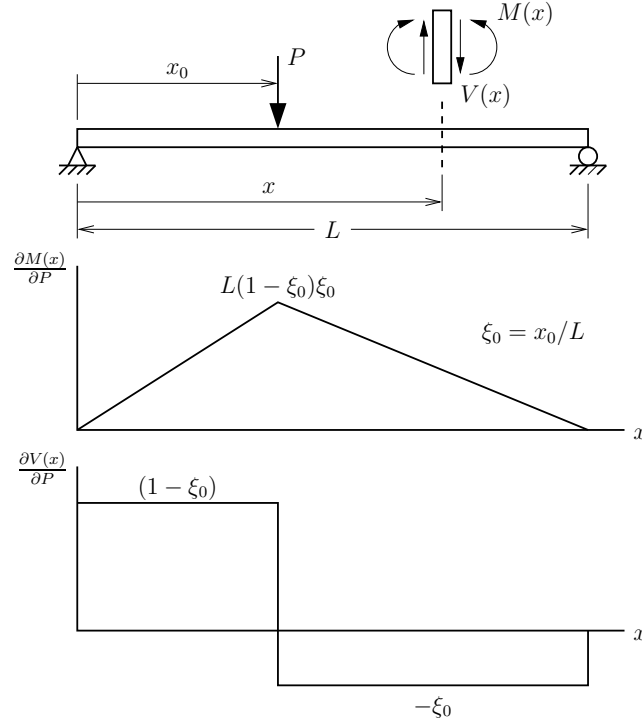


Figure 3.6: Derivative of bending moment and shear force in the basic system with respect to point load.

The target gradient $\partial \mathbf{q} / \partial \varphi|_{\mathbf{v}}$ is formulated in terms of section force derivative

vector $\partial \mathbf{s} / \partial \varphi|_{\mathbf{e}}$. In addition, to compute the gradient at element level, the DDM formulation requires the numerical integration of forces at sections along the element. In the context of this study, the section force derivative vector, $\partial \mathbf{s} / \partial \varphi|_{\mathbf{e}}$, is crucial to formulate analytical response sensitivity of aleatory uncertainties in bridge girder components.

Interpolatory quadrature sensitivity needs to be formulated to consider a significant modeling uncertainty in force-based column elements subjected to extreme loadings. The required response sensitivity formulations will be derived at section level for bridge girders in Chapter 4 and interpolatory quadrature sensitivity will be formulated in bridge columns in Chapter 5.

Chapter 4 – Reinforced Concrete Bridge Girder Sensitivity and Reliability

The finite element response sensitivity formulation is continued for aleatory uncertainties considered in live-load reliability analysis of bridge girders. The section force vector $\partial \mathbf{s} / \partial \varphi|_{\mathbf{e}}$ is quantified for material and geometric parameters. Implementations of new objects to OpenSees and the commanding scripts for the proposed live-load reliability analysis framework in Tcl will be detailed in this section. Verification of DDM sensitivity is followed by live-load reliability examples to present features of new reliability analysis software framework.

4.1 Section Response Sensitivity

The conditional derivative, $\partial \mathbf{s} / \partial \varphi|_{\mathbf{e}}$, depends on how the section forces are computed by assembling fiber forces. There is a variety of approaches to compute the forces at each girder cross-section: elastic constants, closed-form solutions for a particular reinforcing pattern, and fiber discretization. To facilitate DDM computations for a wide array of longitudinal reinforcing details and material properties, a fiber discretization is employed to compute the section bending moment and shear force. The numerical integral is evaluated over a user-defined number of fibers, N_f , with area, A_k , and distance, y_k , from a reference axis:

$$\mathbf{s} = \sum_{k=1}^{N_f} \mathbf{a}_s^T \boldsymbol{\sigma}_k A_k \quad (4.1)$$

where the matrix \mathbf{a}_s relates the section deformations to fiber deformations in compatibility equation:

$$\boldsymbol{\varepsilon}_k = \mathbf{a}_s \mathbf{e} \quad (4.2)$$

where $\mathbf{e} = [\varepsilon \ \kappa \ \gamma]^T$ is the section deformation vector and $\boldsymbol{\varepsilon} = [\varepsilon_k \ \gamma_k]^T$ is the vector holding strains at fiber k .

The fiber stress vector, $\boldsymbol{\sigma}_k$, which contains axial σ_k and shear τ_k stresses is computed from the fiber strains, which is a function of the section curvature and axial deformation, $\varepsilon_k = \varepsilon_0 - y_k \kappa$, and shear deformation, γ_k , so that the compatibility matrix has the form:

$$\mathbf{a}_s = \begin{bmatrix} 1 & -y & 0 \\ 0 & 0 & 1 \end{bmatrix} \quad (4.3)$$

The axial force, bending moment and shear force are combined to form the section force vector using uni- or bi-axial material models.

4.1.1 Uniaxial Section Model Sensitivity

In this approach, axial-flexural behavior is represented by uniaxial material models in section stress-strain relationships. The material model can be chosen either elastic or inelastic. The section force vector with aggregated shear has the form:

$$\mathbf{s} = \begin{bmatrix} N(x) \\ M(x) \\ V(x) \end{bmatrix} = \begin{bmatrix} \sum_{k=1}^{N_f} \sigma_k A_k \\ \sum_{k=1}^{N_f} y_k \sigma_k A_k \\ G(x) F(x) \gamma(x) \end{bmatrix} \quad (4.4)$$

where the section shear force is assumed to be linear-elastic, as described by the shear modulus, G , and shear area, F .

The aggregation of section forces in Eq. (4.4) highlights the ease with which shear deformation is included in force-based elements [125, 89]. Approximate displacement fields are not necessary, as is the case with a Timoshenko formulation of combined flexural and shear response. The derivative of Eq. (4.4) under the condition of fixed section deformations is equal to:

$$\left. \frac{\partial \mathbf{s}}{\partial \varphi} \right|_{\mathbf{e}} = \begin{bmatrix} \sum_{k=1}^{N_f} \left[\left. \frac{\partial \sigma_k}{\partial \varphi} \right|_{\varepsilon_k} A_k + \sigma_k \frac{\partial A_k}{\partial \varphi} \right] \\ \sum_{k=1}^{N_f} \left[\frac{\partial y_k}{\partial \varphi} \sigma_k A_k + y_k \left. \frac{\partial \sigma_k}{\partial \varphi} \right|_{\varepsilon_k} A_k + y_k \sigma_k \frac{\partial A_k}{\partial \varphi} \right] \\ \left(\frac{\partial G}{\partial \varphi} F + G \frac{\partial F}{\partial \varphi} \right) \gamma \end{bmatrix} \quad (4.5)$$

For each fiber k , the axial stress gradient, $\partial \sigma_k / \partial \varphi|_{\varepsilon_k}$, is calculated for the constant strains in constitution formulations in terms of material parameters of the concrete and reinforcing steel materials. In order to compute the gradients $\partial A_k / \partial \varphi$ and $\partial y_k / \partial \varphi$, the fiber areas and locations are derived with respect to the shape parameters that define the section geometry.

4.1.2 Biaxial Section Model Sensitivity

In this section model, a biaxial material with coupled axial-shear behavior will be applied for each fibers. In contrast to aggregated shear stiffness, axial-shear interaction is obtained in fiber level; however, an approximate shear displacement field is necessary. The section force vector has the form:

$$\mathbf{s} = \begin{bmatrix} N(x) \\ M(x) \\ V(x) \end{bmatrix} = \begin{bmatrix} \sum_{k=1}^{N_f} \sigma_k A_k \\ \sum_{k=1}^{N_f} y_k \sigma_k A_k \\ \sum_{k=1}^{N_f} \gamma_k A_k \end{bmatrix} \quad (4.6)$$

It can easily be shown that the derivative of Eq. (4.6) under the condition of fixed section deformations is equal to:

$$\frac{\partial \mathbf{s}}{\partial \varphi} \Big|_{\mathbf{e}} = \begin{bmatrix} \sum_{k=1}^{N_f} \left[\frac{\partial \sigma_k}{\partial \varphi} \Big|_{\varepsilon_k} A_k + \sigma_k \frac{\partial A_k}{\partial \varphi} \right] \\ \sum_{k=1}^{N_f} \left[\frac{\partial y_k}{\partial \varphi} \sigma_k A_k + y_k \frac{\partial \sigma_k}{\partial \varphi} \Big|_{\varepsilon_k} A_k + y_k \sigma_k \frac{\partial A_k}{\partial \varphi} \right] \\ \sum_{k=1}^{N_f} \left[\frac{\partial \tau_k}{\partial \varphi} \Big|_{\gamma_k} A_k + \tau_k \frac{\partial A_k}{\partial \varphi} \right] \end{bmatrix} \quad (4.7)$$

The shear stress is calculated on each fiber k , both axial and shear stress gradients, $\partial \sigma_k / \partial \varphi|_{\varepsilon_k}$ and $\partial \tau_k / \partial \varphi|_{\varepsilon_k}$, are obtained for the constrained strains in constitution formulations. The computation of the shape gradients $\partial A_k / \partial \varphi$ and $\partial y_k / \partial \varphi$ is required for each fiber.

A biaxial material considering axial-shear interaction and a T-beam section integration model are detailed and the required section force sensitivity is obtained in following sections. Implementations of the gradient computations will be performed for material, geometry, load and integration parameters that are applied as φ in Eqs. (4.5) and (4.7).

4.2 Biaxial MCFT Material Model

Currently, for force-based elements in OpenSees, shear stress and deformations can be monitored by only using a uniaxial section model so that axial-flexural deformations do not interact with shear deformations. The concepts of MCFT are implemented to OpenSees in a biaxial material model and details of a new fiber mechanism that can couple shear and moment deformation fields are proposed in this section.

The new material incorporates one additional strain field to be monitored at fiber-discretized cross section. As shown in Fig. 4.1, the shear deformations are formulated in the section mechanics while the lateral strain field ε_y is obtained implicitly by imposing vertical force equilibrium between transverse reinforcement and concrete in each fiber [117]. The section deformation field is given as

$$\mathbf{e} = \begin{bmatrix} \varepsilon \\ \kappa \\ \gamma \end{bmatrix} \quad (4.8)$$

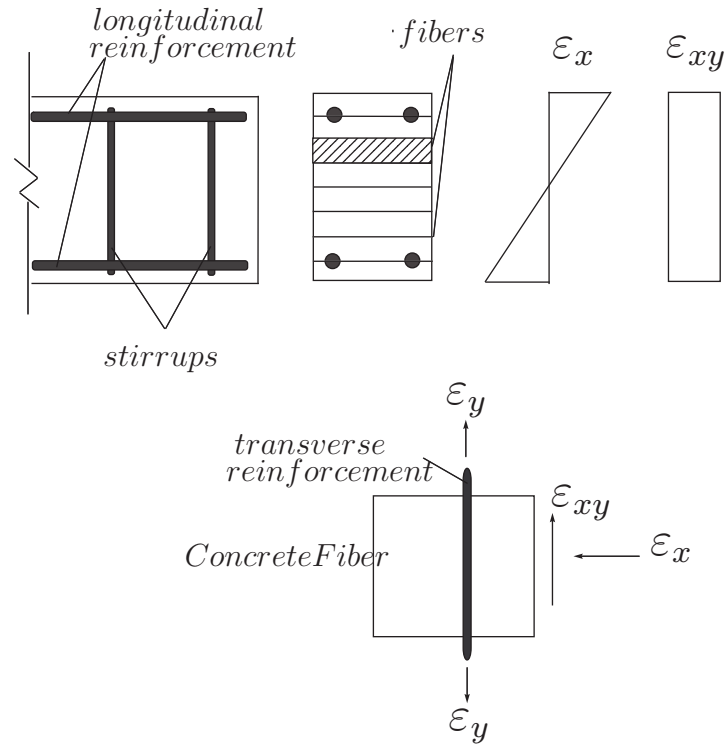


Figure 4.1: Section mechanics and strain fields

For the longitudinal strain field (parallel to the beam axis), the plane section hypothesis has been retained, whereas several shear shape functions can be used for the shear strain field. Vecchio and Collins [152] compared the accuracy of different shape functions with constant and parabolic shear flows in typical beam sections and obtained fairly similar results. However, their predictions tend to diverge somewhat with the constant shear flow as the flexural moments increases. In this study a constant shear flow will be tested so that the section compatibility matrix that distributes deformations along the section has the form as given in Eq. (4.3). The fiber strains will be calculated using Eq. (4.2).

In fiber level, the material constitutive model will be adapted from MCFT formulations in terms of principal strain-stress conditions. This approach maintains a compatibility between the shear and axial deformations to compute principal stresses using one material constitutive model. In solving this problem, the following assumptions are considered:

1. Longitudinal reinforcing steel is treated as an independent uniaxial material and its influence on vertical shear resistance is neglected.
2. A reasonable simplification is to assume the directions of principal strain and stress axes in concrete fibers coincide [151]:

$$\theta_\varepsilon = \theta_\sigma = \theta \quad (4.9)$$

3. A perfect bond comprises the strain compatibility between vertical reinforcement and concrete.
4. Principal angle θ , can be obtained with an iterative algorithm while main-

taining vertical force equilibrium.

4.2.1 Strain Compatibility

The vertical and longitudinal reinforcement is anchored to the concrete and compatibility requires that any strain condition acting on concrete fibers matches the condition on steel reinforcement fibers:

$$\varepsilon_{xs} = \varepsilon_{xc} = \varepsilon_x \quad (4.10)$$

$$\varepsilon_{ys} = \varepsilon_{yc} = \varepsilon_y \quad (4.11)$$

When the strain components ε_x , ε_y and γ_{xy} , are known and the strain in principal directions ε_1 and ε_2 can be calculated using the Mohr's circle of strain. The typical compatibility equations used in the section deformation model are given as [151]:

$$\varepsilon_2 = \varepsilon_x + \frac{\gamma_{xy}}{2} \tan(\theta) \quad (4.12)$$

$$\varepsilon_1 = \frac{\varepsilon_x - \varepsilon_2}{\tan^2(\theta)} + \varepsilon_x \quad (4.13)$$

$$\varepsilon_y = \varepsilon_1 + \varepsilon_2 - \varepsilon_x \quad (4.14)$$

Once the principal strains are obtained, stress-strain relationships are required to link the principal stresses to strains.

4.2.2 Constitutive Behaviors

Stress-strain relationships are required to link fiber stresses to strains for both concrete and reinforcement. The principal tension $\sigma_1 = \sigma_1(\varepsilon_1)$ and principal compression $\sigma_2 = \sigma_2(\varepsilon_2)$ stress-strain behaviors are adapted from related studies. For the constitutive model of concrete in compression, the model proposed by Popovics [120] for normal strength concrete is adapted to the material class Fig. 4.2.

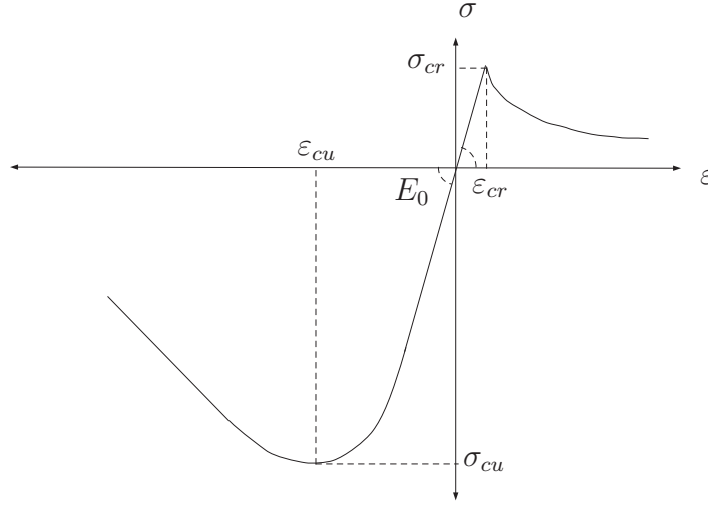


Figure 4.2: Principal strain-stress model

$$\sigma_2 = - \left(\frac{\varepsilon_c}{\varepsilon_{cu}} \right) \sigma_{cu} \frac{n_E}{n_E - 1 + \left(\frac{\varepsilon_c}{\varepsilon_{cu}} \right)^{n_E}} \quad (4.15)$$

where

$$n_E = \frac{E_0}{E_0 - \frac{\sigma_{cu}}{\varepsilon_{cu}}} \quad (4.16)$$

The tension behavior of concrete is taken as linear elastic until critical stress level. For tension softening in concrete, the model by Vecchio and Collins [151]

will be considered. The relationship after cracking has the form,

$$\sigma_1 = \frac{\sigma_{cr}}{1 + \sqrt{500\varepsilon_1}} \quad (4.17)$$

Then, the principal stresses in concrete and the stress in the vertical reinforcing steel are computed while satisfying the vertical equilibrium.

4.2.3 Equilibrium Condition

The computation of shear strain distribution requires complex algorithms and heavy computational effort [152]. Thus, a predefined shear strain field that applies constant shear strain along the section was assumed to implement explicitly in the section deformation calculations. The lateral strain field ε_y is statically evaluated at each fiber separately by imposing the equilibrium between transverse steel and concrete [117]:

$$\sigma_{y_c}^i A_{y_c}^i + \sigma_{y_s}^i A_{y_s}^i = 0 \quad (4.18)$$

where $\sigma_{y_c}^i = \sigma_{y_c}^i(\varepsilon_x^i, \varepsilon_y^i, \gamma_{xy}^i)$ and $\sigma_{y_s}^i = \sigma_{y_s}^i(\varepsilon_y^i)$ at i^{th} fiber. The transverse steel strain-stress relationship is taken as linear-elastic, $\sigma_{y_s}^i = E_s \varepsilon_y^i$. The quantities A_{y_c} and A_{y_s} is concrete and transverse steel areas respectively. In terms of the transverse steel ratio ρ_v , the equilibrium has the form:

$$\sigma_{y_c}^i + \sigma_{y_s}^i \rho_v = 0 \quad (4.19)$$

The transverse steel ratio is the ratio of stirrup area to concrete area along a stirrup spacing, $\rho_v = A_{y_s}/A_{y_c}$.

Lateral stress in concrete can be obtained using the relationships from Mohr's

circle for stress condition. Regarding Eq. (4.9), the concrete stresses are calculated:

$$\tau_{xy_c} = \frac{\sin(2\theta)}{2} (\sigma_1 - \sigma_2) \quad (4.20)$$

$$\sigma_{x_c} = \sigma_2 - \tau_{xy_c} \tan(\theta) \quad (4.21)$$

$$\sigma_{y_c} = \sigma_1 + \tau_{xy_c} \tan(\theta) \quad (4.22)$$

However, neither the principal axis direction, θ , nor the vertical elongation, ε_y , is known to start computations. An iterative search needs to be performed for a strain state in fibers.

4.2.4 Angle Search Algorithm

To start calculating the fiber axial and shear stresses for a strain condition, the lateral strain ε_y or crack angle θ must be known for when lateral force equilibrium is satisfied. Therefore, an iterative angle search procedure is required. The proposed computation procedure of fiber stresses in terms of fiber strains via principal strain-stress constitution is summarized in the flow chart of Fig. 4.3.

The iterative procedure scans the Mohr's stress and strain circles with small angle increments along the interval $[0^\circ, 90^\circ]$ in the direction of shear strain. Using the Mohr's circle of strain equations, principal strains ε_1 and ε_2 are obtained. The constitutive model computes the principal stresses using Eqs. (4.15) and (4.17). Finally, shear, axial and lateral stresses are computed on the Mohr's stress circle and the lateral equilibrium condition is checked. The iterative angle search continues until the lateral equilibrium condition in Eq. (4.19) satisfies and the procedure eventually extracts shear and axial stresses in each fiber.

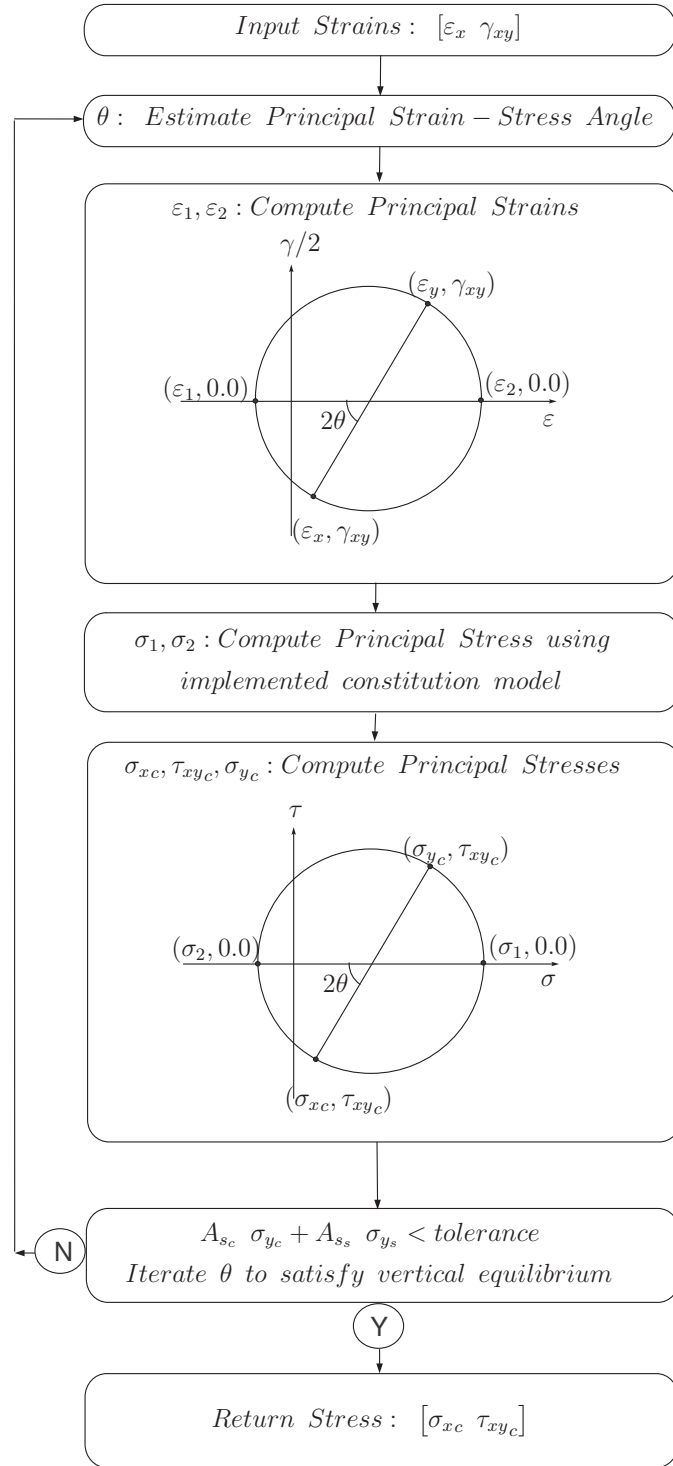


Figure 4.3: Angle search procedure

As a consequence of moving vehicle load, the stress conditions on fibers simulate a hysteretic response. Thus, a cyclic behavior model needs to describe how concrete reloads to and unloads from the monotonic concrete strain-stress curve. To keep the programming of the material model at a basic level for the simplicity of response sensitivity formulations, the plastic offsets are not recorded. As a result, the concrete linearly reloads from and unloads to the point of zero strain and zero stress of the monotonic behavior curve.

$$\sigma_2 = \begin{cases} \sigma_2(\varepsilon_2) & \leftarrow \varepsilon_2 < \varepsilon_{2min} < 0 \\ \frac{\varepsilon_2}{\varepsilon_{2min}} \sigma_{\varepsilon_{2min}} & \leftarrow \varepsilon_{2min} < \varepsilon_2 < 0 \\ 0 & \leftarrow 0 < \varepsilon_2 \end{cases} \quad (4.23)$$

where ε_{2min} is the minimum compressive strain and $\sigma_{\varepsilon_{2min}}$ is the corresponding minimum stress. The function $\sigma_2(\varepsilon_2)$ defines the monotonic compression stress-strain relationships as given in Eq. (4.15). For the principal tension, reload and unload functions have the form:

$$\sigma_1 = \begin{cases} \sigma_1(\varepsilon_1) & \leftarrow \varepsilon_{1max} < \varepsilon_1 \\ \frac{\varepsilon_1}{\varepsilon_{1max}} \sigma_{\varepsilon_{1max}} & \leftarrow 0 < \varepsilon_1 < \varepsilon_{1max} \\ 0 & \leftarrow 0 > \varepsilon_1 \end{cases} \quad (4.24)$$

where ε_{1max} is the maximum compressive strain and $\sigma_{\varepsilon_{1max}}$ is the corresponding stress. The monotonic tensile stress-strain relationship in Eq. (4.17) is plugged in as the function $\sigma_2(\varepsilon_2)$ once the tensile stress exceeds the critical level σ_{cr} .

However, the knowledge of previously attained maximum, $\varepsilon_{max} = [\varepsilon_{x_{max}}, \varepsilon_{y_{max}}, \gamma_{xy_{max}}]$, and minimum, $\varepsilon_{min} = [\varepsilon_{x_{min}}, \varepsilon_{y_{min}}, \gamma_{xy_{min}}]$, concrete strain condition is required to define reloading and unloading slopes. Vecchio [149] recommended a

Mohr's circle approach to approximate the maximum strains corresponding to an arbitrary direction and obtained successful test verifications. The approximated maximum strain envelopes for principal directions are used to compute max-min principal stress at every trial principal direction:

$$\varepsilon_{1_{max}} = \frac{\varepsilon_{x_{max}} - \varepsilon_{y_{max}}}{2} + \frac{\varepsilon_{x_{max}} - \varepsilon_{y_{max}}}{2} \cos(2\theta) - \frac{\gamma_{xy_{max}}}{2} \sin(2\theta) \quad (4.25)$$

$$\varepsilon_{2_{min}} = \frac{\varepsilon_{x_{min}} - \varepsilon_{y_{min}}}{2} + \frac{\varepsilon_{x_{min}} - \varepsilon_{y_{min}}}{2} \cos(2\theta) - \frac{\gamma_{xy_{min}}}{2} \sin(2\theta) \quad (4.26)$$

However, these strain values do not represent a compatible strain condition at one time and the approximated ultimate strain envelope might be recorded at different time steps. On the other hand, recording ultimate strains at every principal angle direction for each fiber is inefficient from the programming aspects.

4.2.5 Tangent Stiffness

For the implementation to OpenSees, the new material class needs to compute the tangent stiffness matrix corresponding to increments in fiber strain and stress. The stiffness matrix should represent the composite behavior of concrete fiber and transverse reinforcement.

The angle search procedure will use ε_x , γ_{xy} and the estimated angle value θ as three independent input data in the stress-strain computations. The vertical strain ε_y and stresses will be computed in terms of independent variable θ . Strain-stress

relationship in concrete and vertical reinforcement are obtained in terms of their distinguished stiffness matrices, \mathbf{T}_c and \mathbf{T}_v :

$$\begin{bmatrix} \Delta\sigma_{xc} \\ \Delta\sigma_{yc} \\ \Delta\tau_{xy_c} \end{bmatrix} = \begin{bmatrix} \frac{\partial\sigma_x}{\partial\varepsilon_x} & \frac{\partial\sigma_x}{\partial\theta} & \frac{\partial\sigma_x}{\partial\gamma_{xy}} \\ \frac{\partial\sigma_y}{\partial\varepsilon_x} & \frac{\partial\sigma_y}{\partial\theta} & \frac{\partial\sigma_y}{\partial\gamma_{xy}} \\ \frac{\partial\tau_{xy}}{\partial\varepsilon_x} & \frac{\partial\tau_{xy}}{\partial\theta} & \frac{\partial\tau_{xy}}{\partial\gamma_{xy}} \end{bmatrix} \begin{bmatrix} \Delta\varepsilon_x \\ \Delta\theta \\ \Delta\gamma_{xy} \end{bmatrix} \quad (4.27)$$

$$\begin{bmatrix} \Delta\sigma_{xv} \\ \Delta\sigma_{yv} \\ \Delta\tau_{xy_v} \end{bmatrix} = \begin{bmatrix} 0 & 0 & 0 \\ \frac{\partial\sigma_{yv}}{\partial\varepsilon_x} & \frac{\partial\sigma_{yv}}{\partial\theta} & \frac{\partial\sigma_{yv}}{\partial\gamma_{xy}} \\ 0 & 0 & 0 \end{bmatrix} \begin{bmatrix} \Delta\varepsilon_x \\ \Delta\theta \\ \Delta\gamma_{xy} \end{bmatrix} \quad (4.28)$$

Total fiber stiffness is the sum of contributions from concrete and reinforcement and has the form:

$$\mathbf{T}_{fiber} = \mathbf{T}_c + \mathbf{T}_v = \begin{bmatrix} T_{11} & T_{12} & T_{13} \\ T_{21} & T_{22} & T_{23} \\ T_{31} & T_{32} & T_{33} \end{bmatrix} \quad (4.29)$$

Recalling the assumption that there is no total stress in transverse direction, the total fiber stiffness matrix is reduced to \mathbf{T}'_{fiber} by a simple algebraic rearrangement [16] that will define the fiber behavior in terms of ε_x and γ_{xy} .

$$\mathbf{T}'_{fiber} = \begin{bmatrix} T_{11} - \frac{T_{12}T_{21}}{T_{22}} & T_{13} - \frac{T_{12}T_{23}}{T_{22}} \\ T_{31} - \frac{T_{32}T_{12}}{T_{22}} & T_{33} - \frac{T_{32}T_{23}}{T_{22}} \end{bmatrix} \quad (4.30)$$

For coding procedure in C++, the new material requires peak compression strength σ_{cu} , strain at peak strength ε_{cu} , initial stiffness E_0 , critical tension stress σ_{cr} , vertical reinforcement modulus of elasticity E_s and stirrup ratio at gauss points ρ_v .

4.2.6 Sensitivity Formulations

The response sensitivity formulations require the derivative of fiber stress to compute Eqs. (4.5) and (4.7). The DDM formulations are established through the strain compatibility, the equilibrium condition and the material constitution of each fiber. In reliability analysis examples, the compressive strength, σ_{cu} , ultimate concrete tensile strength, σ_{cr} , and initial elastic modulus of concrete, E_0 , will be considered for differentiation.

The derivation starts with stress-strain constitution on principal axis directions. For the principal compression Eq. (4.15) is derived with respect to the sensitivity parameter, φ :

$$\begin{aligned} \frac{\partial \sigma_2}{\partial \varphi} = & -\frac{\frac{1}{\varepsilon_{cu}}}{n_E - 1 + \left(\frac{\varepsilon_2}{\varepsilon_{cu}}\right)^{n_E}} \left[\frac{\partial \varepsilon_2}{\partial \varphi} \sigma_{cu} n_E + \varepsilon_2 \frac{\partial \sigma_{cu}}{\partial \varphi} n_E + \varepsilon_2 \sigma_{cu} \frac{\partial n_E}{\partial \varphi} \right] \\ & + \frac{\left(\frac{\varepsilon_2}{\varepsilon_{cu}}\right) \sigma_{cu} n_E}{\left(n_E - 1 + \left(\frac{\varepsilon_2}{\varepsilon_{cu}}\right)^{n_E}\right)^2} \left[\frac{\partial n_E}{\partial \varphi} + \left(\frac{\varepsilon_2}{\varepsilon_{cu}}\right)^{n_E} \left(\frac{\partial n_E}{\partial \varphi} \ln(\varepsilon_2) + n_E \frac{\partial \varepsilon_2}{\partial \varphi} \right) \right] \end{aligned} \quad (4.31)$$

where the derivative of n_E is:

$$\frac{\partial n_E}{\partial \varphi} = \frac{\frac{\partial E_0}{\partial \varphi}}{E_0 - \frac{\sigma_{cu}}{\varepsilon_{cu}}} - \frac{E_0}{\left(E_0 - \frac{\sigma_{cu}}{\varepsilon_{cu}}\right)^2} \left(\frac{\partial E_0}{\partial \varphi} - \frac{\frac{\partial \sigma_{cu}}{\partial \varphi}}{\varepsilon_{cu}} \right) \quad (4.32)$$

For the derivative of principal tension stress, pre- and post-peak formulations are differentiated:

$$\frac{\partial \sigma_1}{\partial \varphi} = \frac{\partial E_0}{\partial \varphi} \varepsilon_1 + E_0 \frac{\partial \varepsilon_1}{\partial \varphi} \quad (4.33)$$

$$\frac{\partial \sigma_1}{\partial \varphi} = \frac{\frac{\partial \sigma_{cr}}{\partial \varphi}}{1 + \sqrt{500\varepsilon_1}} - \frac{\sigma_{cu}}{(1 + \sqrt{500\varepsilon_1})^2} \left(\frac{\sqrt{500\varepsilon_1}}{2} \right) \left(500 \frac{\partial \varepsilon_1}{\partial \varphi} \right) \quad (4.34)$$

For the linear unloading/reloading branch in principal tension ($\varepsilon_1 < \varepsilon_{1max}$) and compression ($\varepsilon_2 > \varepsilon_{2min}$), the stress sensitivity is obtained as:

$$\frac{\partial \sigma_1}{\partial \varphi} = \frac{\partial \sigma_{\varepsilon_{1max}}}{\partial \varphi} \frac{\varepsilon_1}{\varepsilon_{1max}} + \sigma_{\varepsilon_{1max}} \left(\frac{\frac{\partial \varepsilon_1}{\partial \varphi}}{\varepsilon_{1max}} - \varepsilon_1 \frac{\frac{\partial \varepsilon_{1max}}{\partial \varphi}}{\varepsilon_{1max}^2} \right) \quad (4.35)$$

$$\frac{\partial \sigma_2}{\partial \varphi} = \frac{\partial \sigma_{\varepsilon_{2min}}}{\partial \varphi} \frac{\varepsilon_2}{\varepsilon_{2min}} + \sigma_{\varepsilon_{2min}} \left(\frac{\frac{\partial \varepsilon_2}{\partial \varphi}}{\varepsilon_{2min}} - \varepsilon_2 \frac{\frac{\partial \varepsilon_{2min}}{\partial \varphi}}{\varepsilon_{2min}^2} \right) \quad (4.36)$$

There are four sensitivity history variables to track the path-dependent behavior, ε_{1max} , $\sigma_{\varepsilon_{1max}}$, ε_{2min} and $\sigma_{\varepsilon_{2min}}$. The principal tension and compression stresses at the maximum and minimum strain values need to be recorded. The sensitivity of history variable requires the gradients of strain envelope ε_{xmax} , ε_{xmin} , $\gamma_{xy_{max}}$, $\gamma_{xy_{min}}$, ε_{ymax} and ε_{ymin} that are obtained in terms of section derivatives $\partial \mathbf{e} / \partial \varphi$ differentiating Eq. (4.2) along load increment steps where maximum and minimum strains are committed. When principal strains are in unloading/reloading branch, the minimum-maximum strain and stress values do not change, so that the sensitivity history variables are not updated during the fiber is reloading or unloading in principal axis directions.

The derivative of maximum principal tension strain is:

$$\begin{aligned} \frac{\partial \varepsilon_{1max}}{\partial \varphi} = & \frac{1}{2} \left(\frac{\partial \varepsilon_{xmax}}{\partial \varphi} - \frac{\partial \varepsilon_{ymax}}{\partial \varphi} \right) + \frac{\cos(2\theta)}{2} \left(\frac{\partial \varepsilon_{xmax}}{\partial \varphi} - \frac{\partial \varepsilon_{ymax}}{\partial \varphi} \right) \\ & - \sin(2\theta) \frac{\partial \theta}{\partial \varphi} (\varepsilon_{xmax} - \varepsilon_{ymax}) - \frac{\sin(2\theta)}{2} \frac{\partial \gamma_{xy_{max}}}{\partial \varphi} - \cos(2\theta) \gamma_{xy_{max}} \frac{\partial \theta}{\partial \varphi} \end{aligned} \quad (4.37)$$

The derivative of minimum principal compression strain has the form:

$$\begin{aligned} \frac{\partial \varepsilon_{2min}}{\partial \varphi} = & \frac{1}{2} \left(\frac{\partial \varepsilon_{xmin}}{\partial \varphi} - \frac{\partial \varepsilon_{ymin}}{\partial \varphi} \right) + \frac{\cos(2\theta)}{2} \left(\frac{\partial \varepsilon_{xmin}}{\partial \varphi} - \frac{\partial \varepsilon_{ymin}}{\partial \varphi} \right) \\ & - \sin(2\theta) \frac{\partial \theta}{\partial \varphi} (\varepsilon_{xmin} - \varepsilon_{ymin}) - \frac{\sin(2\theta)}{2} \frac{\partial \gamma_{xymin}}{\partial \varphi} - \cos(2\theta) \gamma_{xymin} \frac{\partial \theta}{\partial \varphi} \end{aligned} \quad (4.38)$$

The compressive stress gradient $\partial \sigma_{\varepsilon_{2min}} / \partial \varphi$ is calculated at recorded minimum compressive strain using Eq. (4.31). The tension stress gradient $\partial \sigma_{\varepsilon_{2min}} / \partial \varphi$ is calculated by Eqs. (4.33) and (4.34) whether the corresponding maximum tensile is in linear elastic or softening region.

The concrete stresses given in Eqs. (4.20), (4.21), and (4.22) are derived with respect to the sensitivity parameter:

$$\frac{\partial \tau_{xy_c}}{\partial \varphi} = \frac{\sin(2\theta)}{2} \left(\frac{\partial \sigma_1}{\partial \varphi} - \frac{\partial \sigma_2}{\partial \varphi} \right) + 2\cos(2\theta) \frac{\partial \theta}{\partial \varphi} (\sigma_1 - \sigma_2) \quad (4.39)$$

$$\frac{\partial \sigma_{x_c}}{\partial \varphi} = \frac{\partial \sigma_2}{\partial \varphi} - \frac{\partial \tau_{xy_c}}{\partial \varphi} \tan(\theta) - \tau_{xy_c} \sec^2(\theta) \frac{\partial \theta}{\partial \varphi} \quad (4.40)$$

$$\frac{\partial \sigma_{y_c}}{\partial \varphi} = \frac{\partial \sigma_1}{\partial \varphi} + \frac{\partial \tau_{xy_c}}{\partial \varphi} \tan(\theta) + \tau_{xy_c} \sec^2(\theta) \frac{\partial \theta}{\partial \varphi} \quad (4.41)$$

The strains $[\varepsilon_x, \gamma_{xy}]$ with θ iterated to compute ε_y vertical strain defines the strain state at a fiber. At fixed strain state, the gradients $\partial \varepsilon_x / \partial \varphi|_\varepsilon$, $\partial \gamma_{xy} / \partial \varphi|_\varepsilon$, $\partial \theta / \partial \varphi|_\varepsilon$, $\partial \varepsilon_1 / \partial \varphi|_\varepsilon$ and $\partial \varepsilon_2 / \partial \varphi|_\varepsilon$ are equal to zero so that the conditional derivatives of fiber strains have the form:

$$\left. \frac{\partial \tau_{xy_c}}{\partial \varphi} \right|_\varepsilon = \frac{\sin(2\theta)}{2} \left(\frac{\partial \sigma_1}{\partial \varphi} - \frac{\partial \sigma_2}{\partial \varphi} \right) \quad (4.42)$$

$$\left. \frac{\partial \sigma_{x_c}}{\partial \varphi} \right|_\varepsilon = \frac{\partial \sigma_2}{\partial \varphi} - \frac{\partial \tau_{xy_c}}{\partial \varphi} \tan(\theta) \quad (4.43)$$

$$\left. \frac{\partial \sigma_{yc}}{\partial \varphi} \right|_{\varepsilon} = \frac{\partial \sigma_1}{\partial \varphi} + \frac{\partial \tau_{xyc}}{\partial \varphi} \tan(\theta) \quad (4.44)$$

The stress-strain relations and their sensitivity computations are completed for the biaxial material model. The implementation to OpenSees continues with the fiber section integration class compatible with the new material model.

4.3 T-Beam Section

To consider the contribution of deck to the section stiffness, a new section model should be defined in terms of deck thickness h_f and effective flange width b_{eff} . One other implementation in OpenSees is the template for T-shape beam section as shown in Fig. 4.4. The new model compatible with proposed MCFT material is based on a fiber discretization in both web and flange sides. To consider the confinement of concrete in the section, different concrete materials can be defined separately as cover and core in the web and flange. For the constitution of longitudinal reinforcement, the template will be available with current uniaxial steel materials in OpenSees library. Finally, the shape sensitivities with respect to each parameter defining the T-beam configuration will be formulated to consider geometric uncertainty.

4.3.1 T-Beam Fiber Discretization

T-section is defined by the parameters: overall section depth, d ; web thickness, b_w ; effective width, b_{eff} ; and deck thickness, h_f . The number of web fibers is N_w and N_f is the number of flange fibers. The indices *cover* and *core* defines the number of fibers in cover and core region of the section flange and web. The reference axis

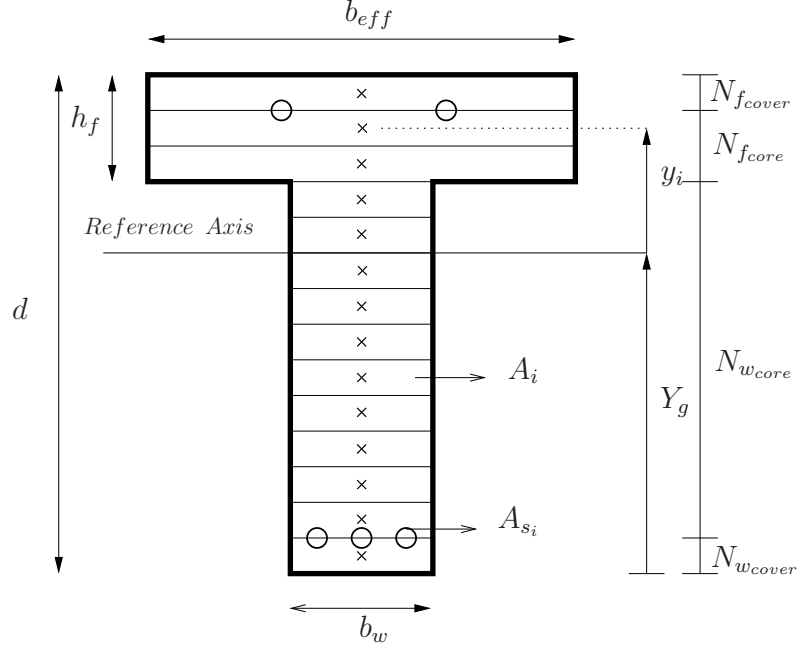


Figure 4.4: T-beam fiber section

from the bottom of the section web is computed:

$$Y_g = \frac{0.5(d - h_f)b_w(d - h_f) + b_{eff}h_f(d - 0.5h_f)}{b_{eff}h_f + (d - h_f)b_w} \quad (4.45)$$

The location of the i^{th} web core fiber is calculated for $i = 1, \dots, N_{w_{core}}$ in terms of web cover, w_{cover} :

$$y_i = -Y_g + w_{cover} + 0.5 \frac{d - h_f - w_{cover}}{N_{w_{core}}} + \frac{d - h_f - w_{cover}}{N_{w_{core}}} i \quad (4.46)$$

The location of a flange core fiber is calculated for $i = 1, \dots, N_{f_{core}}$ in terms of flange cover, f_{cover} :

$$y_i = d - Y_g - h_f + 0.5 \frac{h_f - f_{cover}}{N_{f_{core}}} + \frac{h_f - f_{cover}}{N_{f_{core}}} i \quad (4.47)$$

The location of a web cover fiber is calculated for $i = 1, \dots, N_{w_{cover}}$:

$$y_i = -Y_g + 0.5 \frac{w_{cover}}{N_{w_{cover}}} + \frac{w_{cover}}{N_{w_{cover}}} i \quad (4.48)$$

Finally, the location of a flange cover fiber is calculated for $i = 1, \dots, N_{f_{cover}}$:

$$y_i = d - Y_g - f_{cover} + 0.5 \frac{f_{cover}}{N_{f_{cover}}} + \frac{f_{cover}}{N_{f_{cover}}} i \quad (4.49)$$

Once the concrete fibers are located, reinforcing steel fibers $i = 1, \dots, N_{stop}$, are located at $y_i = d - Y_g - f_{cover}$ on top of the section. For the bottom steel fibers $i = 1, \dots, N_{s_{bottom}}$, the location is computed as $y_i = w_{cover} - Y_g$.

From the section dimensions and the number of fibers at each region, the area of web core fibers are:

$$A_{w_{core}} = b_w \frac{d - h_f - w_{cover}}{N_{w_{core}}} \quad (4.50)$$

The size of each flange core fibers is calculated as:

$$A_{f_{core}} = b_{eff} \frac{h_f - f_{cover}}{N_{f_{core}}} \quad (4.51)$$

At the web cover region, a concrete fiber has the area:

$$A_{w_{cover}} = \frac{b_w - w_{cover}}{N_{w_{cover}}} \quad (4.52)$$

Finally, the area of each concrete fiber at the flange cover region is:

$$A_{f_{cover}} = \frac{b_{eff} - f_{cover}}{N_{f_{cover}}} \quad (4.53)$$

while the area of top and bottom steel fiber is directly assigned as A_{stop} and $A_{sbottom}$, respectively.

4.3.2 T-Beam Section Shape Sensitivity Equations

The shape sensitivity of T-beam formulations is required to compute section force gradients as indicated in Eqs. (4.5) and (4.7). The gradients of fiber locations $\partial y_i / \partial \varphi$ and areas $\partial A_i / \partial \varphi$ are calculated at the i^{th} fiber by direct differentiation of formulations from Eq. (4.45) to Eq. (4.53)

Once the derivative of the reference axis location, $\partial Y_g / \partial \varphi$ is obtained, the computation of shape sensitivity is straightforward for deterministic values of N_w and N_f . The sensitivity of i^{th} fiber of web core region for $i = 1, \dots, N_{w_{core}}$:

$$\frac{\partial y_i}{\partial \varphi} = -\frac{\partial Y_g}{\partial \varphi} + \frac{\partial w_{cover}}{\partial \varphi} + \frac{0.5}{N_{w_{core}}} \left(\frac{\partial d}{\partial \varphi} - \frac{\partial h_f}{\partial \varphi} - \frac{\partial w_{cover}}{\partial \varphi} \right) + \frac{i}{N_{w_{core}}} \left(\frac{\partial d}{\partial \varphi} - \frac{\partial h_f}{\partial \varphi} - \frac{\partial w_{cover}}{\partial \varphi} \right) \quad (4.54)$$

For the sensitivity of flange core fibers, the gradient of centroid, $i = 1, \dots, N_{f_{core}}$:

$$\frac{\partial y_i}{\partial \varphi} = \frac{\partial d}{\partial \varphi} - \frac{\partial Y_g}{\partial \varphi} - \frac{\partial h_f}{\partial \varphi} + \frac{0.5}{N_{f_{core}}} \left(\frac{\partial h_f}{\partial \varphi} - \frac{\partial f_{cover}}{\partial \varphi} \right) + \frac{i}{N_{f_{cover}}} \left(\frac{\partial h_f}{\partial \varphi} - \frac{\partial f_{cover}}{\partial \varphi} \right) \quad (4.55)$$

The sensitivity of web cover fibers, $i = 1, \dots, N_{w_{cover}}$, is:

$$\frac{\partial y_i}{\partial \varphi} = -\frac{\partial Y_g}{\partial \varphi} + \frac{0.5}{N_{w_{cover}}} \frac{\partial w_{cover}}{\partial \varphi} + \frac{i}{N_{w_{cover}}} \frac{\partial w_{cover}}{\partial \varphi} \quad (4.56)$$

Finally, for $i = 1, \dots, N_{f_{cover}}$ flange cover fibers, the location gradient is calculated as:

$$\frac{\partial y_i}{\partial \varphi} = \frac{\partial d}{\partial \varphi} - \frac{\partial Y_g}{\partial \varphi} - \frac{\partial f_{cover}}{\partial \varphi} + \frac{0.5}{N_{f_{cover}}} \frac{\partial f_{cover}}{\partial \varphi} + \frac{i}{N_{f_{cover}}} \frac{\partial f_{cover}}{\partial \varphi} \quad (4.57)$$

The sensitivity of size of a web core fiber is:

$$\frac{\partial A_{w_{core}}}{\partial \varphi} = \frac{1}{N_{w_{core}}} \frac{\partial b_w}{\partial \varphi} \left(\frac{\partial d}{\partial \varphi} - \frac{\partial h_f}{\partial \varphi} - \frac{\partial w_{cover}}{\partial \varphi} \right) \quad (4.58)$$

For each flange core fiber, the gradient of the size is calculated as:

$$\frac{\partial A_{f_{core}}}{\partial \varphi} = \frac{1}{N_{f_{core}}} \frac{\partial b_{eff}}{\partial \varphi} \left(\frac{\partial h_f}{\partial \varphi} - \frac{\partial f_{cover}}{\partial \varphi} \right) \quad (4.59)$$

At the web cover region, the gradient of fiber area is:

$$\frac{\partial A_{w_{cover}}}{\partial \varphi} = \frac{1}{N_{w_{cover}}} \left(\frac{\partial b_w}{\partial \varphi} - \frac{\partial w_{cover}}{\partial \varphi} \right) \quad (4.60)$$

Finally, the sensitivity of area for each concrete fiber at the flange cover region is:

$$\frac{\partial A_{f_{cover}}}{\partial \varphi} = \frac{1}{N_{f_{cover}}} \left(\frac{\partial b_{eff}}{\partial \varphi} - \frac{\partial f_{cover}}{\partial \varphi} \right) \quad (4.61)$$

The each derivative, $\partial d / \partial \varphi$, $\partial b_w / \partial \varphi$, $\partial h_f / \partial \varphi$, $\partial b_{eff} / \partial \varphi$, $\partial w_{cover} / \partial \varphi$, $\partial f_{cover} / \partial \varphi$, $\partial A_s^- / \partial \varphi$ and $\partial A_s^+ / \partial \varphi$ is equal to either one or zero depending on the parameter φ represents in the section model. The formulations are derived and implemented in OpenSees for the parameters listed in Table 4.1.

4.4 Software Design for The Methodology Tools

OpenSees as an object-oriented software frameworks provides the user an open source code to implement new objects in the program. Objects are structures that encapsulate data algorithms and perform operations requested by the user. An object do not exist unless an instance of the class has been created where internal

Table 4.1: Shape Sensitivity Parameters for T-Beam Section

Geometry:	<i>T-Beam</i>
Section depth	d
Section width	b_w
Effective width	b_{eff}
Deck thickness	h_f
Neg. r/f steel area	A_s^-
Pos. r/f steel area	A_s^+

data and procedures are contained. As an object-oriented programming technique, abstraction provides a common interface to subclasses where such abstract classes give the partial implementation and leave subclasses the rest of the procedure to complete. In this section, the implementation of proposed material model and section shape is explained.

Once the methodology tools are implemented in the software framework, the user needs to define the finite element models and analysis procedures. Tcl scripting language provides an interface with its control structures, programmable operations and procedures. The user is able to customize applications assembling the software blocks. Tcl scripts program OpenSees with provided finite element analysis setup such as nodes, boundary conditions, finite elements, and moving axle loads that represent truck loading along the bridge girders in pseudo-time steps. The input arrays of axle weights and spaces will define the user-specified multi-axle permit truck whose motion will be monitored at time steps.

4.4.1 Implementation of Fiber Section

The force-based element formulation is based on the interpolation of forces at sections along the element. The internal section forces, \mathbf{s} , are defined in terms of corresponding section deformations, \mathbf{e} . In general architecture of OpenSees, computation of section forces and stress resultant are controlled by the abstract class called *ForceDeformation* providing an interface to conduct the operations in subclasses. The computation of section stress resultant and committing the stress state to save the history variables are performed through subclasses of *ForceDeformation*.

A UML diagram [18] of the subclass implementations to OpenSees is shown in Fig. 4.5. The new subclass, *McftFiberSection*, is implemented to obtain stress resultants by evaluating the numerical integration at each fiber level over the section as given in Eq. (4.3). To obtain stress resultant from each fiber, the constitutive relationships need to be implemented within a subclass. In OpenSees, the current multi-axial material models are implemented under the subclass name *nDMaterial*. The proposed biaxial constitutive model is encapsulated in a subclass, *ConcreteMcftNonlinear*, assigned to each concrete fiber to carry out the shear-flexural operations. For the longitudinal reinforcing steel material, the constitution formulations are evaluated within the subclass *UniaxialMaterial* assigned on each steel fiber.

The fiber section subclass contains the compatibility matrix, \mathbf{a}_s , carrying the characteristics of axial, flexural and shear deformation distributions in the proposed section model as given in Eq. (4.3). However, the integration of fiber stress requires the locations and the area of fibers in the proposed T-shape girder section. As shown in Fig. 4.6, the new section integration subclass, *RCTbeamSectionIntegration* is implemented to supply the required geometrical data, each fiber location, y_i , and

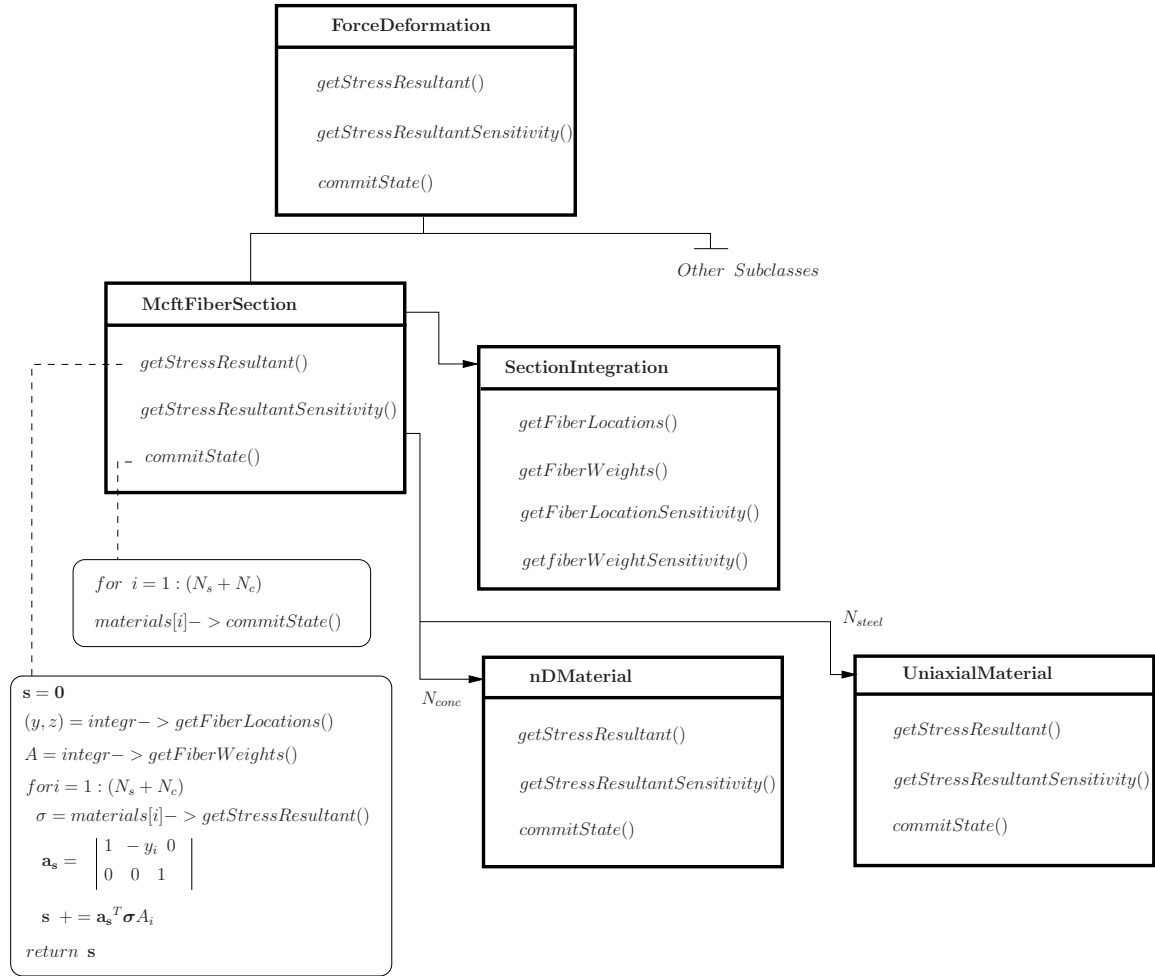


Figure 4.5: Design strategy for MCFT fiber section class.

fiber area, A_i in terms of the parameters, d , b_w , b_{eff} , h_f and number of fibers in core-cover regions of flange and the web of the section.

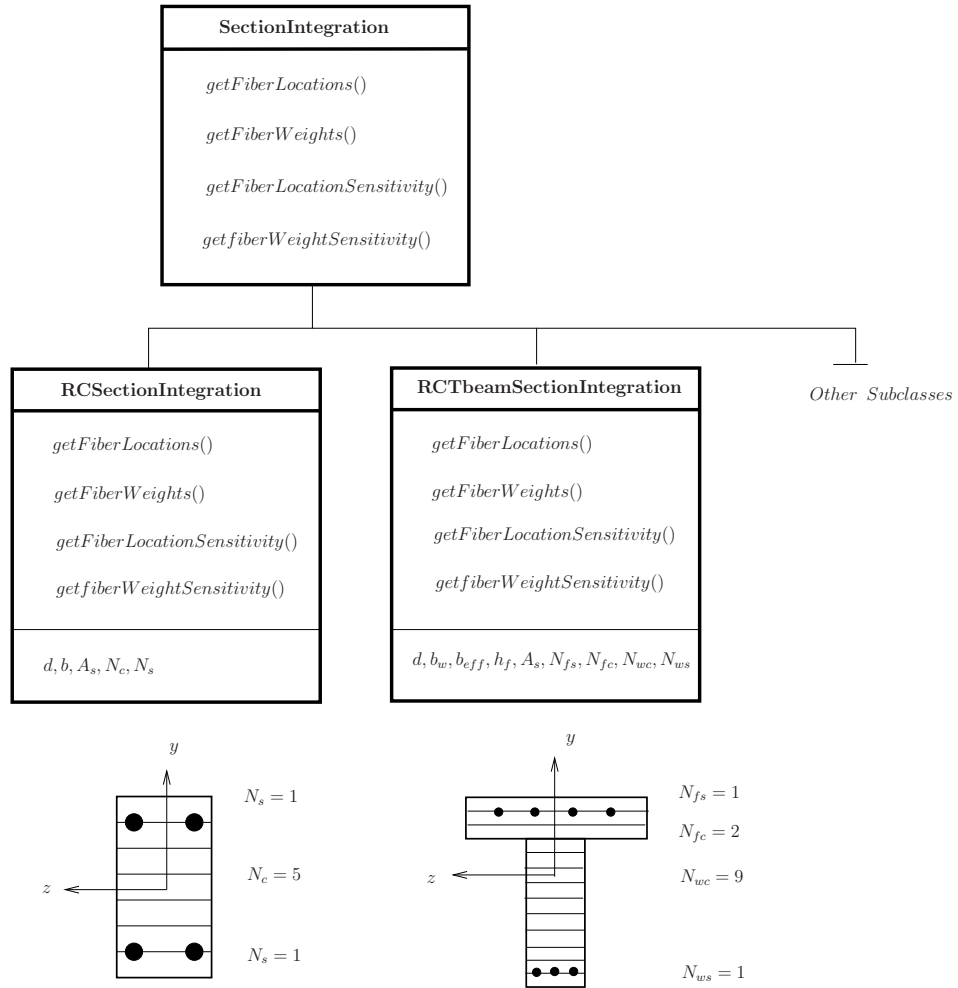


Figure 4.6: Design strategy for section integration class.

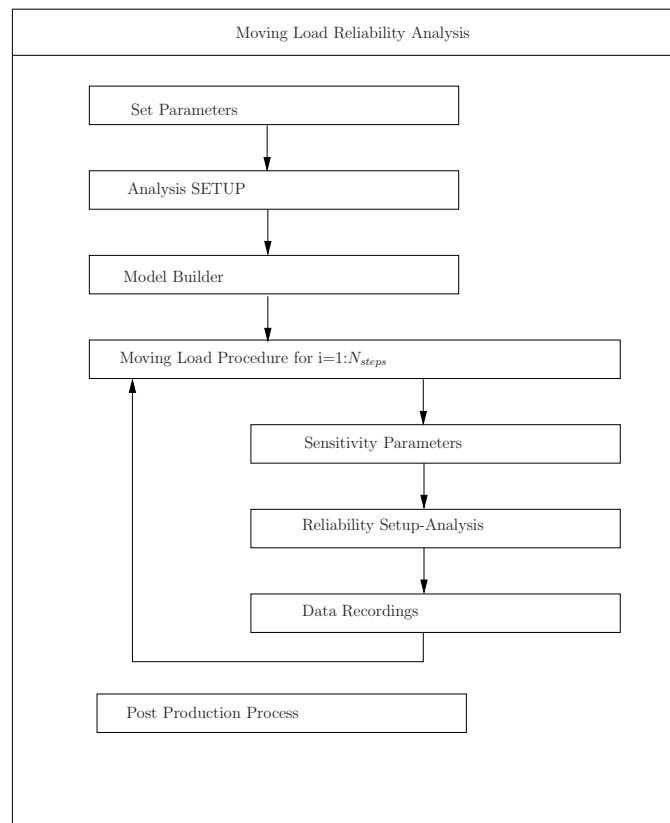


Figure 4.7: Tcl procedure for moving load reliability analysis.

4.4.2 Analysis Setup

The generic script format for reliability analysis of bridge girders is programmed in Tcl using the strategy conducting finite element and reliability analysis modules as shown in Fig. 4.7. The first script carries the data input covering material geometry and loading parameters. The generic bridge model is coded by user defined variables for the number of the spans and corresponding span lengths. The truck loads, axle spaces, concrete and steel material parameters are contained in *SetParameter* script given in Fig. 4.8. Sections are defined using simple data array and the content is indexed with the number corresponding to the order in the array.

The Tcl script *AnalysisSETUP* contains user-defined analysis options that customize moving load reliability procedure as shown in Fig. 4.9. The entry, N_{steps} , is the total number of moving load simulation steps and defines the increment in load along the bridge. The user specifies the target sections in the array, *CrSections* so that the limit state functions are built only at given sections. The variable, *MCFTLines*, is the number of performance functions to be used in reliability analysis.

The capacity will be calculated for critical sections where the performance functions are imposed to run reliability analysis. For user-defined critical sections, moment-shear reliability indices will be calculated at every pseudo-time step using Tcl procedures defined in *AnalysisSETUP*. The script provides capacity calculations for two user defined limit state approaches, LC and MB, as shown in Fig. 4.10.

Using MB procedure, the limit state functions will be defined as five line equations in terms of nominal moment and shear capacity. The Tcl script is made

```

# Span definitions
set Nspan 3
set Lspan { $La $Lb $Lc }
set nIP 3 ;#number of integration points
:
:
# Material Properties
#concrete
set fcu [expr -4000*$psi]
set ecu -0.003
:
:
#steel
set fy [expr 60*$ksi]
set Es [expr 200000*$MPa]
:
:
# Axle Truck Loads and Axle Spaces
set Naxle 8
set s_1 [expr 4300*$mm]
set s_2 [expr 4300*$mm]
:
:
set P_1 [expr -8*$kip]
set P_2 [expr -32*$kip]
set P_3 [expr -32*$kip]
:
:
#Section Properties
#section_ij { $d $bw $Ss $Ast $Asb $Av $beff $hf }
set Section_11 {48 13.0 12.0 7.15 0.40 0.40 13.0 6.0}
set Section_12 {48 13.0 19.0 9.36 0.40 0.40 13.0 6.0}
set Section_13 {48 13.0 19.0 12.48 0.40 0.40 13.0 6.0}
:
:
#Label variables
for {set ie 1} {$ie <= $Nele} {incr ie} {
    for {set inp 1} {$inp <= $nIP} {incr inp} {
        set "d$ie$inp" [expr [lindex [expr $\Section_$ie$inp] 1]*$in]
        set "bw$ie$inp" [expr [lindex [expr $\Section_$ie$inp] 2]*$in]
        :
    }
}

```

Figure 4.8: Parameter entries in reliability analysis scripts

```

# Number of Moving Load Steps
set Nsteps 50

#Critical Sections to investigate
set CrSections {16 17 21 .. ..}

# Numberof lines making MCFT curve
set MCFTLines 5

```

Figure 4.9: Custom setup parameters

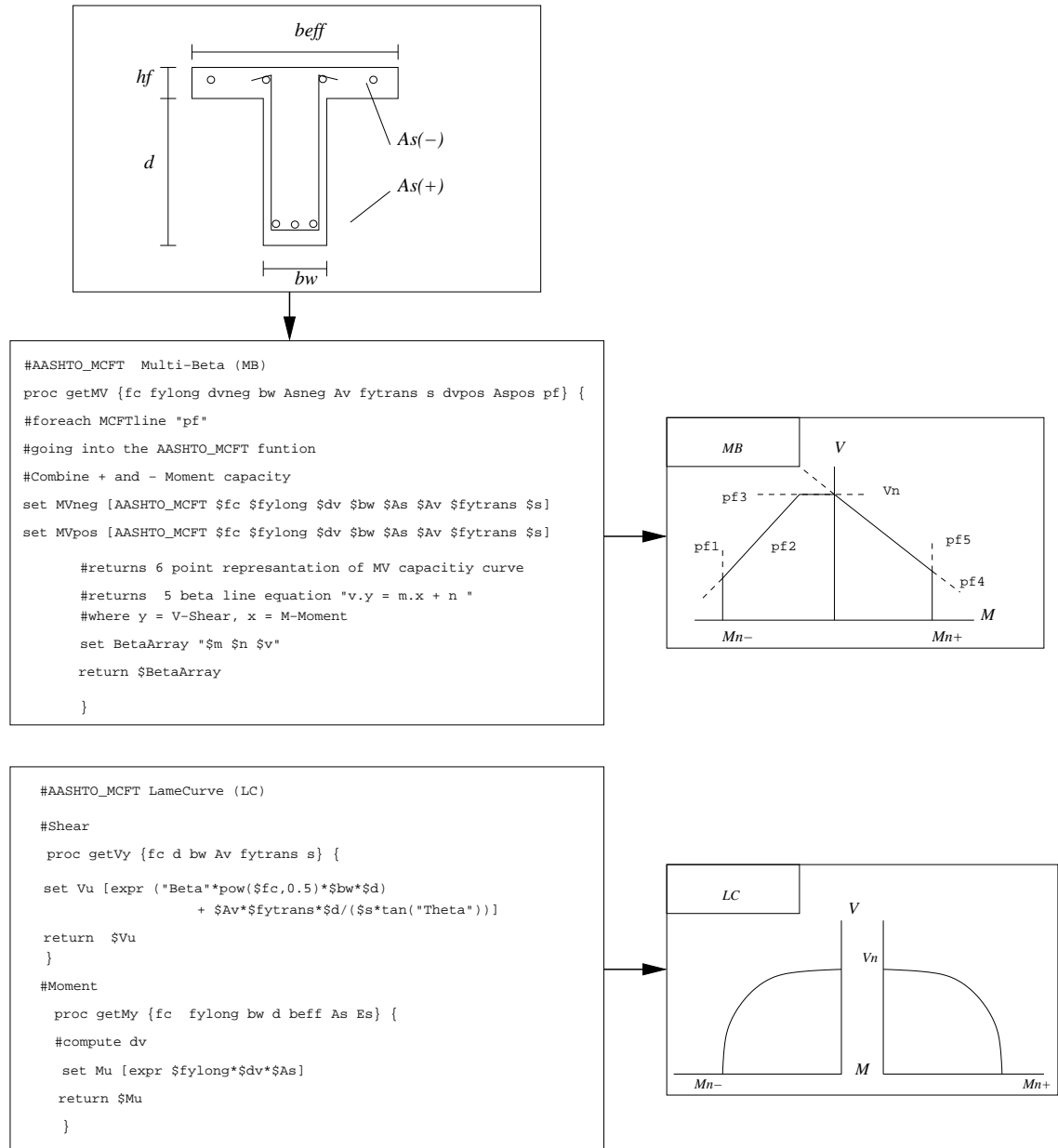


Figure 4.10: Tcl capacity procedures

up of two nested functions. The procedure *getMV* calculates the coefficients of moment and shear demand in each line equation, once the nominal capacity curve calculated by the embedded OpenSees function *AASHTO_MCFT*.

The Tcl and C++ codes for these procedures are given in Appendices A and B. The calculation of LC nominal shear and moment capacity is coded in *getVy* and *getMy* procedures, respectively. The nominal capacities, M_n and V_n , that describe the shape of the Lamé curve are given by peak values from MCFT analysis using Eq. (3.18).

4.4.3 Model Builder

The mesh generation of nodes and force-based beam elements for the model building and moving load analysis is described by Tcl interpreter commands in OpenSees as shown in Fig. 4.11. Tcl code locates a node at each coordinate corresponding to the end point of each span. The interpreter command line *Element* assigns one force-based element for each span. In addition, the command line contains the information about the integration method and the section properties. Eventually, the customization of moving load analysis can easily be coded while investigating bridges with various number and length of spans.

The moving load analysis is based on the repetition of finite element analysis while the position and the combination of loads are changing from one pseudo-time step to another one. The truck loads are represented by the element point loads and the vehicle path is defined as *TrackLength* equal to the sum of twice of the truck length and the total span length so that the analysis will be performed with the step of first axle load until the last axle weight steps off the last span. As the

vehicle moves along the bridge, Tcl code locates the span and the relative distance of the axle weight from the element end and assign a load pattern for each axle.

4.4.4 Reliability Analysis Setup

In FORM analysis of girders in the methodology, random variables on selected parameters need to be assigned to define uncertainties in both demand and resistance side of the limit state. The interaction between finite element modules and reliability addresses the random variable definition of the finite element parameters considered uncertain in the analysis. The Tcl script *RelRV* interprets the command line *randomVariable* as a definition of a uncertainty with a specified probabilistic distribution. The command *parameter* holds the identity of the uncertain parameter so that the limit state function gradients will be calculated in terms of each parameter identified. The Tcl syntax for the random variable and the performance function is shown in Fig. 4.12. To specify the limit state function the required shear and moment coefficients are called in the function using the capacity procedures given in *AnalysisSETUP*. The interpreter command *performanceFunction* indexes the closed form of five limit state equation in a simple loop for each *MCFTline*.

4.5 Material Modeling Verifications

To verify the proposed biaxial material model represents the behavior of shear critical concrete components correctly, a set of pushover analysis has been carried out on several beam specimens having flexural, shear and combined failure modes. First two numerical analyses of hypothetical beam examples are performed to

```

# Node Coordinate Array
set Ltotal {0.0}
set sum 0.0
for {set i 0} {$i < $Span} {incr i} {
  set sum [expr $sum + [lindex $Lspan $i]]
  lappend Ltotal $sum
}
# Assign node coordinates by array
node 1 0.0 0.0

for {set i 1} {$i <= $Span} {incr i} {
  node [expr $i+1] [lindex $Ltotal $i] 0.0
  element forceBeamColumn $i $i [expr $i+1] 1 $integration $sections
}

#Step size - dx
set dx [expr $TrackLength / ($Nsteps)]

# Moving Loads
for {set q 0} {$q <= $Nsteps} {incr q} {
  set x [expr $q*$dx]

# Locate axles
  for {set jj 1} {$jj <= $Naxle} {incr jj} {
    pattern Plain $jj Constant {
      set Load [lindex $axleLoad [expr $jj-1]]
      set Loc [expr $x - [lindex $axleLoc [expr $jj-1]]]

# Check the location and assign the load
      for {set k 1} {$k <= $Span} {incr k} {
        set k1 [lindex $Ltotal [expr $k-1]]
        set k2 [lindex $Ltotal $k]
        if { $Loc > $k1 && $Loc < $k2 } {
          #Relative Distance of Load on Element
          set Reltvdist [expr ($Loc - $k1)/($k2 - $k1)]
          eleLoad -ele $k -type -beamPoint [expr 1*$Load] $Reltvdist
        } else {
          continue
        }
      }
    }
  }
}

```

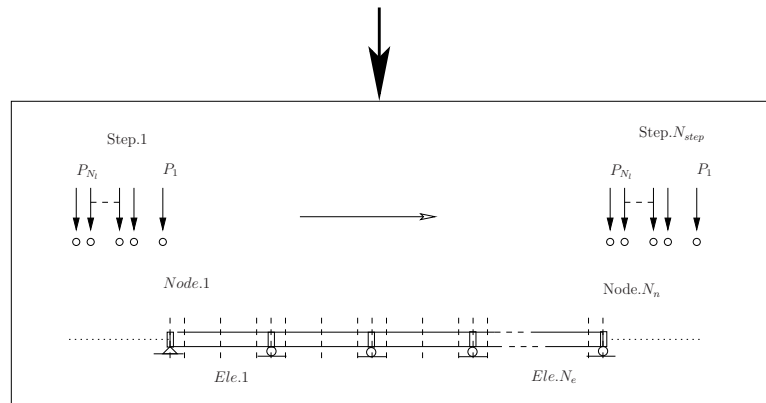


Figure 4.11: Tcl codes for model builder and moving load simulation


```

parameter $i -element $e -section $s -section $parameter
randomVariable $i lognormal $mean $variance
randomVariablePositioner $i -rvNum $i -parameter $parameter

for {set p 1} {$p <= $MCFTLines} {incr p} {
    set cfm "\[lindex \[getMV rvfc $rvfyldong $rvd $rvb $rvAst $rvAv $rvfytrans $rvSs $rvAs $rvEs $rvb) $p] 0 ] "
    set cfn "\[lindex \[getMV rvfc $rvfyldong $rvd $rvb $rvAst $rvAv $rvfytrans $rvSs $rvAs $rvEs $rvb) $p] 0 ] "
    set cfv "\[lindex \[getMV rvfc $rvfyldong $rvd $rvb $rvAst $rvAv $rvfytrans $rvSs $rvAs $rvEs $rvb) $p] 0 ] "
    performanceFunction $p "($cfv) + ($cfm)*(df*IM*[expr $moment]) + ($cfv)*(abs(df*IM*[expr $shear]))"
}

```

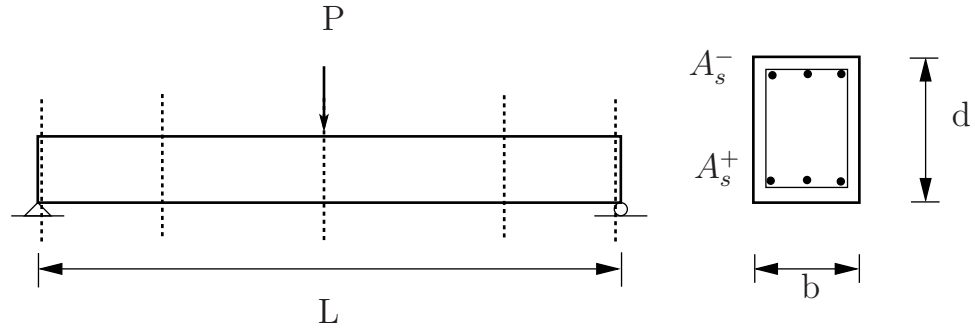
Figure 4.12: Tcl code to assign random variables and performance functions

compare the new model with the uniaxial material models of current OpenSees material library. Then, simulations on real test specimens will follow in this section.

4.5.1 Simply-Supported Beams with Flexure and Shear Failure Modes

Two simply-supported beams have been analyzed to indicate the accuracy of biaxial material model over uniaxial concrete models in OpenSees Fig. 4.13. The analysis results are checked against the solution by non-linear finite element program, VecTor2 [153]. The framework is a non-commercial package for the analysis of two-dimensional reinforced concrete membrane. The theoretical solution method of the program is based on the MCFT and the Disturbed Stress Field Model (DSFM) [150].

The longitudinal reinforcement is modeled by *Steel02* (Fig. D.1) uniaxial material class in OpenSees. For uniaxial representation of concrete fibers *Concrete02* [70] material model (Fig. C.1) with tensile strength and linear tension softening is used in analysis where the shear strains are uncoupled. One force based element



Beam No.	1	2
Failure	Flexure	Shear
L	5000mm	3660mm
d	500mm	550mm
b	200mm	305mm
A_s^-	1500mm ²	200mm ²
A_s^+	3500mm ²	2400mm ²
f_c'	35.0MPa	22.6MPa
ε_c'	-0.002	-0.002
f_{c_r}	2.0MPa	1.7MPa
E_{cinit}	30.6GPa	23.7GPa
E_{sv}	200GPa	200GPa
ρ_v	0.005	0.001
f_y	413MPa	436MPa
E_s	200GPa	200GPa

Figure 4.13: Simply-supported beams: Material and geometry configurations.

is not adequate to record critical vertical displacements so that, two force-based elements are employed in OpenSees analysis where nodal displacement is captured in the mid-span. On each element, integration point weights and locations coincide with integration properties of 5 point Gauss-Lobatto quadrature on one force-based element of entire span. Accordingly, a force-displacement behavior of one force-based element is demonstrated while the critical bending moment at point load location is represented with the weight of a higher order integration method in numerical evaluation of nodal displacement.

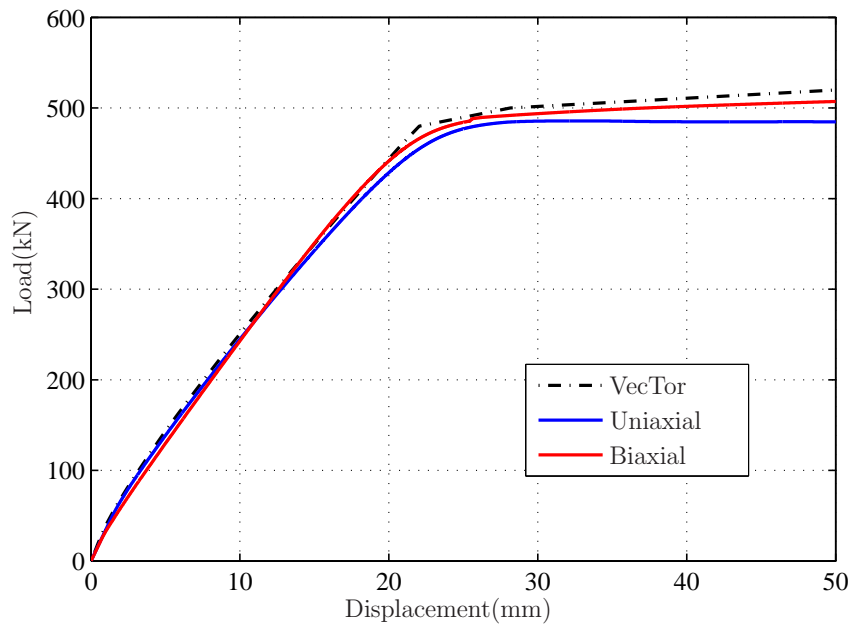


Figure 4.14: Load-displacement behavior of Beam No.1 with flexural failure mode

The beam no.1 has the strength level at $P = 500.0(kN)$ and the failure mode is flexural dominant. The longitudinal reinforcement yields until failure before critical shear deformations occur on the element. The simulations with uniaxial

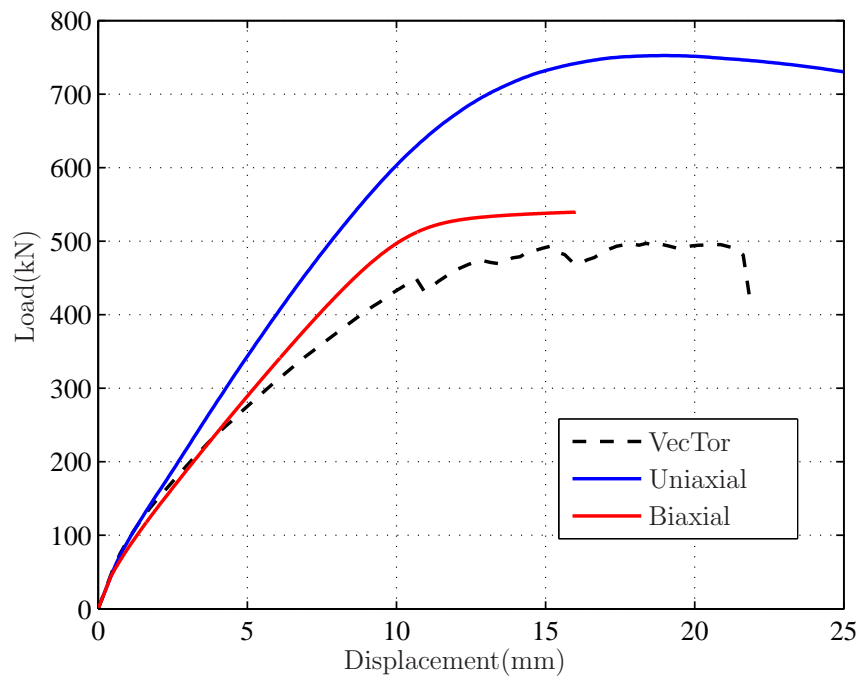


Figure 4.15: Load-displacement behavior of Beam No.2 with shear failure mode

Concrete02 and biaxial model provide flexural representations consistent with each other. The strength and displacement results with biaxial material coincides with the MCFT based VecToR solution.

Meanwhile, a slight difference appears in the analysis of the beam no. 2 when uniaxial and biaxial materials are compared. The VecToR solution indicates a shear crack initiation causes shear dominant failure in shell elements at lower moment-shear ratios. Similarly, biaxial material model subjected to significant shear strain causes a strength reduction. While uniaxial material represents the flexural failure mode of the beam, biaxial material provides a path of strength envelope of a shear dominant behavior in the presence of shear strains. The difference between simulation with uniaxial and biaxial material model is significant, $200(kN)$.

4.5.2 Cantilever Test Specimens with Axial Loading

Three test specimens have been analyzed to demonstrate the accuracy of the proposed biaxial material model in simulating the failure mode of shear critical column elements subjected to axial loading. The setup of specimens is shown in Fig. 4.16 and the related reinforcement configurations are tabulated in Table 4.2. In addition, the stress-strain behavior of concrete fibers is also modeled by a uniaxial *Concrete02* material with a parabolic ascending branch and linear descending branch in compression. For the steel reinforcement, the modulus of elasticity is $E=200000$ MPa, hardening ratio is $\alpha=0.01$ in all specimens and yield stress is taken as listed for each test. A compressive axial load, $P=\nu f'_c A_g$, is applied to each specimen.

The global response is given for each column in Fig. 4.17 using one force-based

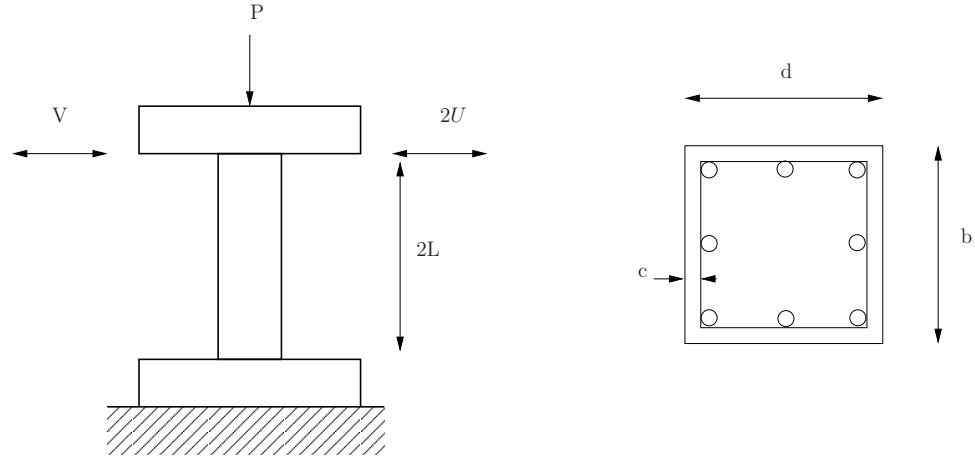


Figure 4.16: Double-cantilever test setup and reinforcement details

Table 4.2: Material and Geometry Properties of Test Specimens

Specimens	1	2	3
Reference	[86]	[111]	[132]
Test No.	3CLH18	4D13RS	2
L	1473.2mm	400.0mm	1473.2mm
d	457.2mm	200.0mm	457.2mm
b	457.2mm	200.0mm	457.2mm
A_s	794.2mm ²	132.7mm ²	645.0mm ²
f'_c	26.9MPa	29.9MPa	21.1MPa
ρ_v	0.001	0.006	0.002
f_y	331MPa	370MPa	434MPa
P-LoadRatio (ν)	0.089	0.153	0.605

element with a high-order Gauss-Lobatto quadrature with seven points providing a sufficient detail of the response. As seen in the figures, uniaxial material that couples only the axial and flexural strain can not detect the global shear strength and represent only the flexural response envelope of test specimens. On the other hand, the proposed material model provides more accurate results. The results show that new biaxial material is able to capture critical shear loading and the accuracy of coupled shear-flexural stiffness of the element on global load-displacement is unquestionable when compared to the uniaxial material.

4.5.3 Simply-Supported T-Beam Girder Specimen

The reinforced concrete T-section girder, the specimen 2T12 in the tests of Higgins et al. [61] is analyzed in this example. Dimensions of the specimen and the reinforcement configuration are given in Fig. 4.18 and Fig. 4.19, respectively. In addition, the crack propagation at the end of the test is also given in the same figure. As in the previous examples, the same constitutive material for the steel are used in this example taking the elastic modulus is $E = 200000MPa$ and the yield stress is $f_y = 413MPa$. In this case, the concrete compressive strength is $f_c' = 30.06MPa$ and the strain at ultimate stress $e_c' = 0.0038$.

The global response of the beam is calculated using two five-point Gauss-Lobatto quadrature and a nine-point low-order integration, $x = \{0.1, 0.2, 0.3, 0.4, 0.5, 0.6, 0.7, 0.8, 0.9\}$, with mid-distance integration weights and the simulated behavior is shown in Fig. 4.20. The proposed biaxial model extracts information on principal stress-strain directions and rotating crack as shown in Fig. 4.21. However, since the entire beam is represented by only one force-based element,

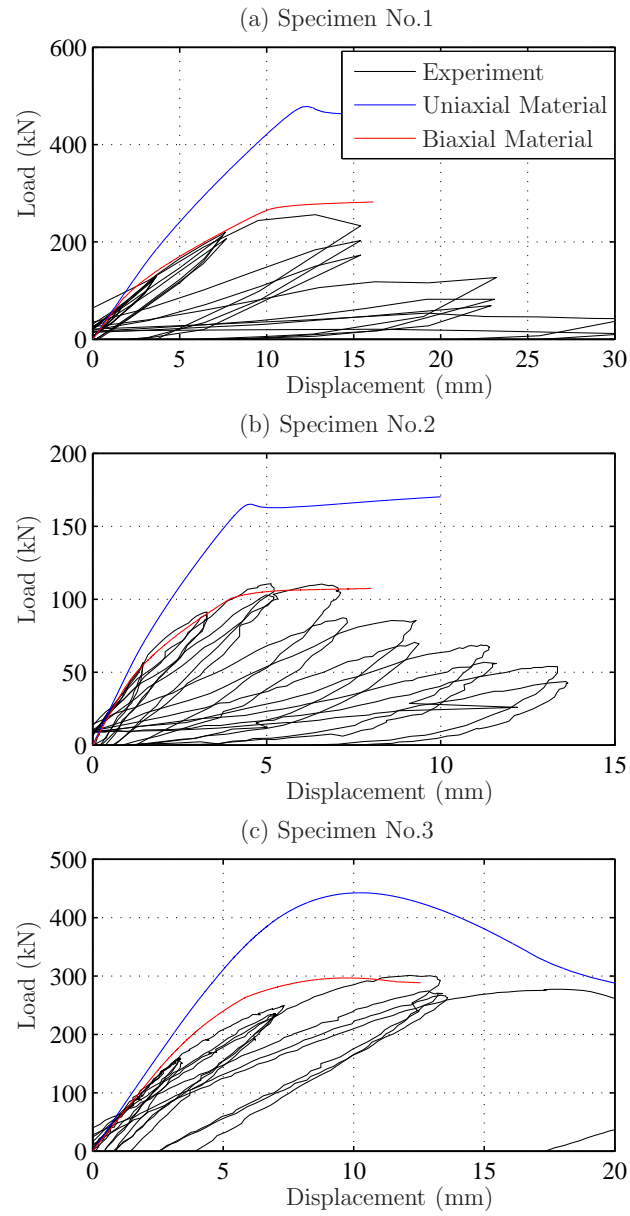


Figure 4.17: Load-displacement behavior of test specimens

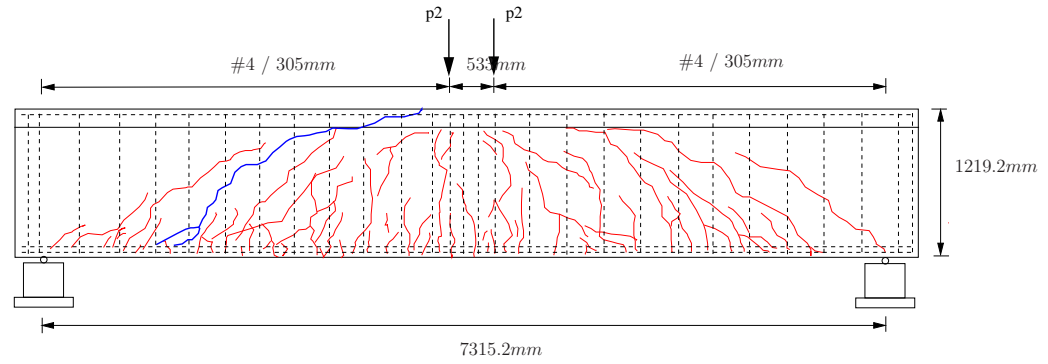


Figure 4.18: T-beam specimen setup and crack propagation map

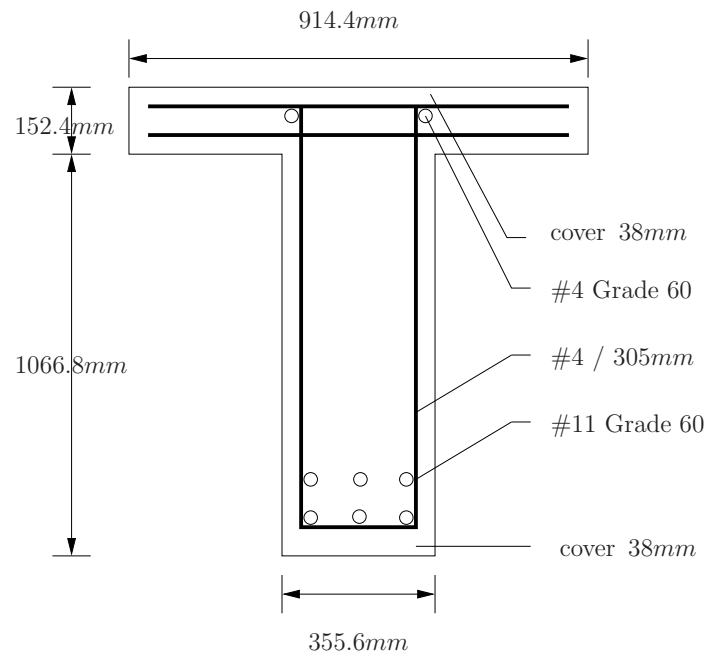


Figure 4.19: T-beam specimen section details

the mid-span displacement is not available, the global response is derived using a linear approximation calculating the displacement by the support rotation.

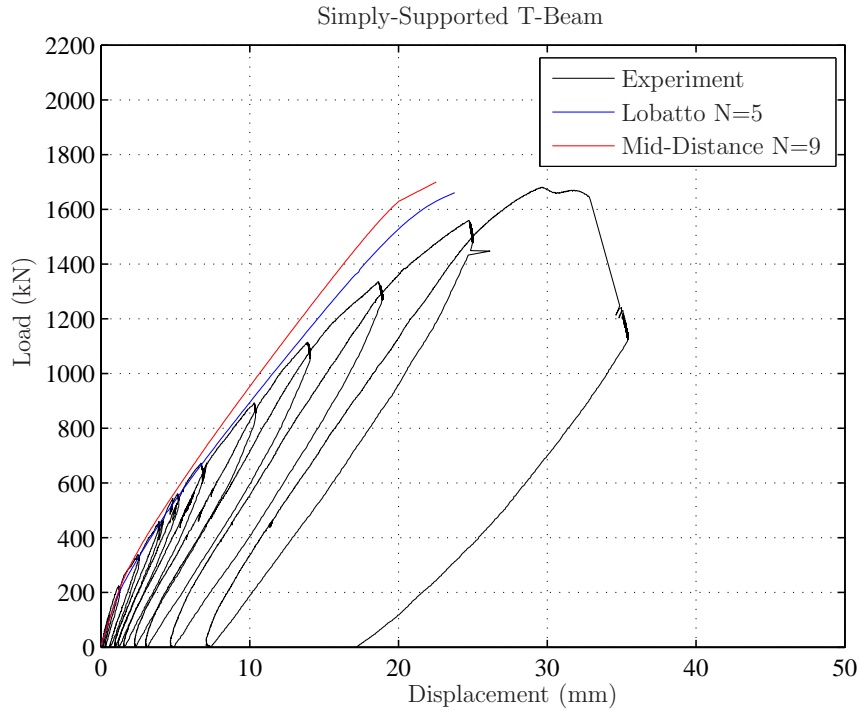


Figure 4.20: Load-displacement behavior of T-beam girder

The simulated global load-displacement response using biaxial material reaches an identical strength level. The recorded displacements are improved when high-order integration quadrature is used. On the other hand, at the lower load, $P = 267kN$ where the initial flexural cracks occurs, the simulated behavior is exact when compared to the test results. In Fig. 4.21, where the cracked fibers are marked in red, the flexure cracks occur at $\theta = 84^\circ \sim 89^\circ$. From support to mid-span, the crack angles decreases to $\theta = 45^\circ \sim 80^\circ$ as the influence of shear deformations starts to overcome axial strains and flexural cracks form into diagonal

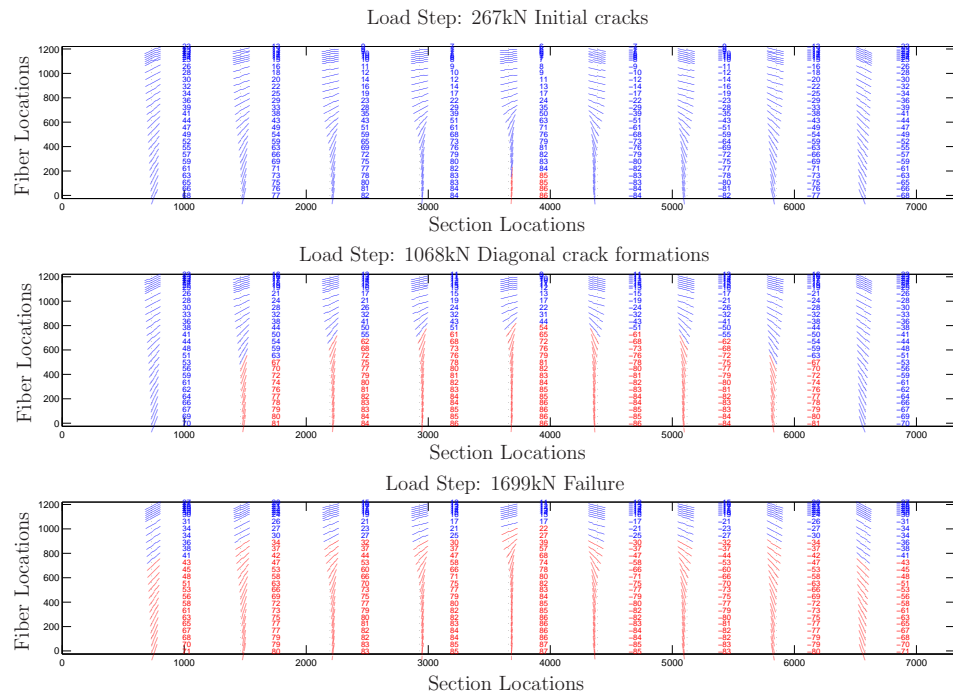


Figure 4.21: Fiber principal axes compression directions

cracks at these locations. The new material extracts crack directions matching with the real test crack propagation and provides the analyst additional information by improving simulations of shear dominant members in OpenSees.

4.6 Verification of DDM Equations

To demonstrate the application of response sensitivity analysis in assessing uncertainty, numerical examples are presented for an interior girder of the McKenzie River Bridge, which carries the northbound lanes of Interstate-5 just north of Eugene, OR. Each span of this reinforced concrete deck girder (RCDG) bridge is 15.2 m long, as shown in Fig. 4.22. The depth, d , of the interior girder is uniform at 122 cm while the girder width, b , is tapered from 33 cm at quarter spans to 50 cm at the continuous supports.

For the two-dimensional analyses presented herein, each span is described as a single force-based element with integration points that correspond to critical locations at midspan and at distances d , $2d$, and $3d$ from the supports:

$$x = \{1.22, 2.44, 3.66, 7.60, 11.6, 12.8, 14.0\} \text{ m} \quad (4.62)$$

These locations dictate where section forces, \mathbf{s} , and the corresponding response sensitivity, $\partial \mathbf{s} / \partial \varphi|_{\mathbf{e}}$, are evaluated during the analysis. The associated integration weights are computed from the average distance between adjacent integration points:

$$w = \{1.83, 1.22, 2.58, 4.00, 2.58, 1.22, 1.83\} \text{ m} \quad (4.63)$$

To verify the DDM equations for section force response sensitivity are correctly

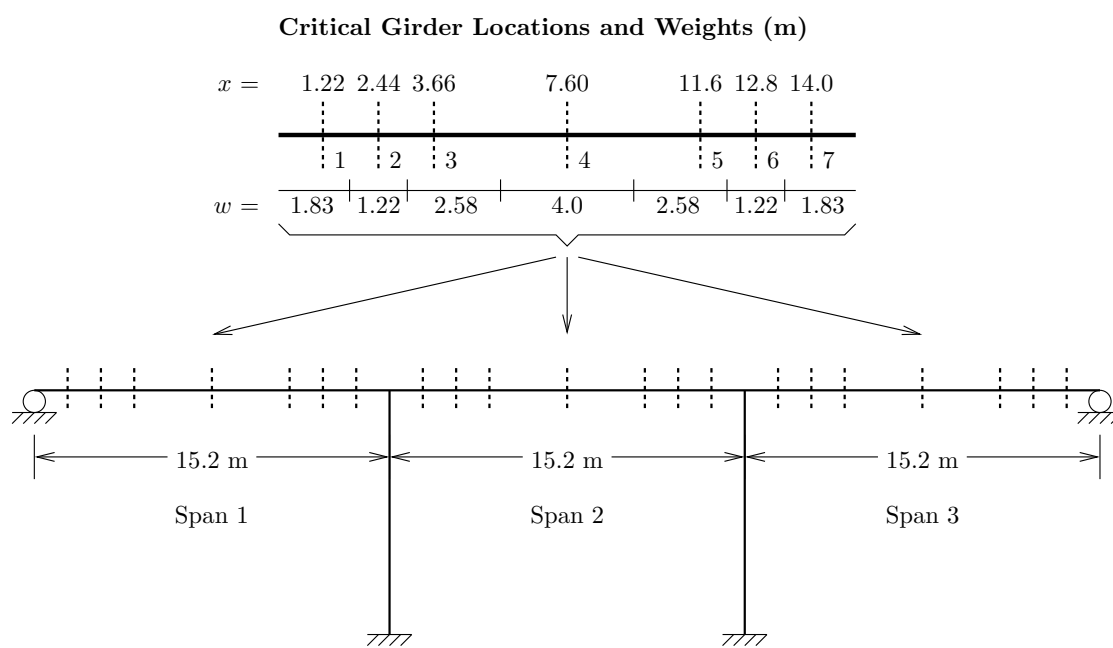


Figure 4.22: Span lengths and critical locations for an interior girder of the McKenzie River Bridge.

implemented in OpenSees, finite difference calculations are carried out with successively smaller parameter perturbations. As the perturbation decreases, the finite difference approximation should converge to the analytic derivative:

$$\lim_{\varepsilon \rightarrow 0} \frac{\mathbf{s}(\varphi + \varepsilon\varphi) - \mathbf{s}(\varphi)}{\varepsilon\varphi} = \frac{\partial \mathbf{s}}{\partial \varphi} \quad (4.64)$$

For the DDM solution, $\partial \mathbf{s} / \partial \varphi$ is recovered from terms on the right-hand side of Eq. (3.31), each of which is known after the DDM equations have been solved during the analysis.

Two numerical examples will present the verification of DDM formulations in this section. First example is the verification of section force sensitivity with respect to material geometry and load parameters when rectangular sections are represented by linear elastic uniaxial concrete and steel material for the axial-flexural behavior at fiber level while an elastic shear stiffness is aggregated for computation of shear strain at section level as given in Eq. (4.5). The second example will verify the sensitivity formulations of proposed biaxial material and the T-beam section geometry under vehicle loading. In both examples The three axle AASHTO HS-20 design truck [3] shown in Fig. 4.23(a) moves across the bridge in load increments and the FDM-DDM sensitivities of section bending moment and shear force will be compared at each load increment step.

4.6.1 Elastic Section Sensitivity Verifications

Section dimensions, reinforcing details, and material properties for the critical sections are listed in Fig. 4.24 where the labels, ij , indicate the span number, i , and the section number, j . The derivatives of bending moment and shear force at

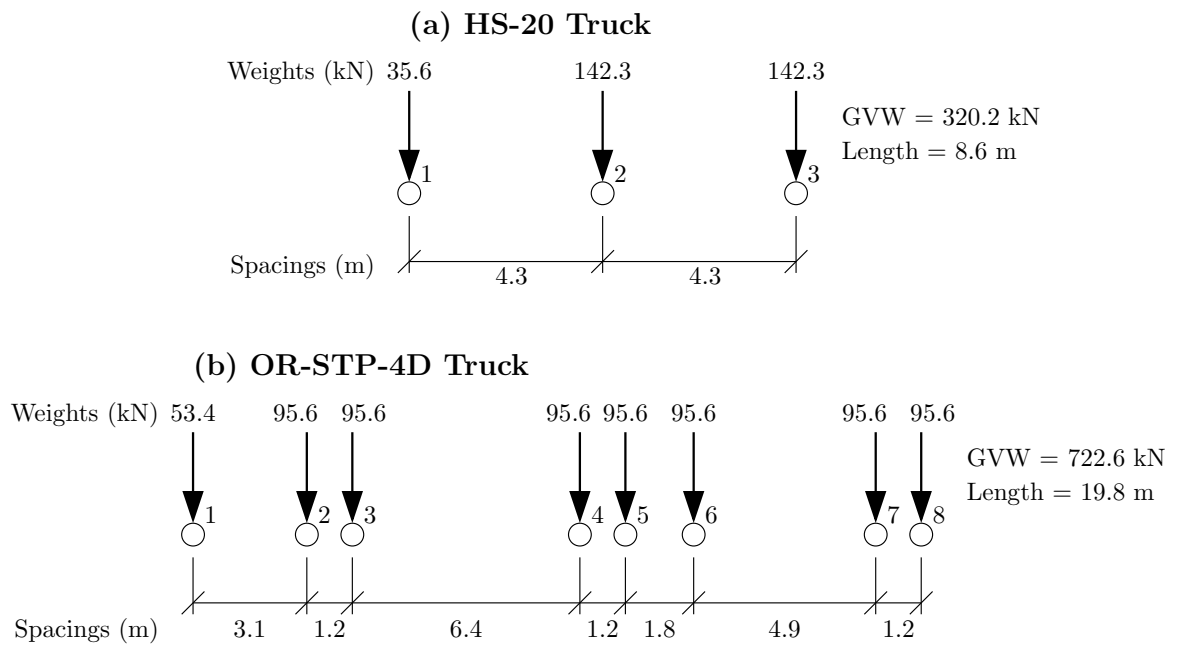


Figure 4.23: Axle weights and spacings of vehicles used in sensitivity and reliability analyses: (a) HS-20 truck; (b) OR-STP-4D single trip permit truck.

section 17 with respect to concrete material properties, section dimensions, area of reinforcement, axle spacing and load magnitudes are presented in Fig. 4.25 and Fig. 4.26, respectively. As anticipated, the results obtained by the FDM converge to those obtained by the DDM at every load increment of the analysis.

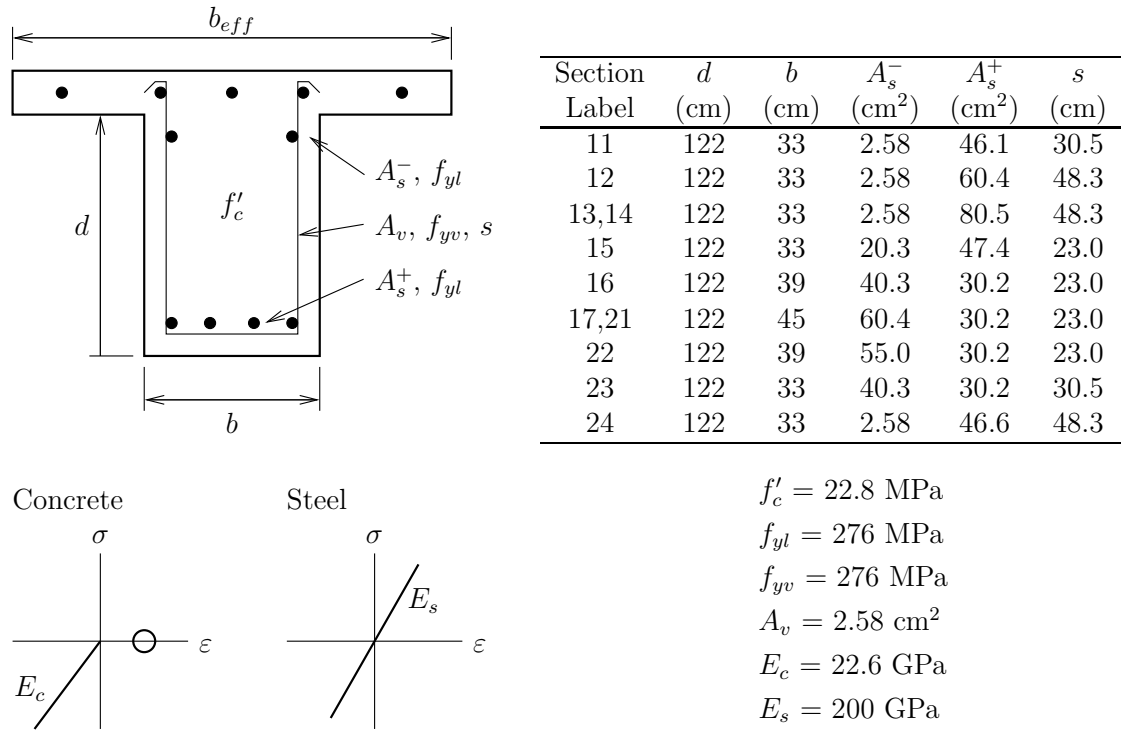


Figure 4.24: Typical reinforcing layout and details for an interior girder of the McKenzie River Bridge.

The sensitivities are multiplied by the initial value of the corresponding parameter such that absolute changes in response can be estimated from Fig. 4.25 for a relative (%) parameter change. The moment of section 17 is much more sensitive to the load parameters than to the material and geometric parameters; however, the section moment is nearly as sensitive to relative changes in section depth as it

is to the axle load. Similar analyses indicate that the shear force response is much less sensitive to the chosen parameters than that for bending moment.

4.6.2 MCFT Material Sensitivity Verifications

The DDM response sensitivity to parameters of the biaxial material is verified using FDM results in this section. The sensitivity formulations have been implemented for initial modulus of elasticity, E_0 , the compression strength, σ_{cu} and the tensile strength, σ_{cr} of the proposed biaxial material. In the analysis, E_0 is taken as $27.5GPa$. The compressive and tensile strength of the concrete fibers are $\sigma_{cu} = 27.6MPa$ and $\sigma_{cr} = 3.24MPa$, respectively. The strain at ultimate compressive stress is taken as $\varepsilon_{cu} = -0.003$. The current and the following examples verifying DDM formulations for the biaxial material, t-beam shape and interpolation parameters are performed with the proposed material.

For the section 17, the moment and shear gradients multiplied by the initial value of the corresponding parameter are shown in Fig. 4.29. The moment of section 17 is much more sensitive to the modulus of elasticity and the tensile strength of the concrete than to the compressive strength; however, the section shear is significantly less sensitive when compared to the section moment. In FDM perturbations, the occurrence of numerical round off errors causes inaccurate results at several time steps. Inaccurate results of FDM encourage usage of DDM sensitivities for the material properties of proposed material model.

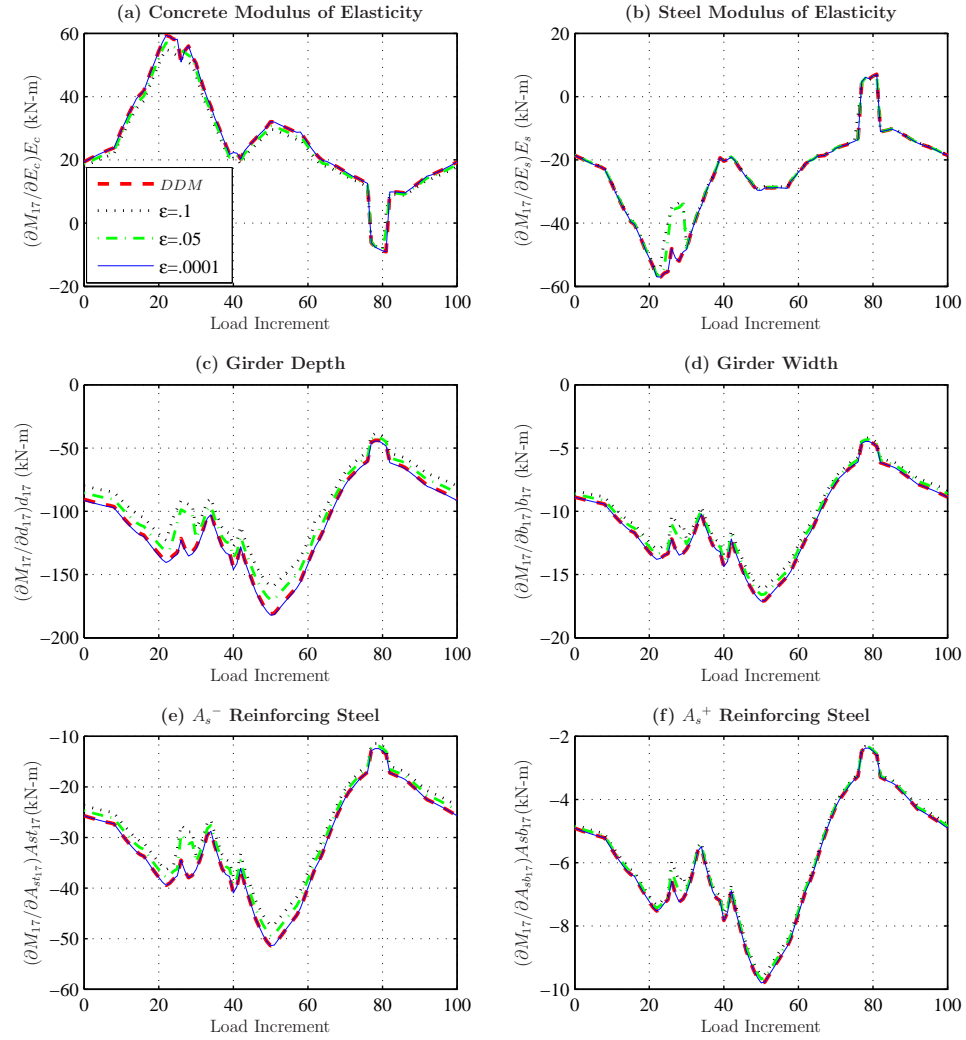


Figure 4.25: Verification of DDM moment response sensitivity computations for moving load analysis of an interior girder of the McKenzie River Bridge with elastic materials and rectangular sections.

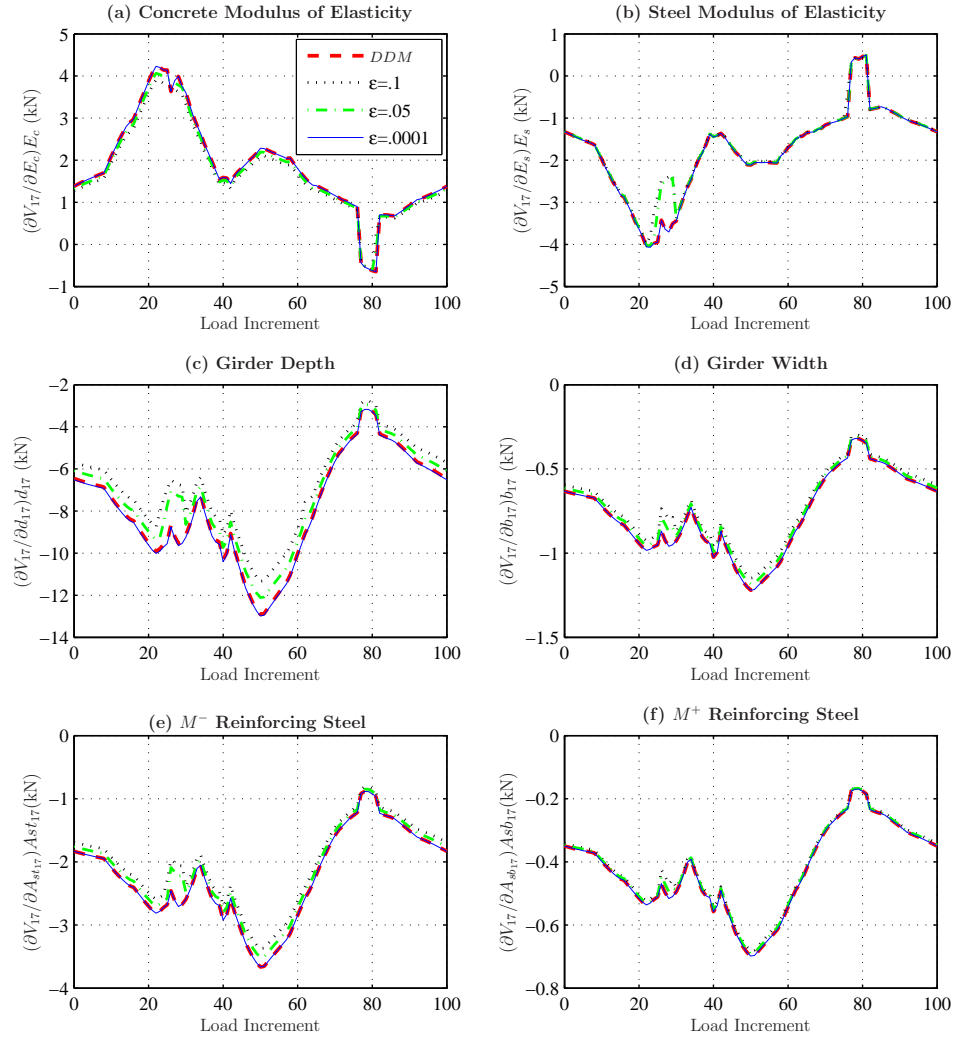


Figure 4.26: Verification of DDM shear response sensitivity computations for moving load analysis of an interior girder of the McKenzie River Bridge for elastic material and rectangular section parameters.

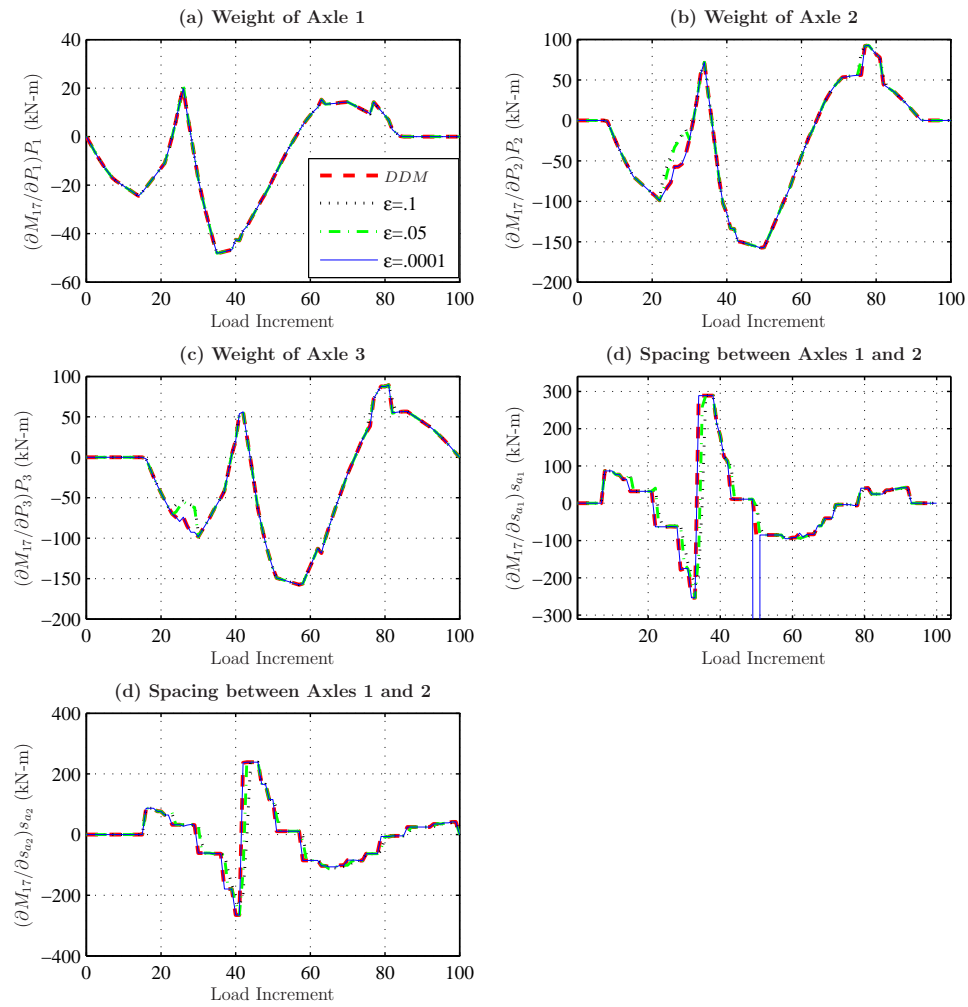


Figure 4.27: Verification of DDM moment response sensitivity computations for moving load analysis of an interior girder of the McKenzie River Bridge for vehicle load parameters.

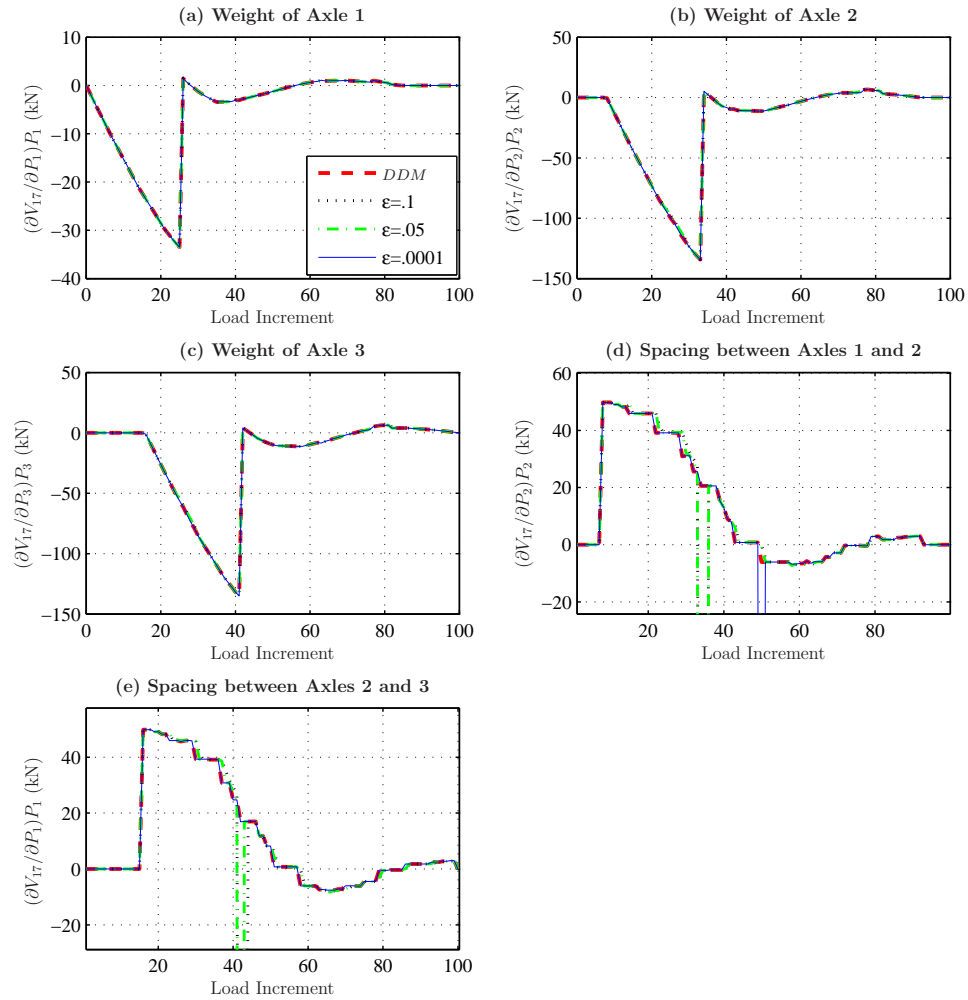


Figure 4.28: Verification of DDM shear response sensitivity computations for moving load analysis of an interior girder of the McKenzie River Bridge for vehicle load parameters.

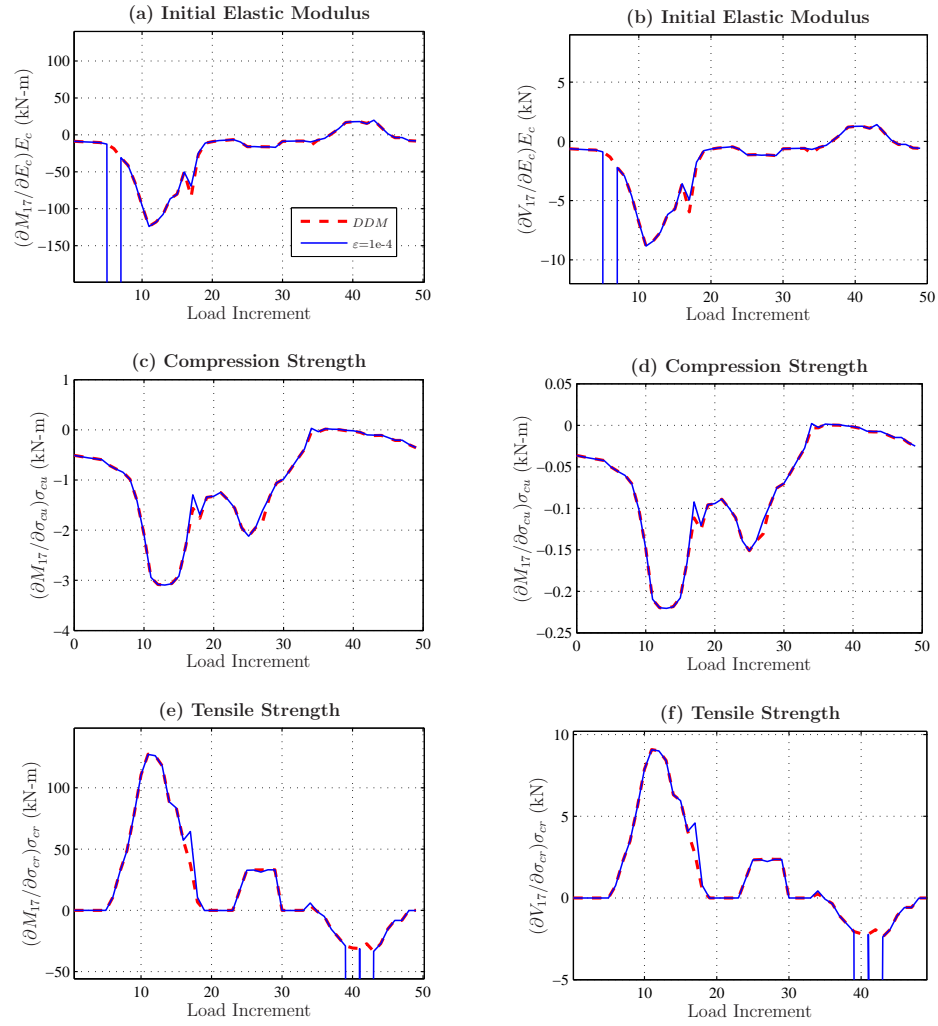


Figure 4.29: Verification of DDM moment-shear response sensitivity computations for moving load analysis of an interior girder of the McKenzie River Bridge for biaxial material parameters.

4.6.3 T-beam Geometry Sensitivity Verifications

The moment and shear sensitivities of section 17 to the shape parameters of T-beam girders are given in Figs. 4.30 and 4.31, respectively. The girder depth, d , the girder web width, b_w , the effective flange width, b_{eff} , the deck thickness, h_f , the negative moment reinforcing steel A_{st} and the positive moment reinforcing steel A_{sb} are considered as sensitivity parameters in this example. The DDM sensitivities show that the section moment is more sensitive to depth, web and the effective flange width when compared to the other shape parameters. However, section shear sensitivities are significantly lower than the moment gradients.

4.7 Reliability Analysis Examples

A set of first-order reliability (FORM) analyses is carried out to assess the effect of parametric uncertainty on the interaction of moment and shear force at the critical locations. The girder investigated in the verification examples is selected and live load reliability analyses are performed using several material-section configurations and the capacity functions implemented to OpenSees framework.

While conservative in design, treating moment and shear separately can lead to non-conservative estimates of reliability. This approach is accounted for applying MB and LC capacity functions in OpenSees. For the demand in finite element reliability, the biaxial material model considers the influence of coupled moment and shear behavior on the demand side of the limit state. The analysis results are compared with examples using uniaxial material model. In addition, the new section shape class is used in examples and compared with the results by rectangular reinforced concrete section. The parameter importance factors are calculated at

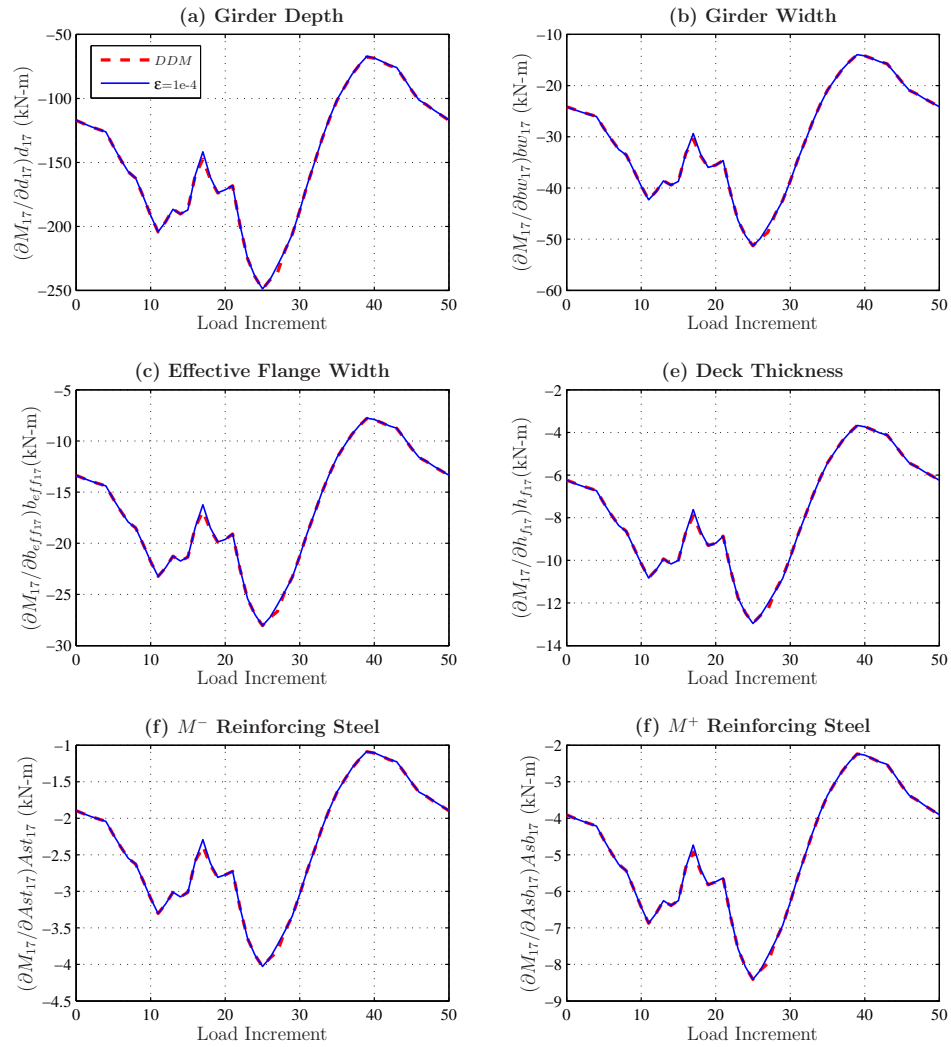


Figure 4.30: Verification of DDM moment response sensitivity computations for moving load analysis of an interior girder of the McKenzie River Bridge for T-beam section parameters.

Figure 4.31: Verification of DDM shear response sensitivity computations for moving load analysis of an interior girder of the McKenzie River Bridge for T-beam sections parameters.

critical load increments.

LC performance functions considered in all reliability analysis is formulated in terms of random finite element response M , V and ultimate moment and shear capacity M_n , V_n :

$$g^- = 1 - \left| \frac{M}{M_n^-} \right|^3 - \left| \frac{V}{V_n} \right|^3 \quad (4.65a)$$

$$g^+ = 1 - \left| \frac{M}{M_n^+} \right|^3 - \left| \frac{V}{V_n} \right|^3 \quad (4.65b)$$

The performance functions of MB are formulated in terms of coefficients that define line equations connecting 6 points of AASHTO-MCFT representations:

$$g_1 = M_n^- + M \quad (4.66a)$$

$$g_2 = cf_{m2}(V_n, M_n^-)M + cf_{v2}(V_n, M_n^-)V + cf_{n2}(V_n, M_n^-) \quad (4.66b)$$

$$g_3 = V_n - V \quad (4.66c)$$

$$g_4 = cf_{m4}(V_n, M_n^+)M + cf_{v4}(V_n, M_n^+)V + cf_{n4}(V_n, M_n^+) \quad (4.66d)$$

$$g_5 = M_n^+ - M \quad (4.66e)$$

In the limit state expressions, $M = IF * DF_M * M_{FE}$ is the bending moment from the finite element analysis, M_{FE} , modified by the impact factor, IF , and moment distribution factor, DF_M . Similarly, the shear, $V = IF * DF_V * V_{FE}$, is obtained from the finite element analysis, impact factor, and shear distribution factor, DF_V . The impact and moment and shear distribution factors are treated as random variables with mean values 1.1, 0.854, and 0.884, respectively, obtained from LRFR specifications [2]. Field testing and three-dimensional analysis of the McKenzie River Bridge [121] offer more realistic estimates of the impact and distribution

factors; however, the use of LRFR values does not affect the analysis methodology presented herein.

To display forms of limit state formulations, MB and LC capacity functions are quantified at mean values of all resistance variables and shown in Fig. 4.32 for sections 17 and 14. The LC approach provides conservative shear strength while the flexural capacities are same in negative and positive directions. In reliability analysis, more conservative reliability indices are anticipated for shear critical section 17 while moment- critical section 14 is expected to converge the similar values. The combined moment- shear behavior in closed form of LC will be compared to linearly interpolated resistance in MB.

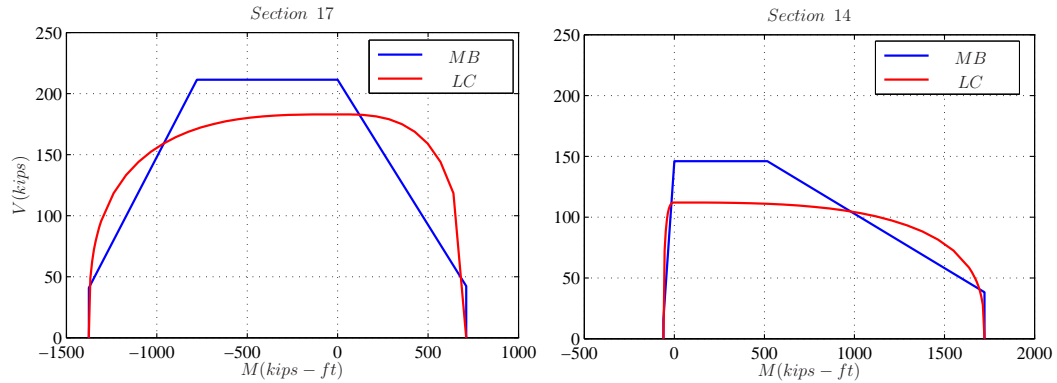


Figure 4.32: MB and LC capacities at mean values of resistance variables

4.7.1 Bridge Girder with Uniaxial and Biaxial Material Models

In the first set of reliability analyses, the interior girder of McKenzie Bridge is modeled using a uniaxial and biaxial concrete material with rectangular sections. The material configurations for two cases is defined in Table 4.3. The reliability

analysis is performed for the two limit state cases, LC and MB at two critical sections 14 and 17. The section 14 is considered as a moment dominant location while section 17 at d distance away from the support is critical due to higher interaction of shear and bending moment expected.

Table 4.3: Material models used in live load reliability of girders.

Fibers	Case 1	Case 2
Concrete	Uniaxial: <i>ElasticENT</i>	nDMaterial: <i>ConcreteMCFTNonlinear</i>
Steel	Uniaxial: <i>LinearElastic</i>	Uniaxial: <i>Steel01</i>
Shear Aggregator	Uniaxial: <i>LinearElastic</i>	<i>N/A</i>

An eight-axle single-trip permit truck, type OR-STP-4D given in Fig. 4.23(b), moves across the bridge in 100 load increments. All axle weights are assumed to be correlated lognormal random variables, with descriptors based on WIM specifications [13]. The correlation between all axle weights is 0.4, while the correlation between axles in the tandem and triple groups (axles 2-3, 4-5-6, and 7-8) is 0.8 [69]. Mixed lognormal distributions for tandem axle configurations are given by Prozzi and Hong [123]. Coefficients of variation for the impact and distribution factors are available in the literature [64, 74] and used in the analysis. All parameters that define $M - V$ and $M_n - V_n$ are treated as random variables with distribution properties shown in Tables 4.4 and 4.5.

The reliability index at each load increment step is shown in Figs. 4.33 and 4.34 for section 17 and 14, respectively. Using the DDM to evaluate sensitivity gradients, the reliability analyses with uniaxial and biaxial material configurations converge to the minimum reliability index, $\beta_{cr} = 2.00$ at section 17, when the limit state is defined by conservative LC approximation. Using MB approach where

Table 4.4: Random variable descriptions for the finite element reliability analysis of an interior girder of the McKenzie River Bridge using uniaxial materials and rectangular sections

Case 1: Uniaxial Elastic					
RV no.	Param.	Distribution	Mean		C.O.V.
			17	14	
1	d	Normal	122 cm		0.015
2	b	Normal	45 cm		0.015
3	A_s^-	Normal	60.4 cm ²	2.6 cm ²	0.024
4	A_s^+	Normal	30.2 cm ²	80.5 cm ²	0.024
5	E_c	Lognormal	22.6 GPa		0.08
6	G	Lognormal	9.41 GPa		0.08
7	E_s	Lognormal	200 GPa		0.06
8	f'_c	Normal	22.8 MPa		0.15
9	A_v	Normal	2.58 cm ²		0.024
10	f_{yv}	Lognormal	276 MPa		0.12
11	s	Normal	23 cm	48 cm	0.10
12	f_{yt}	Lognormal	276 MPa		0.12
13	DF_M	Normal	0.854		0.10
14	DF_V	Normal	0.884		0.10
15	IF	Normal	1.10		0.08
16	P_1	Lognormal	53 kN		0.20
17-23	P_2 - P_8	Lognormal	96 kN		0.20
24	b_{eff}	Normal	227 cm	215 cm	0.015
25	DL	Lognormal	2.26 kNm		0.10

Table 4.5: Random variable descriptions for the finite element reliability analysis of an interior girder of the McKenzie River Bridge using biaxial concrete material and rectangular sections

Case 2: Biaxial Nonlinear					
RV no.	Param.	Distribution	Mean		C.O.V.
			17	14	
1	d	Normal	122 cm		0.015
2	b	Normal	45 cm		0.015
3	A_s^-	Normal	60.4 cm ²	2.6 cm ²	0.024
4	A_s^+	Normal	30.2 cm ²	80.5 cm ²	0.024
5	E_c	Lognormal	22.6 GPa		0.08
6	f'_c	Normal	22.8 MPa		0.15
7	f_{cr}	Normal	3.3 MPa		0.15
8	E_s	Lognormal	200 GPa		0.06
9	f_{yt}	Lognormal	276 MPa		0.12
10	A_v	Normal	2.58 cm ²		0.024
11	f_{yv}	Lognormal	276 MPa		0.12
12	s	Normal	23 cm	48 cm	0.10
13	DF_M	Normal	0.854		0.10
14	DF_V	Normal	0.884		0.10
15	IF	Normal	1.10		0.08
16	P_1	Lognormal	53 kN		0.20
17-23	P_2-P_8	Lognormal	96 kN		0.20
24	b_{eff}	Normal	227 cm	215 cm	0.015
25	DL	Lognormal	2.26 kNm		0.10

MCFT parameters, $\beta^* - \theta^*$, are not deterministic, the critical reliability index is computed $\beta_{cr} = 2.59$ as shown in Fig. 4.33(b) for g_2 representing the negative bending moment and shear interaction. Regardless of the specified performance function, the linear elastic material case (Case 1) converges to the same critical value with the biaxial material case (Case 2) for the section 17 where high shear-moment interaction occurs. However, LC approximation provides conservative results when compared to MB approach at critical load increment.

At section 14, where the most probable failure mode is due to the moment limit state, the critical reliability index is converged to $\beta_{cr} = 3.40$ at the load increment step 27. As the influence of MCFT parameters on ultimate moment capacity is not significant, the LC approximation converges to MB approach as shown in Fig. 4.34(c). Meanwhile, Case 1 provides conservative results when compared to the nonlinear Case 2.

For the critical load increment, the ranking of the RVs according to the importance measures (γ -values) is shown in Tables 4.6 and 4.7 for Case 1 and 2, respectively. The random variables that characterize the impact factor and shear distribution factor rank highest in importance, which reflects the large amount of epistemic uncertainty in estimating dynamic effects and three-dimensional load distribution for this type of bridge analysis. Moreover, the vehicle axle loads have significant γ -values in demand. Due to the strong correlation assigned to axle loads 4 through 6, each random variable assigned to these axles has similar importance factors on the limit state function for the section 17. On the other hand, the axle loads causing maximum moment demand at step 27 take the higher importance factors for section 14. In addition, the variation in dead load is another important parameter with the γ -value over 0.1 for all cases.

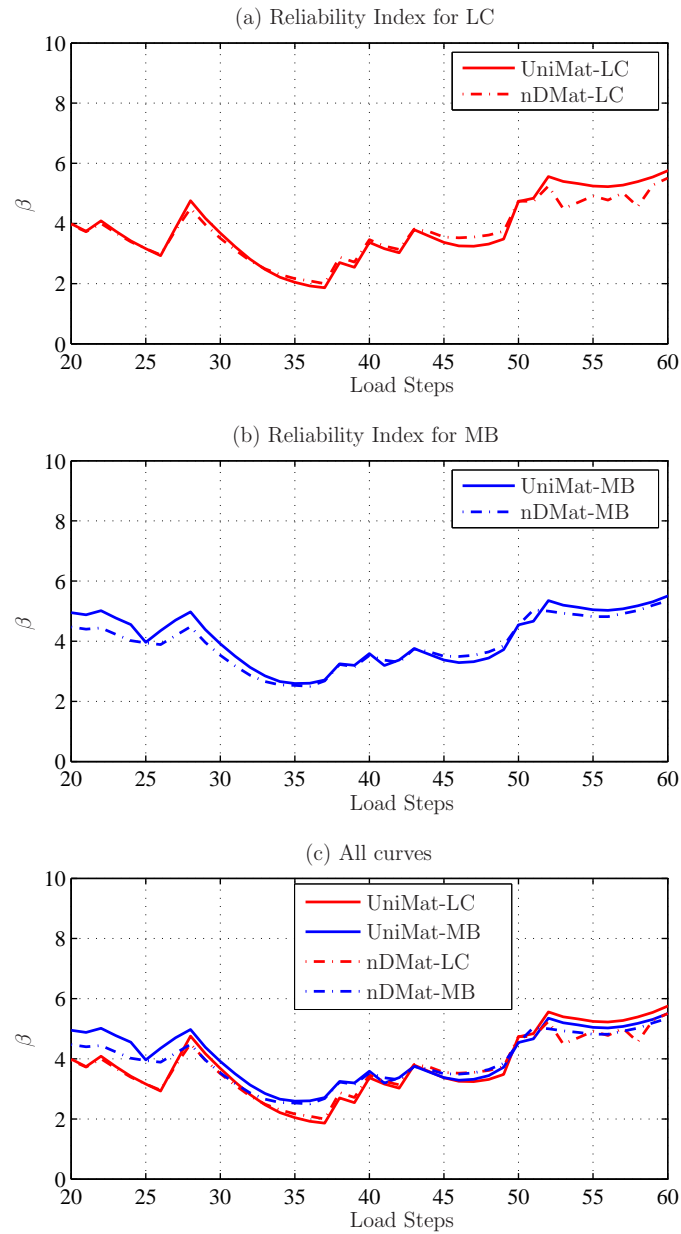


Figure 4.33: Reliability analysis for moment-shear interaction at rectangular section 17: (a) M-V capacity by LC, (b) M-V capacity by MB, (c) All curves

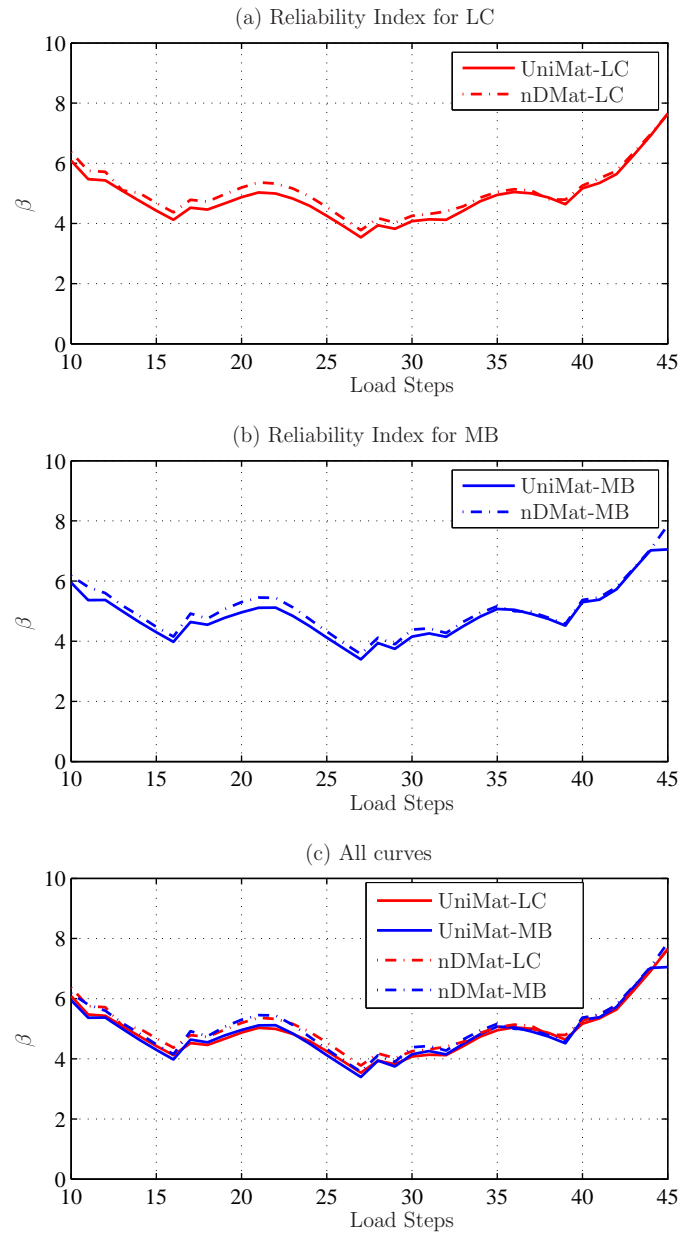


Figure 4.34: Reliability analysis for moment-shear interaction at rectangular section 14: (a) M-V capacity by LC, (b) M-V capacity by MB, (c) All curves

The longitudinal steel yield stress, f_{yl} , is the most important resistance variable in the analysis for section 14. The most probable failure is due to excessive bending moment for LC and MB limit state so that, the importance factors of resistance parameters are similar in both cases.

At section 17, the high ranking of both moment and shear distribution factors highlights the interaction of moment and shear at the failure point in MB. The most probable failure mode is calculated on g_2 and the influence of DF_V and DF_M is similar on the reliability index. The most important resistance parameter is f_{yl} with the γ -value of -0.577 for Case 1 and -0.583 for Case 2.

The nominal shear capacity in LC is smaller than the shear cap of MB approach. The limit state considering deterministic values of $\beta = 2.0$ and $\theta = 45^\circ$ converges to a conservative reliability index. The shear and moment capacity parameters, f_{yv} , f'_c , f_{yl} , f_{yv} have shared high influence on the reliability index in LC. On the demand side, shear influence is highlighted with γ -value for DF_V higher than DF_M .

Table 4.6: Importance measures (γ -values) of the random variables for uniaxial elastic material at the critical load increment.

Material: Uniaxial Elastic					
Section: Rectangular 14 - 17					
RVno.		14		17	
		LC	MB	LC	MB
1	d	-0.075	-0.061	-0.085	-0.052
2	b	-0.014	-0.001	-0.038	-0.008
3	A_s^-	0.001	0.001	-0.026	-0.111
4	A_s^+	-0.082	-0.099	-0.001	-0.015
5	E_c	0.006	0.007	0.004	0.008
6	G	-0.001	-0.001	0.001	0.001
7	E_s	0.005	0.007	0.011	0.022
8	f'_c	-0.092	-0.044	-0.212	-0.025
9	A_v	-0.013	0.003	-0.051	-0.018
10	f_{yv}	-0.063	-0.057	-0.252	-0.078
11	s	0.008	0.004	0.031	0.056
12	f_{yl}	-0.415	-0.390	-0.157	-0.577
13	DF_M	0.318	0.341	0.134	0.294
14	DF_V	0.147	0.133	0.430	0.215
15	IF	0.369	0.377	0.451	0.402
16	P_1	-0.012	-0.016	0.026	0.054
17	P_2	0.006	0.007	0.058	0.101
18	P_3	0.020	0.024	0.058	0.095
19	P_4	0.319	0.323	0.150	0.092
20	P_5	0.261	0.264	0.159	0.110
21	P_6	0.176	0.177	0.155	0.114
22	P_7	0.000	0.000	0.099	0.075
23	P_8	0.000	0.000	0.080	0.057
24	b_{eff}	-0.001	0.000	0.000	0.000
25	DL	0.121	0.125	0.204	0.191

Table 4.7: Importance measures (γ -values) of the random variables for nonlinear nDMaterial at the critical load increment.

Material: Biaxial Nonlinear					
Section: Rectangular 14 - 17					
RVno.		14		17	
		LC	MB	LC	MB
1	d	-0.073	-0.054	-0.080	-0.040
2	b	-0.009	-0.001	-0.034	-0.007
3	A_s^-	0.000	0.000	-0.038	-0.111
4	A_s^+	-0.077	-0.098	-0.000	0.000
5	E_c	0.006	0.007	0.010	0.040
6	f'_c	-0.096	-0.037	-0.189	-0.016
7	f_{cr}	0.005	0.005	0.020	0.024
8	E_s	0.009	0.009	0.011	0.017
9	f_{yl}	-0.421	-0.375	-0.217	-0.583
10	A_v	-0.013	-0.003	-0.044	-0.015
11	f_{yv}	-0.065	-0.058	-0.221	-0.083
12	s	0.008	0.022	0.028	0.071
13	DF_M	0.321	0.335	0.181	0.309
14	DF_V	0.162	0.144	0.397	0.220
15	IF	0.381	0.380	0.459	0.417
16	P_1	0.011	0.012	0.026	0.042
17	P_2	0.005	0.007	0.054	0.081
18	P_3	0.020	0.023	0.054	0.078
19	P_4	0.329	0.326	0.147	0.088
20	P_5	0.270	0.265	0.156	0.092
21	P_6	0.138	0.176	0.154	0.113
22	P_7	0.000	0.000	0.101	0.091
23	P_8	0.000	0.000	0.081	0.070
24	b_{eff}	0.000	-0.003	0.000	0.000
25	DL	0.131	0.135	0.206	0.190

4.7.2 Bridge Girder with T-Section Model

In the second set of reliability analyses, the same interior girder of McKenzie River Bridge is represented with T-beam in FEA using the section integration class, *RCTBeamSectionIntegration*. The reliability analysis is repeated with two material cases for two limit state functions, LC and MB. Additional shape sensitivity parameters, b_{eff} and h_f , are accounted for in both demand and resistance side of the limit state function. The updated random variables are shown in Tables 4.8 and 4.9 for Case 1 and 2, respectively. For the same truck loading FORM analysis has been carried out at sections 14 and 17 for each load increment step.

The reliability index at each load step is displayed with the results from the first analysis set for section 17 and 14 in Figs. 4.35 and 4.36, respectively. At section 17, the critical beta value for Case 2, is not significantly sensitive to T-shape parameters the reliability index and converges to the same critical value whether the limit state definition is LC or MB. The LC approximation again presents a conservative result, $\beta_{cr} = 2.01$, while MB extracts $\beta_{cr} = 2.18$. However, for zero-tension and linear elastic-compression case of concrete (Case 1), the probability of failure decreases with T-shape section when compared to the rectangular shape. Since the negative moment demand decreases with the change in shape, the reliability index for interaction line g_2 of MB increases.

The contribution of effective width is considered in both demand and resistance side of the limit state function. The critical reliability index converges to the same value in LC and MB approach at flexural dominant section 14. The reliability indices are computed as $\beta_{cr} = 3.44$ for LC and $\beta_{cr} = 3.69$ for MB in Case 1. Meanwhile, in nonlinear Case 2 demand on sections decreases so that LC and MB analyses extract higher reliability indices, $\beta_{cr} = 3.86$ and $\beta_{cr} = 4.10$, respectively.

Table 4.8: Random variable descriptions for the finite element reliability analysis of an interior girder of the McKenzie River Bridge using uniaxial material and T-sections.

Case 1: Uniaxial Elastic					
RV no.	Param.	Distribution	Mean		C.O.V.
			17	14	
1	d	Normal	122 cm		0.015
2	b	Normal	45 cm		0.015
3	b_{eff}	Normal	227 cm	215 cm	0.015
4	h_f	Normal	15 cm		0.015
5	A_s^-	Normal	60.4 cm ²	2.6 cm ²	0.024
6	A_s^+	Normal	30.2 cm ²	80.5 cm ²	0.024
7	E_c	Lognormal	22.6 GPa		0.08
8	G	Lognormal	9.41 GPa		0.08
9	E_s	Lognormal	200 GPa		0.06
10	f'_c	Normal	22.8 MPa		0.15
11	A_v	Normal	2.58 cm ²		0.024
12	f_{yv}	Lognormal	276 MPa		0.12
13	s	Normal	23 cm	48 cm	0.10
14	f_{yt}	Lognormal	276 MPa		0.12
15	DF_M	Normal	0.854		0.10
16	DF_V	Normal	0.884		0.10
17	IF	Normal	1.10		0.08
18	P_1	Lognormal	53 kN		0.20
19-25	P_2-P_8	Lognormal	96 kN		0.20
26	DL	Lognormal	2.26 kNm		0.10

Table 4.9: Random variable descriptions for the finite element reliability analysis of an interior girder of the McKenzie River Bridge biaxial material and T-sections.

Case 2: Biaxial Nonlinear					
RV no.	Param.	Distribution	Mean		C.O.V.
			17	14	
1	d	Normal	122 cm		0.015
2	b	Normal	45 cm		0.015
3	b_{eff}	Normal	227 cm	215 cm	0.015
4	h_f	Normal	15 cm		0.015
5	A_s^-	Normal	60.4 cm ²	2.6 cm ²	0.024
6	A_s^+	Normal	30.2 cm ²	80.6 cm ²	0.024
7	E_c	Lognormal	22.6 GPa		0.08
8	f'_c	Normal	22.8 MPa		0.15
9	f_{cr}	Normal	3.3 MPa		0.15
10	E_s	Lognormal	200 GPa		0.06
11	f_{yv}	Lognormal	276 MPa		0.12
12	A_v	Normal	2.58 cm ²		0.024
13	f_{yt}	Lognormal	276 MPa		0.12
14	s	Normal	23 cm	48 cm	0.10
15	DF_M	Normal	0.854		0.10
16	DF_V	Normal	0.884		0.10
17	IF	Normal	1.10		0.08
18	P_1	Lognormal	53 kN		0.20
19-25	P_2-P_8	Lognormal	96 kN		0.20
26	DL	Lognormal	2.26 kNm		0.10

For the critical load position, the ranking of the RVs according to the importance measures (γ -values) is shown in Tables 4.10 and 4.11, for Case 1 and 2, respectively. The longitudinal steel yield stress, f_{yl} , is the most important resistance variable in the analysis for section 14 in all cases. For section 17, the interaction line g_2 is still the most probable failure mode in MB and f_{yl} is placed at the top of the resistance parameters. For section 17, the T-shape section model reflects the difference in response with Case 1 and 2. However, the influence of shape parameters on design point stay at a negligibly small in the second set of analyses.

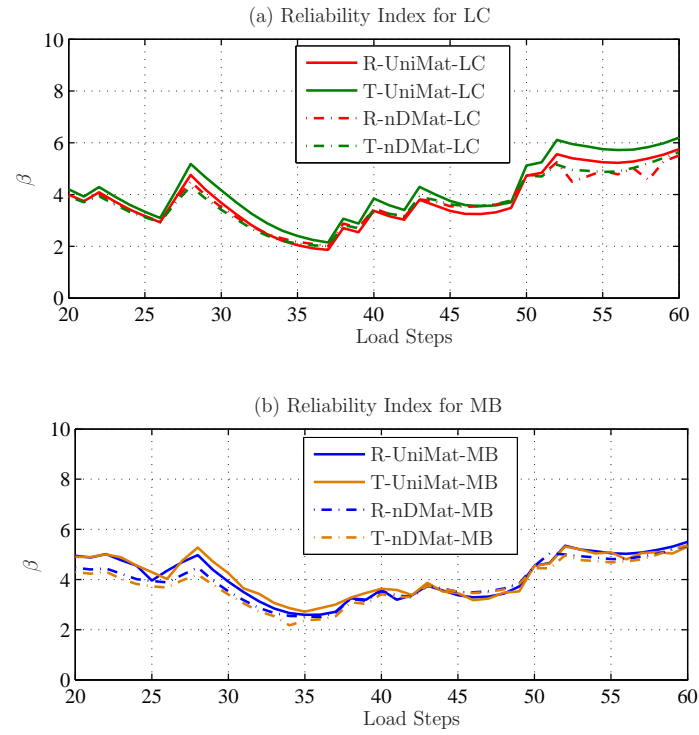


Figure 4.35: Reliability analysis for moment-shear interaction at T-beam section 17: (a) M-V capacity by LC, (b) M-V capacity by MB

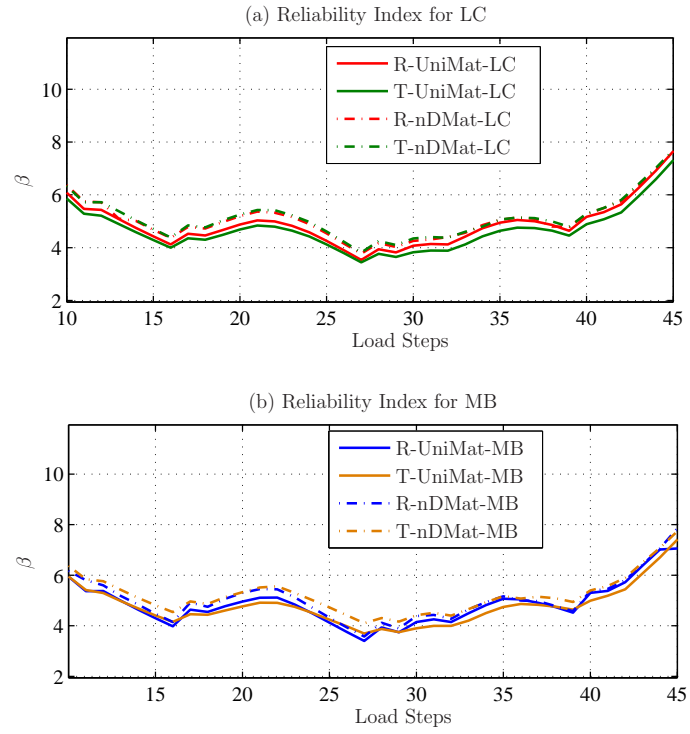


Figure 4.36: Reliability analysis for moment-shear interaction at T-beam section 14: (a) M-V capacity by LC, (b) M-V capacity by MB

Table 4.10: Importance measures of the random variables for Uniaxial elastic material at the critical load increment

Material: Uniaxial Elastic					
Section: T-shape 14 - 17					
RVno.		14		17	
		LC	MB	LC	MB
1	d	-0.077	-0.059	-0.084	-0.045
2	b	-0.014	0.001	-0.041	0.007
3	b_{eff}	-0.001	-0.001	0.000	0.000
4	h_f	0.001	0.001	0.000	0.000
5	A_s^-	0.000	0.000	-0.017	-0.117
6	A_s^+	-0.084	-0.105	-0.001	0.001
7	E_c	0.002	0.003	0.003	0.007
8	G	-0.001	-0.001	0.000	0.003
9	E_s	0.007	0.011	0.010	0.024
10	f'_c	-0.082	-0.011	-0.226	-0.010
11	A_v	-0.011	-0.001	-0.054	-0.016
12	f_{yv}	-0.055	-0.022	-0.269	-0.087
13	s	0.008	0.012	0.034	0.069
14	f_{yl}	-0.439	-0.541	-0.110	-0.598
15	DF_M	0.336	0.367	0.095	0.269
16	DF_V	0.130	0.065	0.452	0.229
17	IF	0.371	0.350	0.440	0.393
18	P_1	0.011	0.015	0.022	0.055
19	P_2	0.005	0.008	0.051	0.110
20	P_3	0.019	0.028	0.052	0.105
21	P_4	0.311	0.283	0.166	0.090
22	P_5	0.255	0.231	0.168	0.103
23	P_6	0.171	0.154	0.156	0.103
24	P_7	0.000	0.000	0.091	0.063
25	P_8	0.000	0.000	0.073	0.048
26	DL	0.132	0.135	0.196	0.190

Table 4.11: Importance measures of the random variables for Nonlinear nDMaterial at the critical load increment

Material: Biaxial Nonlinear					
Section: T-shape 14 - 17					
RVno.		14		17	
		LC	MB	LC	MB
1	d	-0.072	-0.061	-0.081	-0.048
2	b	-0.017	0.002	-0.036	0.007
3	b_{eff}	0.001	-0.001	0.001	0.002
4	h_f	0.001	0.001	0.001	0.001
5	A_s^-	0.001	-0.000	-0.035	-0.113
6	A_s^+	-0.078	-0.103	-0.001	0.000
7	E_c	0.006	0.001	0.018	0.030
8	f'_c	0.104	0.010	0.208	0.009
9	f_{cr}	0.011	0.017	0.003	0.002
10	E_s	0.012	0.019	0.003	0.005
11	f_{yl}	-0.407	-0.549	-0.183	-0.557
12	A_v	-0.013	-0.012	-0.046	-0.017
13	f_{yv}	-0.067	-0.034	-0.226	-0.072
14	s	0.008	0.001	0.028	0.053
15	DF_M	0.309	0.354	0.154	0.298
16	DF_V	0.165	0.077	0.405	0.204
17	IF	0.375	0.349	0.446	0.397
18	P_1	0.008	0.014	0.023	0.042
19	P_2	0.004	0.008	0.052	0.080
20	P_3	0.016	0.027	0.052	0.076
21	P_4	0.320	0.285	0.142	0.096
22	P_5	0.260	0.229	0.155	0.119
23	P_6	0.172	0.149	0.160	0.136
24	P_7	0.000	0.000	0.115	0.100
25	P_8	0.000	0.000	0.095	0.077
26	DL	0.124	0.126	0.212	0.203

4.7.3 The Framework for Live Load Reliability Analysis of Bridge Girders

To demonstrate the features of the live load finite-element reliability methodology, a numerical example involving multiple sections of a reinforced concrete bridge girder is analyzed using the proposed framework. The analysis is carried out with the previously presented TCL scripts programming OpenSees for a probabilistic evaluation. The primary purpose of this framework is to estimate the probability of achieving structural performance criteria specified in code requirements and to obtain importance measures to identify the uncertain parameters.

The interior girder of McKenzie River Bridge girder is selected to perform a multi section live load reliability analysis in the framework. The critical section array, $Cr = \{11, \dots, 37\}$ (Fig. 4.22) indicates all locations where the specified performance function is investigated. To reduce the computational effort FERA of girders, the Case 1 material model and rectangular section integration are selected in analyses. Albeit the LC approximation provides conservative results for shear critical sections, MB approach is adapted in the framework to demonstrate the resistance specified by AASHTO-LRFD in the limit state function. The random variables are geometry and material parameters of each section in Cr array. The analysis is not treated as a system reliability evaluation so that the limit state function at each section is investigated individually.

The section arrays containing properties are given in (Fig. E.1.1) and all random variables in 21 sections are listed in Table 4.12. The section geometry of each section is considered as random variable in structural analysis. Concrete Young's modulus E_c , shear modulus G , and reinforcing steel Young's modulus E_s are taken

as three random variables for each of three force-based elements. E_c , G and f'_c are highly correlated with a coefficient of correlation 80%. The parameters with Rv no. bigger than 94 are taken as the resistance variables of only the corresponding critical section.

Table 4.12: Random variable descriptions in the multiple section FERA.

RV no.	Param.	Distribution	Mean	C.O.V.
1-21	d	Normal	Fig. E.1	0.015
22-42	b	Normal	Fig. E.1	0.015
43-45	E_c	Lognormal	22.6 GPa	0.08
46-48	E_s	Lognormal	200 GPa	0.06
49-51	G	Lognormal	9.41 GPa	0.08
52-72	A_s^-	Normal	Fig. E.1	0.024
73-93	A_s^+	Normal	Fig. E.1	0.024
94	DL	Lognormal	2.26kNm	0.10
95	f'_c	Normal	22.8 MPa	0.15
96	f_{yl}	Lognormal	276 MPa	0.12
97	f_{yv}	Lognormal	276 MPa	0.12
98	A_v	Normal	Fig. E.1	0.024
99	s	Normal	Fig. E.1	0.10
100	b_{eff}	Lognormal	Fig. E.1	0.024
101	DF_M	Normal	0.854	0.10
102	DF_V	Normal	0.884	0.10
103	IF	Normal	1.10	0.08
104	P_1	Lognormal	53 kN	0.20
105-111	P_2-P_8	Lognormal	96 kN	0.20

The typical output of the live load reliability framework is extracted after a post-procedure by TCL scripts. The reliability index of each section is given for load increments 0-100 in Fig. 4.38. At load increment step 36, the evaluations converge to the minimum reliability index, $\beta_{cr} = 2.11$ for section 16, shown in Fig. 4.38 (a). This critical reliability index corresponds to a 1.74% probability of

failure due to exceeding shear capacity at section 16.

For the critical load position, the ranking of the RVs according to the importance measures (γ -values) presented by labels indicate the random variables whose γ -value exceeds 0.10, and these variables are ranked in Table 4.13. The random variables that characterize the impact factor and shear distribution factor rank highest in importance. The longitudinal steel yield stress, f_{yl} , is the most important resistance variable in the analysis, followed by the reinforcing steel area, A_s^- . The stirrup spacing, s , acting as a demand parameter has also the γ -value that exceeds 0.10.

AAHSTO-LRFD formulations indicates the significant influence of flexural parameters due to a regulation limiting the ultimate shear strength. The code restricts the shear cap to satisfy $V_u = M_u/d_v$ condition while interpolating M_u values on interaction diagram. The procedure determining AASHTO-LRFD moment-shear interaction diagrams is detailed in Appendix (A.1). At section 16, the shear cap at converged design point is formulated by the linear interpolation between two controlling points heavily affected by longitudinal yield. Thus, the γ -values for longitudinal parameters are significant for this section.

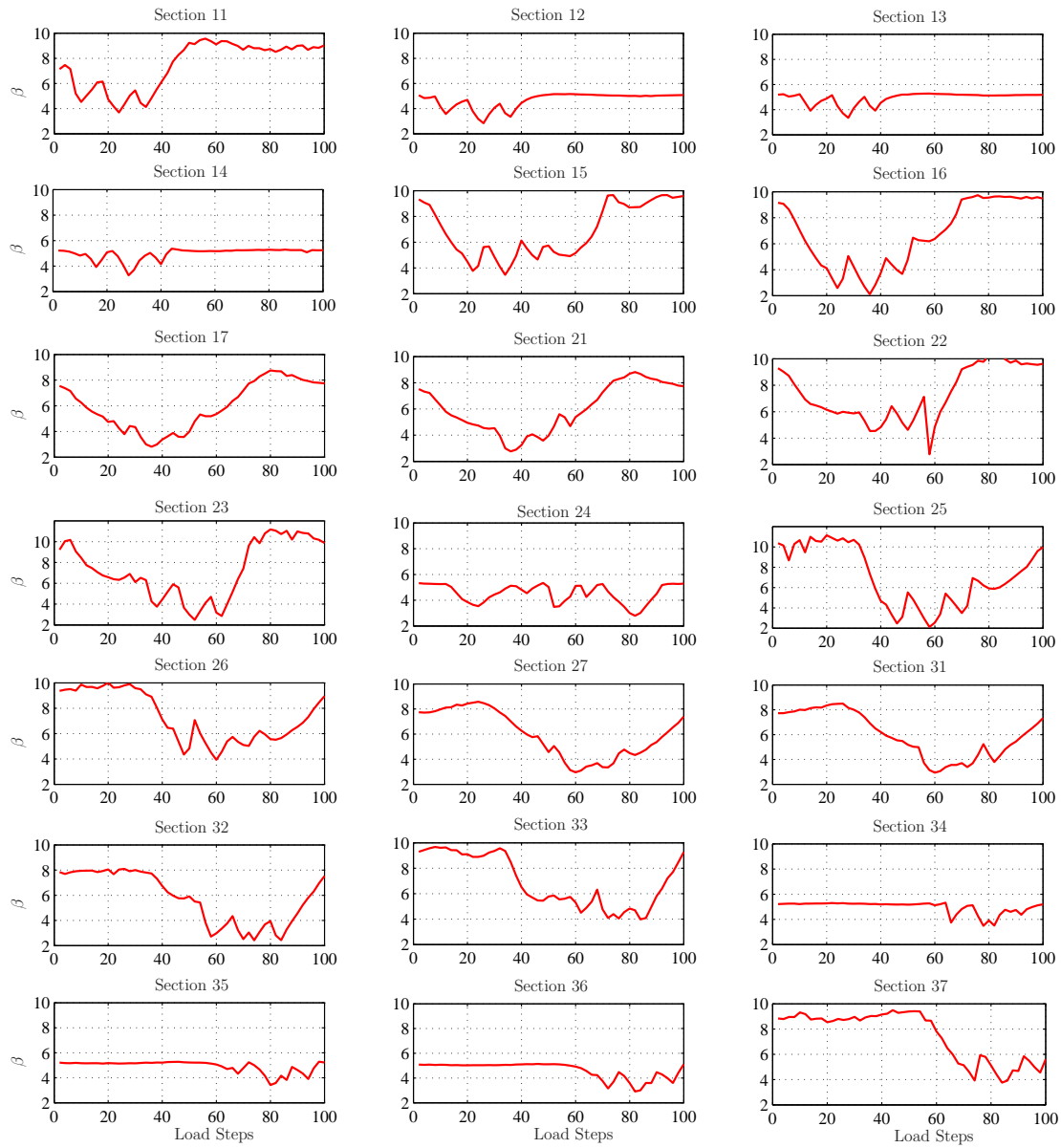


Figure 4.37: Reliability analysis at all sections on an interior girder of the McKenzie River Bridge: Reliability index for load increments 0-100.

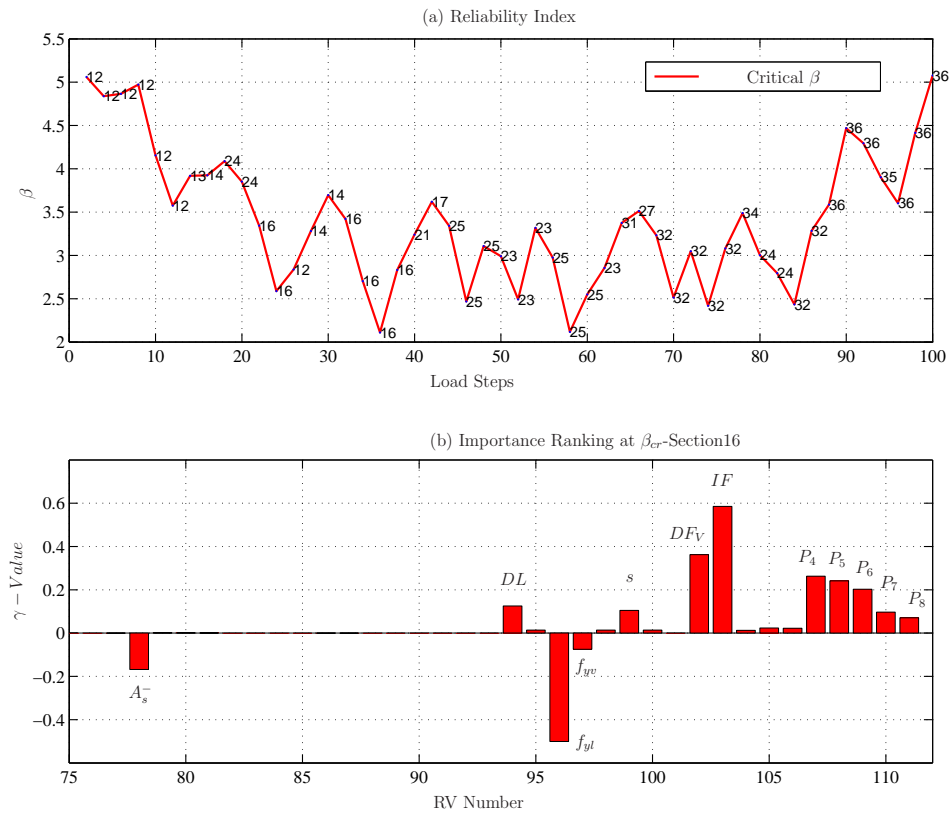


Figure 4.38: Reliability analysis at all sections on an interior girder of the McKenzie River Bridge: (a) Critical reliability index for load increments 0-100; (b) Importance measures of the random variables at the critical load location with RV numbers on the x-axis.

Table 4.13: Ranking of random variables with importance measure exceeding 0.1 in the McKenzie Bridge girder example.

RVno.	Parameter	γ-Value
103	IF	0.585
96	f_{yl}	-0.501
102	DF_V	0.362
107	P_4	0.262
108	P_5	0.241
109	P_6	0.202
78	A_s^-	-0.168
94	DL	0.125
99	s	0.104

Chapter 5 – Reinforced Concrete Bridge Column Sensitivity and Reliability

In this section of the study, the attention turns to a significant modeling uncertainty in force-based column elements. First, the direct differentiation of force-based element formulations is continued and the analytic response sensitivity for interpolatory quadrature is obtained. Then, a discussion on integration methods to represent both strain-softening and -hardening behavior of reinforced concrete columns leads to a new regularization technique that represents both types of behavior without needing a priori. The features of the response sensitivity in reliability analysis are demonstrated on force-based column members while parameters of regularization technique are considered as epistemic uncertainties counted in finite element modeling of bridge piers.

5.1 Interpolatory Quadrature Sensitivity

To quantify the response sensitivity to interpolatory quadrature considered as modeling uncertainty, finite element formulations need to be differentiated in terms of weights and locations of integration points. This section continues formulating target gradient $\partial \mathbf{q} / \partial \varphi|_{\mathbf{v}}$ of response sensitivity.

As the derivation of the response gradient begins by differentiation of the equilibrium in Eq. (3.1), the derivative of the force interpolation matrix is

$$\frac{\partial \mathbf{b}}{\partial \varphi} = \frac{1}{L} \begin{bmatrix} 0 & 0 & 0 \\ 0 & 1 & 1 \\ 0 & 0 & 0 \end{bmatrix} \frac{\partial x_i}{\partial \varphi} \quad (5.1)$$

where $\partial x_i / \partial \varphi$ is the derivative of the i^{th} integration point location. In obtaining Eq. (5.1), it is assumed the element length, L , is deterministic, i.e., that $\partial L / \partial \varphi = 0$.

Differentiation of Eq. (3.3) gives the derivative of the element deformations in terms of the derivatives of the section deformations, the force interpolation matrix, and the integration weights:

$$\frac{\partial \mathbf{v}}{\partial \varphi} = \sum_{i=1}^N \left(\mathbf{b}^T \frac{\partial \mathbf{e}}{\partial \varphi} + \frac{\partial \mathbf{b}^T}{\partial \varphi} \mathbf{e} \right) w_i + \sum_{i=1}^N \mathbf{b}^T \mathbf{e} \frac{\partial w_i}{\partial \varphi} \quad (5.2)$$

After manipulation and combination of Eqs. (3.30) and (5.2) by a process identical to that outlined in [131], the conditional derivative of the basic forces is

$$\left. \frac{\partial \mathbf{q}}{\partial \varphi} \right|_{\mathbf{v}} = \mathbf{k} \sum_{i=1}^N \mathbf{b}^T \mathbf{f}_s \left(\left. \frac{\partial \mathbf{s}}{\partial \varphi} \right|_{\mathbf{e}} - \frac{\partial \mathbf{b}}{\partial \varphi} \mathbf{q} \right) w_i - \mathbf{k} \sum_{i=1}^N \left(\frac{\partial \mathbf{b}^T}{\partial \varphi} \mathbf{e} w_i + \mathbf{b}^T \mathbf{e} \frac{\partial w_i}{\partial \varphi} \right) \quad (5.3)$$

The term $\partial \mathbf{s} / \partial \varphi|_{\mathbf{e}}$ represents the contribution of the section constitutive response to the element sensitivity, whereas the derivatives $\partial \mathbf{b} / \partial \varphi$ and $\partial w_i / \partial \varphi$ depend on the locations and weights of the element integration points, as described in the following section.

To evaluate the conditional derivative of the basic forces in Eq. (5.3), it is necessary to differentiate Eq. (3.6) with respect to φ , which may correspond to the location or weight of an integration point. Under the assumption that the interval

of integration is held fixed, the sensitivity of the computed integration weights to φ is obtained by the differentiation of Eq. (3.6) and the subsequent solution to the linear system of equations:

$$\sum_{i=1}^{N_f} x_{fi}^{j-1} \frac{\partial w_{fi}}{\partial \varphi} = - \sum_{i=1}^{N_c} \left((j-1) x_{ci}^{j-2} \frac{\partial x_{ci}}{\partial \varphi} w_{ci} + x_{ci}^{j-1} \frac{\partial w_{ci}}{\partial \varphi} \right) - (j-1) \sum_{i=1}^{N_f} x_{fi}^{j-2} \frac{\partial x_{fi}}{\partial \varphi} w_{fi} \quad (5.4)$$

For a single parameter, φ , at most one derivative on the right-hand side of Eq. (5.4) will be non-zero. When φ corresponds to an integration point location, one of $\partial x_{ci}/\partial \varphi$ or $\partial x_{fi}/\partial \varphi$ will be equal to one and all other derivatives on the right-hand side of Eq. (5.4) will be zero. Similarly, when φ corresponds to a specified integration weight, $\partial w_{ci}/\partial \varphi$ will be equal to one while all other derivatives are equal to zero. The resulting solution of Eq. (5.4) for $\partial w_{fi}/\partial \varphi$ gives the sensitivity of the free integration weights to changes in the specified integration point locations and weights. These derivatives, along with the binary values for the derivatives of w_{ci} , x_{ci} , and x_{fi} are incorporated in Eq. (5.3) for subsequent calculation of the element response sensitivity to uncertain integration parameters.

5.2 Regularization Approaches

Recent advances in the literature regularize the strain-softening response of force-based frame elements by either modifying the constitutive parameters or scaling selected integration weights. While the former case maintains numerical accuracy for strain-hardening behavior, the regularization requires a tight coupling of the element constitutive properties and the numerical integration method. In the latter case, objectivity is maintained for strain-softening problems; however, there

is a lack of convergence for strain-hardening response. Unlike displacement-based formulations where localization occurs over the length of an entire element, strain-softening behavior causes deformations to localize at a single integration point in a force-based element.

The most common integration approach to evaluate Eqs. (3.3) and (3.4) is Gauss-Lobatto quadrature [5], which places sample points at the element ends where bending moments are largest in the absence of member loads. The order of accuracy, i.e., the highest monomial integrated exactly, for Gauss-Lobatto quadrature is $2N - 3$. Thus, to obtain the exact solution for a linear-elastic, prismatic frame element, e.g., during a patch test [142], at least three Gauss-Lobatto points are required since quadratic polynomials appear in the integrand of Eq. (3.3) in this case. A unique solution is obtained for strain-hardening problems by increasing the number of integration points in a single force-based element. Four to six points are typically sufficient to represent the spread of plasticity along an element [103].

In the presence of strain-softening section response where deformations localize at a single integration point, the solution depends on the characteristic length implied by the Gauss-Lobatto integration weights. This leads to a loss of objectivity since the force-based element response will change as a function of the number of integration points selected by the analyst. Coleman and Spacone [23] regularize the element response using a criterion of constant energy release based on the number of Gauss-Lobatto points and a characteristic length. The advantage of this approach is it does not alter the integration weights of the Gauss-Lobatto rule and thus maintains numerical accuracy for strain-hardening response. However, the main drawback is the regularization ties the section material model to the element integration method, leading to a loss of objectivity of the section response.

5.2.1 Regularization Based on Scaling Integration Weights

An alternative force-based element regularization method is to scale the element integration weights to match prescribed characteristic lengths. This approach is based on dividing an element in to three regions (one plastic hinge region at each end and one interior region) then applying separate integration rules over each region.

Addessi and Ciampi [6] use Gauss-Lobatto integration over each region, e.g., a two-point rule over the plastic hinge regions and a three-point rule over the interior. To regularize the element response, the integration rules over the plastic hinge regions are scaled by a factor of two in order to make the integration weights at the element ends equal to the characteristic lengths, l_{pI} and l_{pJ} , specified by the analyst. As shown in Fig. 5.1 (a), the integration point locations are

$$x = \{0, 2l_{pI}, 2l_{pI}, L_{int}/2, L - 2l_{pJ}, L - 2l_{pJ}, L\} \quad (5.5)$$

and associated weights are

$$w = \{l_{pI}, l_{pI}, L_{int}/6, 2L_{int}/3, L_{int}/6, l_{pJ}, l_{pJ}\} \quad (5.6)$$

where $L_{int} = L - 2l_{pI} - 2l_{pJ}$ is the length of the element interior. It is noted that the coincident Gauss-Lobatto integration points in Eq. (5.5), and their corresponding weights in Eq. (5.6), at the interfaces between the plastic hinge regions and the element interior can be combined in order to reduce the number of sample points. Addessi and Ciampi [6] also propose three-point Gauss-Lobatto integration over the plastic hinge regions, in which case quadratic polynomials are represented

exactly over the entire element length.

Scott and Fenves [129] apply two-point Gauss-Radau quadrature [5] over the plastic hinge regions and scale the integration weights by four in order to regularize the element response. In this case, the length of the element interior is $L_{int} = L - 4l_{pI} - 4l_{pJ}$, over which two-point Gauss-Legendre quadrature is applied, giving the following integration point locations

$$x = \{0, 8l_{pI}/3, x_3, x_4, L - 8l_{pJ}/3, L\} \quad (5.7)$$

where $x_{3(4)} = 4l_{pI} + L_{int}(\pm 1/\sqrt{3} + 1)/2$. The associated weights are

$$w = \{l_{pI}, 3l_{pI}, L_{int}/2, L_{int}/2, 3l_{pJ}, l_{pJ}\} \quad (5.8)$$

The mixture of Gauss-Radau and Gauss-Legendre quadrature ensures a sufficient level of integration accuracy while placing sample points at the element ends. The locations and weights of the integration points for this approach are shown in Fig. 5.1 (b).

The numerical behavior of regularization methods based on scaling integration weights is demonstrated via the moment-rotation response of a simply-supported beam under anti-symmetric bending. As shown in Fig. 5.2, the section moment-curvature relationship is bilinear with hardening ratio α . To investigate strain-hardening section behavior, α is set equal to 0.02; while this parameter is set to -0.02 in order to produce localized response at the element ends. The characteristic plastic hinge lengths are $l_{pI} = l_{pJ} = 0.15L$.

The solutions obtained by using the integration points and weights in Equations (5.5)-(5.6) and (5.7)-(5.8) are shown in Fig. 5.3 and compared to that ob-

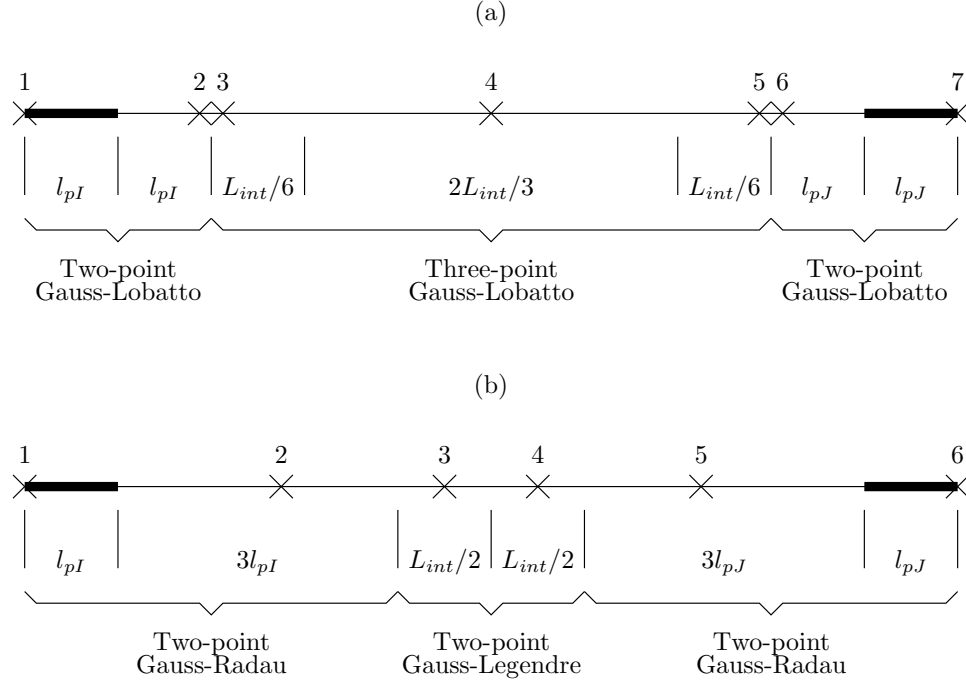


Figure 5.1: Force-based element regularization methods based on scaling integration weights in the plastic hinge regions: (a) Gauss-Lobatto over the plastic hinge and interior regions; and (b) Gauss-Radau in the plastic hinge regions and Gauss-Legendre over the interior.

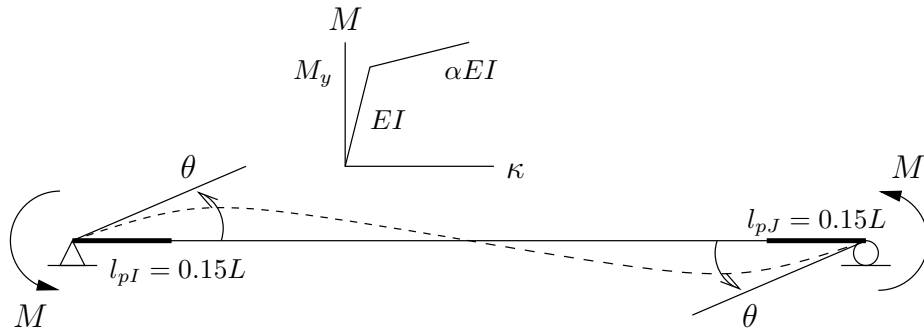


Figure 5.2: Simply-supported beam in a state of anti-symmetric bending and with a bilinear moment-curvature relationship.

tained for a non-regularized five-point Gauss-Lobatto rule applied over the element length. For strain-softening behavior that causes localization at the element ends, both regularized integration methods unload at an identical rate, as shown in Fig. 5.3 (b). The beam unloads at a higher rate for five-point Gauss-Lobatto integration since the implied characteristic length is $0.05L$. On the other hand, five-point Gauss-Lobatto integration gives the best solution for strain-hardening behavior (Fig. 5.3 (a)), while the post-yield response of the regularized methods is too flexible compared to the exact solution. This example demonstrates the need to find a single integration method that can accommodate both strain-softening and strain-hardening behavior. To arrive at such a solution, it is worth turning attention to a regularization approach based on interpolatory quadrature.

5.2.2 Regularization Based on Interpolatory Quadrature

An equivalent approach to regularize the element response is to set the integration weights at the element ends equal to characteristic values then solve a system of equations for the remaining integration point locations and weights to ensure numerical accuracy. In the case where all integration point locations and weights are unknown over the interval $[a, b]$ except for end points of weight l_{pI} and l_{pJ} , there are $2N - 4$ unknown locations and weights of $N - 2$ integration points. These unknowns can be found by solving the following system of equations

$$\sum_{i=2}^{N-1} x_i^j w_i + a^j l_{pI} + b^j l_{pJ} - \frac{b^{j+1} - a^{j+1}}{j+1} = 0 \quad j = 0, 1, \dots, 2N - 5 \quad (5.9)$$

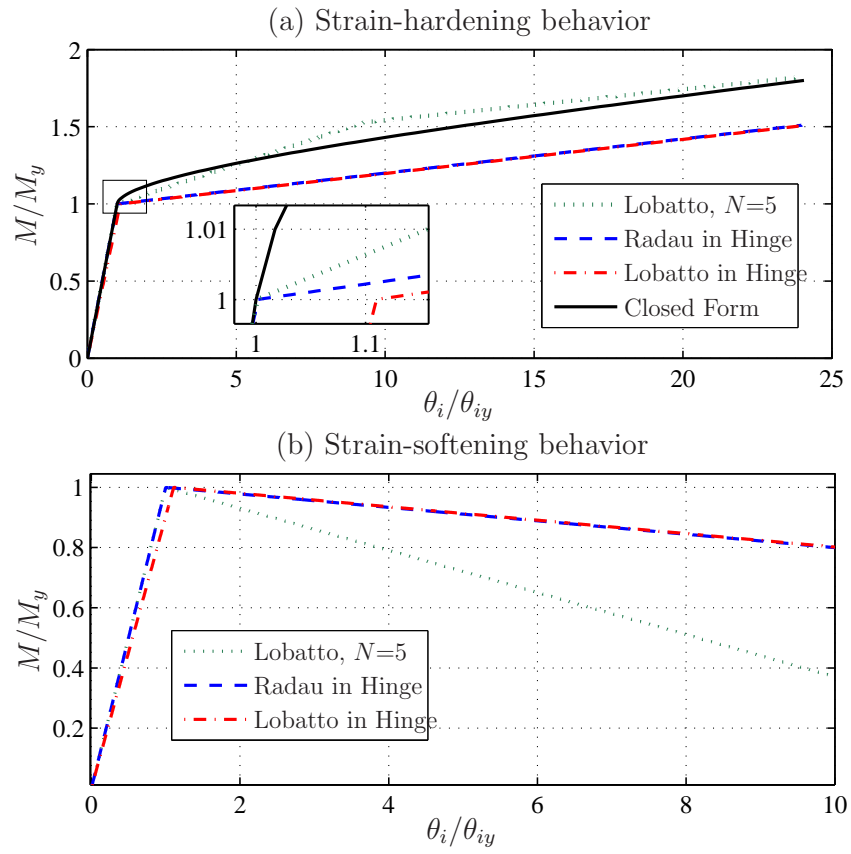


Figure 5.3: Computed moment-rotation relationship of regularization methods based on scaling integration weights compared with standard five-point Gauss-Lobatto rule for (a) strain-hardening and (b) strain-softening section behavior.

The most common choice to solve Eq. (5.9) is Newton's method [136]; however, its convergence is highly dependent on the initial guess for the unknown locations and weights. The resulting quadrature rule has an order of accuracy of $2N - 5$; thus, at least four integration points (two interior points in addition to the two end points) are required to ensure the element passes a patch test. In the absence of constraints on the end weights, the solution to Eq. (5.9) gives the Gauss-Lobatto locations and weights with accuracy $2N - 3$; while in the absence of any constraints on the locations and weights of the integration points, the solution gives Gauss-Legendre quadrature of accuracy $2N - 1$.

Interpolatory quadrature, where the locations of all the integration points are fixed, gives a more stable solution procedure, albeit with a lower order of accuracy. Specifying all N integration point locations, in addition to setting the integration weights at the element ends to l_{pI} and l_{pJ} reduces the order of accuracy to $N - 3$ and turns Eq. (5.9) into a linear system of $N - 2$ equations for the unknown weights

$$\begin{bmatrix} 1 & 1 & \dots & 1 \\ x_2 & x_3 & \dots & x_{N-1} \\ \vdots & \vdots & & \vdots \\ x_2^{N-3} & x_3^{N-3} & \dots & x_{N-1}^{N-3} \end{bmatrix} \begin{bmatrix} w_2 \\ w_3 \\ \vdots \\ w_{N-1} \end{bmatrix} = \begin{bmatrix} b - a - l_{pI} - l_{pJ} \\ (b^2 - a^2)/2 - al_{pI} - bl_{pJ} \\ \vdots \\ (b^{N-2} - a^{N-2})/(N - 2) - a^{N-3}l_{pI} - b^{N-3}l_{pJ} \end{bmatrix} \quad (5.10)$$

To integrate quadratic polynomials exactly, at least five integration points (three interior points plus two end points) must be used. To prevent poor conditioning of

the Vandermonde matrix in Eq. (5.10), the integration point locations should be well-spaced and symmetric on the interval of integration and the order of integration, N , should be kept low [46]. Better conditioning for interpolatory quadrature rules can be obtained using least squares theory [53].

While the solutions provided by Eqs. (5.9) and (5.10) regularize the element response for strain-softening section behavior, they suffer from the same shortcomings for strain-hardening behavior as the methods based on scaling integration weights and will thus lead to the same results shown in Fig. 5.3. A further modification is required in order for a single integration method to provide regularized response while maintaining a convergent solution for strain-hardening behavior.

5.2.3 Proposed Regularization Method

As seen in the foregoing discussion, regularizing force-based element response for strain-softening behavior comes at the price of losing numerical accuracy when simulating strain-hardening behavior. This forces an analyst to decide *a priori* which integration method to use when modeling frame structures with force-based finite elements. For simulations such as reinforced concrete columns with heavy axial loads using fiber models, the answer may not be clear.

To avoid complicated phenomenological rules that couple the integration rule to the section constitutive model, a standard quadrature rule is modified with two additional integration points. These points are placed small distances, ξ_I and ξ_J , from the element ends, as shown in Fig. 5.4(a).

$$x = \{(x_1 = 0), \xi_I, x_2, \dots, x_{N-1}, L - \xi_J, (x_N = L)\} \quad (5.11)$$

From this juxtaposition of integration points, the element response is regularized by setting the weights of the integration points at the element ends equal to l_{pI} and l_{pJ} , as was the case in the previous regularization methods. Then, the weights of the integration points at ξ_I and $L - \xi_J$ are set equal to $w_1 - l_{pI}$ and $w_N - l_{pJ}$, respectively, where w_1 and w_N are the end weights of the standard quadrature rule.

$$w = \{l_{pI}, w_1 - l_{pI}, w_2, \dots, w_{N-1}, w_N - l_{pJ}, l_{pJ}\} \quad (5.12)$$

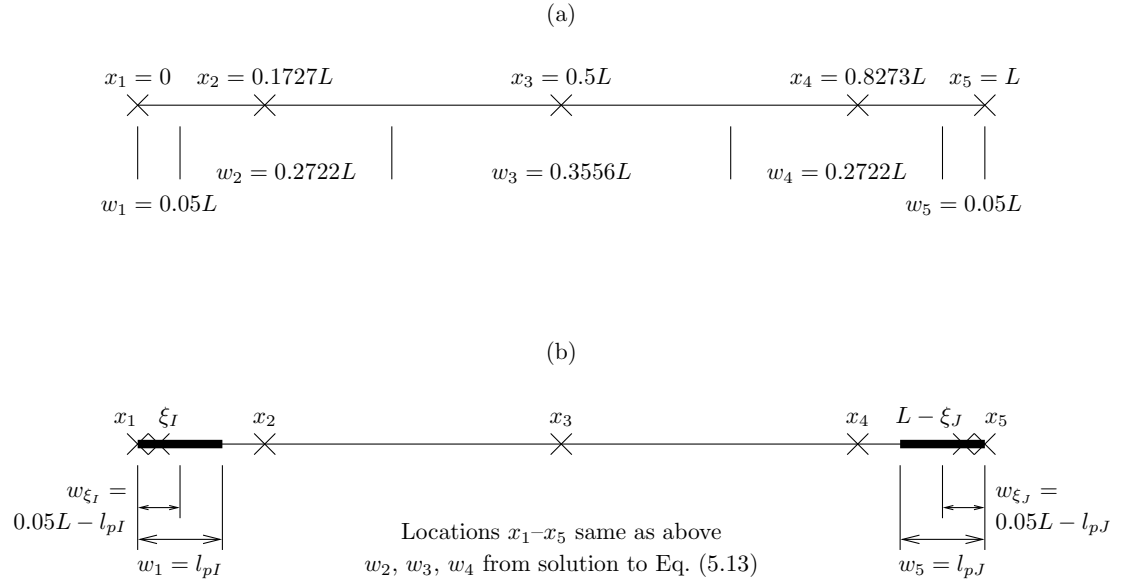


Figure 5.4: (a) Standard five-point Gauss-Lobatto integration rule; (b) Five-point Gauss-Lobatto rule regularized by addition of two integration points just inside the element ends.

This arrangement of integration points at the element ends, demonstrated in Fig. 5.4 (b) for a standard five-point Gauss-Lobatto rule, ensures a convergent strain-hardening solution is maintained; however, manipulating the locations and weights of the integration points will compromise the accuracy of the underlying

Gauss-Lobatto quadrature rule. Only constant polynomials can be represented exactly since the sum of the integration weights in Eq. (5.12) remains equal to the element length. For frame analysis; however, quadratic polynomials must be represented exactly in order to capture the exact solution for a linear-elastic, prismatic element. To this end, the integration weights of the element interior can be re-computed using interpolatory quadrature in order to ensure a sufficient level of accuracy for structural engineering applications.

$$\begin{bmatrix} 1 & 1 & \dots & 1 \\ x_2 & x_3 & \dots & x_{N-1} \\ \vdots & \vdots & & \vdots \\ x_2^{N-3} & x_3^{N-3} & \dots & x_{N-1}^{N-3} \end{bmatrix} \begin{bmatrix} w_2 \\ w_3 \\ \vdots \\ w_{N-1} \end{bmatrix} = \begin{bmatrix} L - w_1 - w_N \\ L^2/2 - Ll_{pJ} - \xi_I(w_1 - l_{pI}) - (L - \xi_J)(w_N - l_{pJ}) \\ \vdots \\ \frac{L^{N-2}}{N-2} - L^{N-3}l_{pJ} - \xi_I^{N-3}(w_1 - l_{pI}) - (L - \xi_J)^{N-3}(w_N - l_{pJ}) \end{bmatrix} \quad (5.13)$$

For an underlying N -point Gauss-Lobatto rule, the order of accuracy will be reduced from $2N-3$ to $N-3$ after re-computing the integration weights. As a result, there must be at least five integration points of the underlying quadrature method in order for the regularized integration rule to capture the exact solution for a linear-elastic, prismatic element. The underlying quadrature method can provide as few as three integration points while maintaining the exact linear-elastic solution if the constraints on $(w_1 - l_{pI})$ and $(w_N - l_{pJ})$ are removed; however, using this few integration points will lead to a poor representation of the spread of plasticity in strain-hardening problems.

It is emphasized that the proposed regularization method is not restricted to an underlying Gauss-Lobatto quadrature rule. Any N point quadrature method can be used, including Newton-Cotes, which spaces integration points equally along the element [5]. In fact, N arbitrarily located integration points can be used; however, this may lead to ill-conditioning of the Vandermonde equations used for interpolatory quadrature. The only restriction is that the underlying quadrature rule place integration points at the element ends.

Condition Number

An additional consideration in constructing numerical integration rules is the condition number [47, 42], which is the sum of the absolute values of the integration weights:

$$K = \sum_{i=1}^N |w_i| \quad (5.14)$$

For beam-column elements, a well-conditioned quadrature rule has a condition number equal to the element length, L . However, for the regularized integration method described in this paper, negative integration weights will appear when $l_{pI} > w_1$ or $l_{pJ} > w_N$. When it is the case that there are negative weights at each end of the element, it can be shown that the condition number of the regularized integration method is

$$K = 2(l_{pI} - w_1) + 2(l_{pJ} - w_N) + \tilde{K} \quad (5.15)$$

where \tilde{K} is the condition number of the underlying quadrature rule. For values of l_{pI} and l_{pJ} that satisfy $l_{pI} + l_{pJ} < L$, the condition number of the proposed regular-

ization method remains bounded by $2L + \tilde{K}$. Thus, for an underlying quadrature rule that is well-conditioned, which is guaranteed for Gauss-Lobatto quadrature with any value of N and Newton-Cotes quadrature for any N except odd values greater than or equal to nine [5], the proposed method will be numerically stable.

This arrangement of integration points at the element ends ensures a convergent strain-hardening solution is maintained; however, manipulating the locations and weights of the integration points will compromise the accuracy of the underlying Gauss-Lobatto quadrature rule. To validate the proposed regularization method, the static, cyclic response of two reinforced concrete specimens is simulated.

The most significant source of uncertainty in the proposed regularization method is the values of the parameters lp and ξ at both ends. For strain-hardening problems, these parameters should be relatively small in order to maintain the convergent behavior offered by the underlying quadrature method. The effect of increasing ξ for the strain-hardening example will be demonstrated in a numerical example that covers seismic reliability analysis of bridge pier columns.

5.2.4 Software Design of Regularized Integration Method

The implementation of the proposed regularization technique to OpenSees need a software design strategy providing the user ability to apply the method on any N point underlying quadrature. To emphasize the loose coupling of the proposed regularization method from both the underlying quadrature method and the element constitutive behavior, a UML diagram of its implementation in an object-oriented finite element framework is shown in Fig. 5.5. The force-based frame element state determination is encapsulated in a class that contains N instances of

a section force-deformation object and one instance of a beam integration object. This implementation follows the *Strategy* design pattern of offering an object interchangeable algorithms to define its behavior [41, 130]. The proposed regularization method is implemented by recursive composition of an object of the same type but different class, e.g., using an implementation of a Gauss-Lobatto or Newton-Cotes quadrature rule. The encapsulation of the regularized integration method in an object separate from the element makes the proposed method applicable to the wide range of force-based element state determination algorithms available in the literature [134, 116, 103, 80].

5.3 Regularized Integration Verifications

To verify the proposed regularization method is mathematically correct, the response of the simply-supported beam in Fig. 5.2 is demonstrated with a five-point Gauss-Lobatto rule regularized with parameters $\xi_I = \xi_J = 0.001L$ and $l_{pI} = l_{pJ} = 0.15L$. The location and weight of the regularized integration points are given in Fig. 5.4(b). After the solution to Eq. (5.13), the interior integration weights are $w_2 = w_4 = 0.2718L$ and $w_3 = 0.3563L$, which differ only slightly from the corresponding weights of the underlying five-point Gauss-Lobatto rule, $w_2 = w_4 = 0.2722L$ and $w_3 = 0.3556L$. This difference increases with increasing values of ξ_I and ξ_J and would be zero when these parameters are zero; however, this change in integration weights is essential to ensure the element response is correct in the linear-elastic range of response.

The moment-rotation response with the original and regularized five-point Gauss-Lobatto integration is presented in Fig. 5.6 for strain-hardening section be-

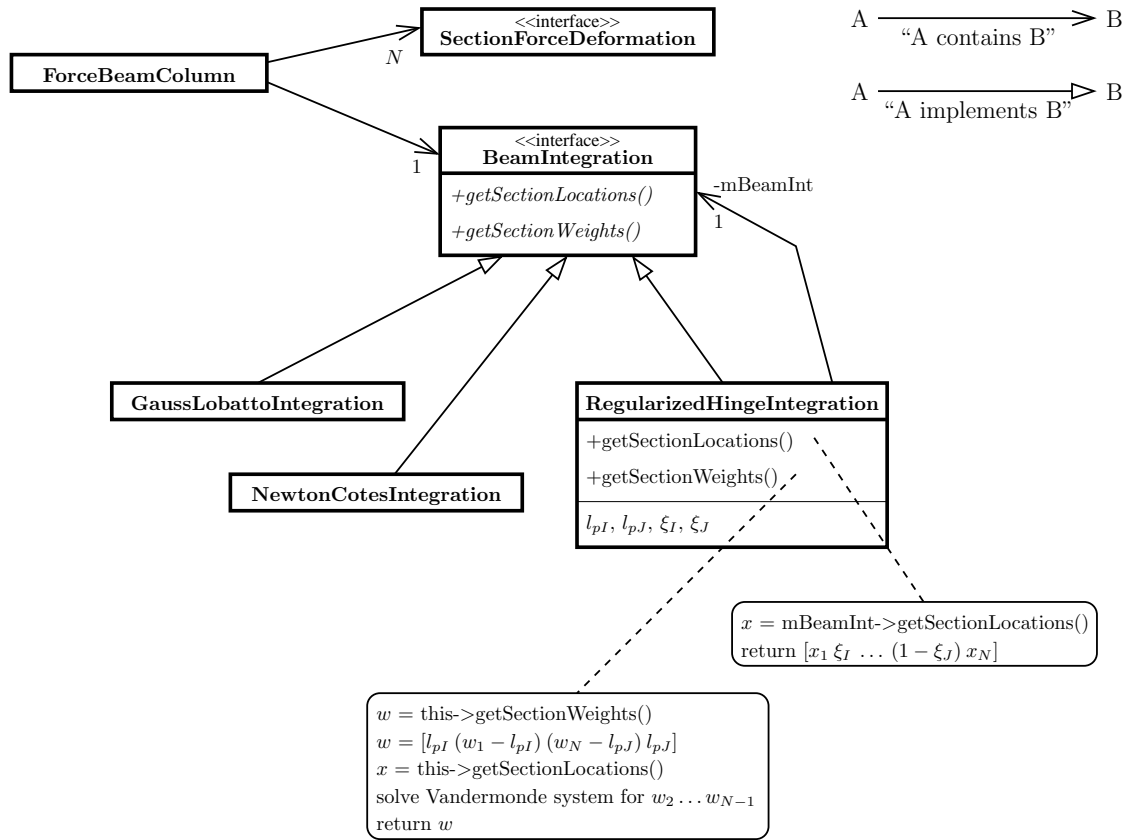


Figure 5.5: UML diagram for implementation of proposed regularization method in an object-oriented finite element framework.

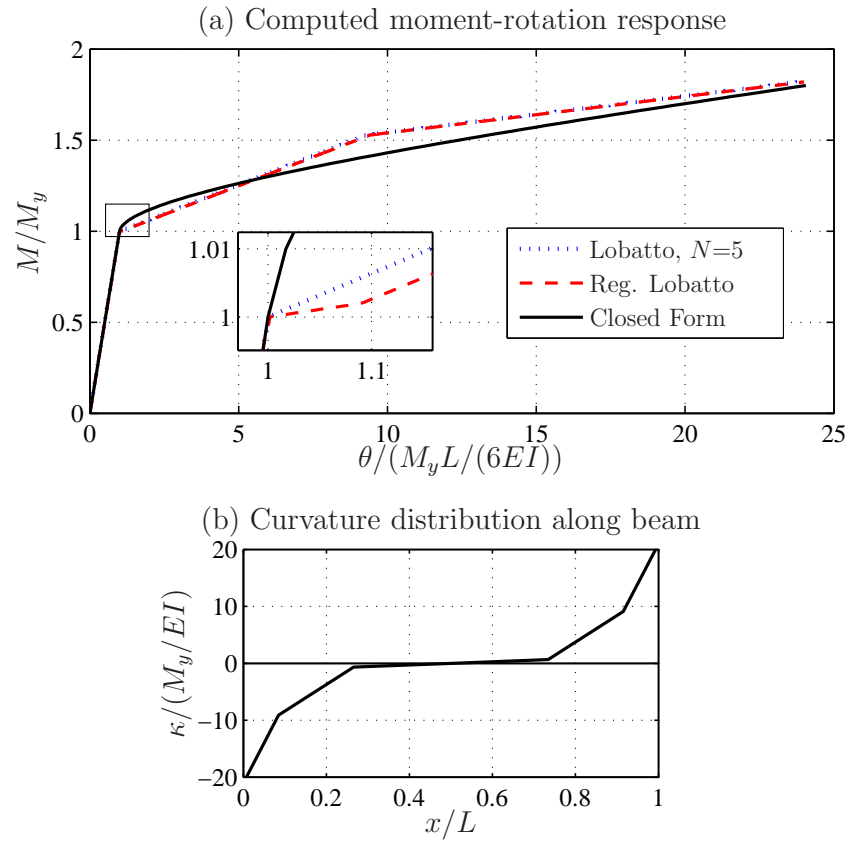


Figure 5.6: Comparison of beam response between standard and regularized five-point Gauss-Lobatto for strain-hardening section behavior.

havior. As shown in Fig. 5.6 (a), there is a slight difference between the response computed with the regularized and non-regularized integration rules. This discrepancy occurs as yielding spreads over distances ξ_I and ξ_J at the element ends. After these integration points plastify, the regularized solution returns to that obtained by the unmodified Gauss-Lobatto rule. Thus, the proposed regularization method maintains a convergent solution for strain-hardening problems. This was not possible using the previous regularization methods [6, 129].

For the case of localization at the element ends due to strain-softening section behavior, Fig. 5.7 (a) shows the regularized five-point Gauss-Lobatto rule unloads at an identical rate to the solution obtained by scaling Gauss-Radau integration weights in the plastic hinge regions [129]. In addition, the response of the unmodified five-point Gauss-Lobatto rule is repeated in Fig. 5.7 (a) for comparison. This idealized example shows the proposed regularization method is suitable for simulating both strain-hardening and strain-softening section response. Comparisons with published experimental data in the following section will show the method is applicable to simulating the response of reinforced concrete structural members.

5.3.1 Sensitivity of ξ Parameters

The most significant source of uncertainty in the proposed regularization method is the values of the parameters ξ_I and ξ_J . For strain-hardening problems, these parameters should be relatively small in order to maintain the convergent behavior offered by the underlying quadrature method. The effect of increasing ξ_I and ξ_J for the strain-hardening example is demonstrated in Fig. 5.8. The computed solution deviates slightly from the standard Gauss-Lobatto solution when $\xi_I = \xi_J = 0.01L$;

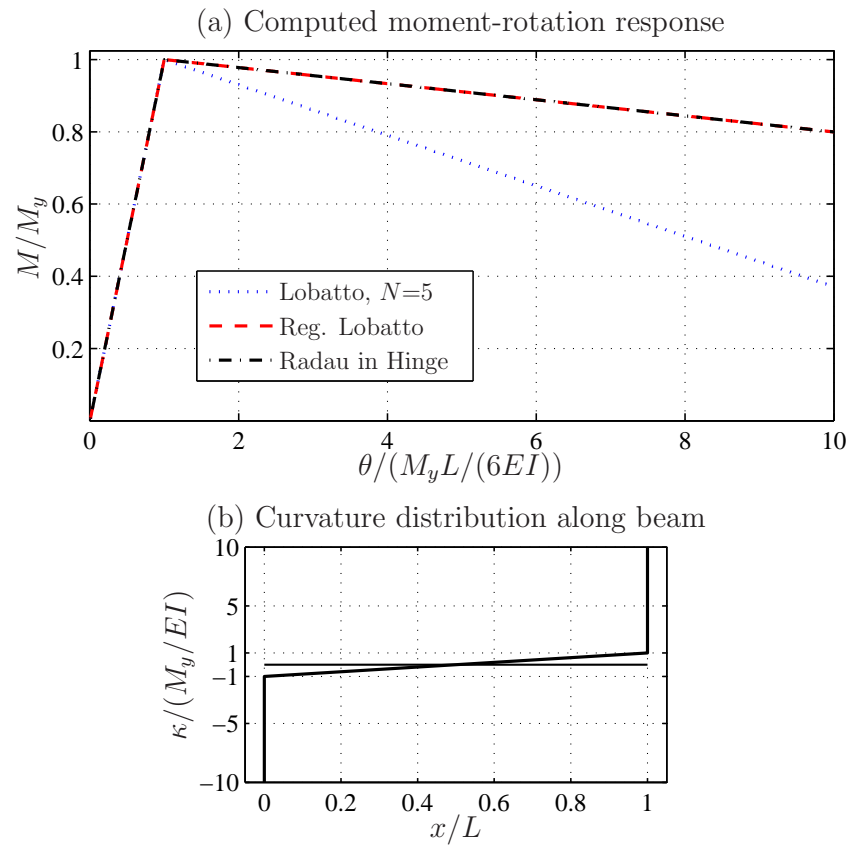


Figure 5.7: Comparison of beam response between standard and regularized five-point Gauss-Lobatto for strain-softening section behavior.

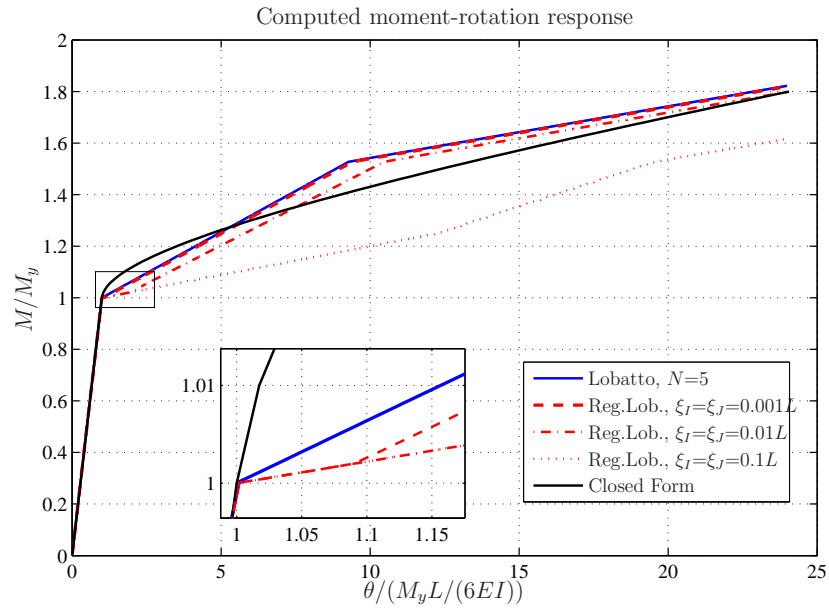


Figure 5.8: Sensitivity of beam response for increasing values of parameters ξ_I and ξ_J for regularized five-point Gauss-Lobatto integration and strain-hardening section behavior.

however, there is a large error for $\xi_I = \xi_J = 0.1L$, which places the additional integration points outside the $0.05L$ region associated with the end points of the underlying five-point Gauss-Lobatto rule.

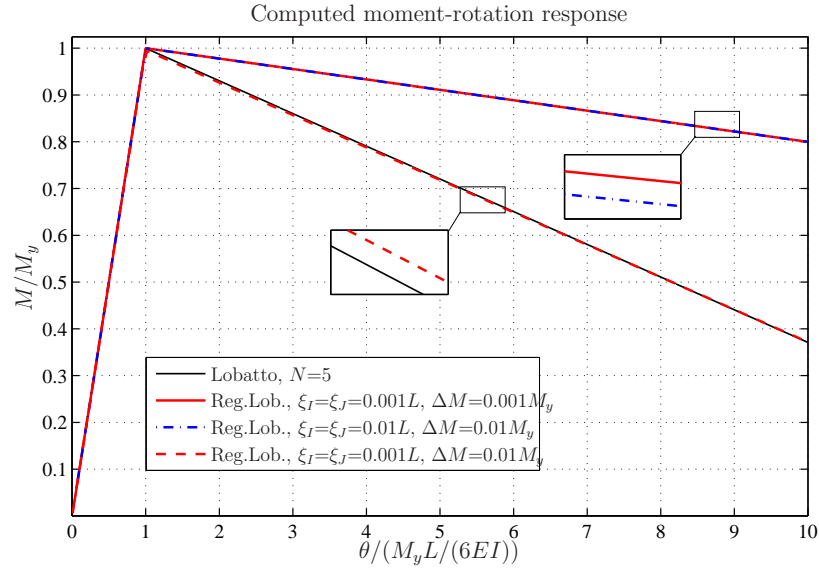


Figure 5.9: Sensitivity of beam response for various combinations of parameters ξ_I and ξ_J and load steps for regularized five-point Gauss-Lobatto integration and strain-softening section behavior.

On the other hand, for strain-softening problems, the ξ_I and ξ_J parameters should be large enough to ensure that localization only occurs at the element ends under discrete load steps. For large load steps and small values of ξ_I and ξ_J , it is possible for these additional integration points to yield simultaneously with the integration points at the element ends. This simultaneous yielding is demonstrated in Fig. 5.9 for relatively small integration parameters $\xi_I = \xi_J = 0.001L$ and the larger load step values of $\Delta M = 0.01M_y$. It is noted that the likelihood of simultaneous yielding is reduced for more complex constitutive models, e.g., the reinforced

concrete fiber sections presented in the following example, where the stiffnesses of the adjacent sections at the element ends differ due to axial-moment interaction.

Based on numerous simulations conducted by the authors, values of ξ_I and ξ_J equal to $0.1w_1$ and $0.1w_N$, respectively, are ideal for the regularization method to detect the correct behavior for a wide range of constitutive behavior and load increments. The weights w_1 and w_N represent the end weights of the underlying quadrature rule, e.g., for the five-point Gauss-Lobatto rule with end weights $w_1 = w_N = 0.05L$, the optimal parameter values are $\xi_I = \xi_J = 0.005L$.

5.3.2 Reinforced Concrete Columns With Hardening and Softening Behavior

To validate the proposed regularization method, the static, cyclic response of two reinforced concrete specimens is simulated. The response of each specimen is computed using a single force-based element with a regularized five-point Gauss-Lobatto rule with $\xi_I = \xi_J = 0.005L$. The plastic hinge lengths are determined from the individual specimen properties. The numerical examples are performed in the OpenSees (Open System for Earthquake Engineering Simulation) software framework developed as the computational platform for research in performance-based earthquake engineering at the Pacific Earthquake Engineering Research Center (PEER) [93].

5.3.2.1 Strain-Hardening

A spirally reinforced concrete column, specimen 430 in the tests of Lehman and Moehle [78], is modeled to demonstrate the accuracy of the regularized integration method under strain-hardening behavior. The reinforcing details of the column are shown in Fig. 5.10 and a fiber discretization of the cross-section is used to compute the section stress resultants and account for axial-moment interaction. The stress-strain behavior of concrete fibers is modeled by a parabolic ascending branch and linear descending branch in compression [70]. The concrete compressive strength is $f'_c=31$ MPa. Confining effects of transverse reinforcement are estimated using the Mander model [87]. Using this model, the confined concrete has a compressive strength of $f'_{cc}=43.4$ MPa reached at a strain of $\varepsilon_{cc}=0.006$, and ultimate strain $\varepsilon_{ccu}=0.028$. The reinforcing steel is modeled using the Giuffre-Menegotto-Pinto constitutive model [95]. The elastic modulus, yield stress, and hardening ratio of the steel are assumed to $E=200000$ MPa, $f_y=462$ MPa, and $\alpha=0.01$. The compressive axial load applied to the specimen is 7.2% of the axial capacity, $f'_c A_g$, a relatively light axial load. For the plastic hinge length, an experimentally validated empirical formula that takes in to account the effects of bar pullout and strain penetration [115] is used

$$l_p = 0.08L + 0.022f_y d_b (MPa, mm) \quad (5.16)$$

where L , f_y and d_b are the member length, steel yield stress and bar diameter, respectively. Using the column properties, the plastic hinge length is equal to $0.15L$ according to Eq. (5.16). In using this equation to determine the plastic hinge length, it is implicitly assumed that if localization occurs, the region of

fracture will be large compared to the individual cracks that contribute to the overall energy dissipation.

The computed load-displacement response of the column is shown in Fig. 5.11 (a) and Fig. 5.11 (b) for standard and regularized five-point Gauss-Lobatto integration, respectively. As seen in the figures, the methods give nearly identical results as yielding spreads from the base of the column under the light axial load. Further evidence of the strong agreement between the standard and regularized integration methods is shown in Fig. 5.11 (c) with the moment-curvature response at the base. The results of this example show the regularized method is able to find a unique solution for strain-hardening cyclic response without any spurious behavior arising from the negative integration weight a small distance from the base of the column.

5.3.2.2 Strain-Softening

The reinforced concrete column, specimen BG-8 in the tests of Saatcioglu and Grira [128], is analyzed in this example. The geometry and reinforcing details of the column are given in Fig. 5.12. As in the previous example, a fiber discretization of the cross-section accounts for axial moment-interaction. The same constitutive models for the steel and concrete stress-strain relationships are used in this example. In this case, the concrete compressive strength is $f'_c=34$ MPa. In the core region, f'_{cc} is 49.3 MPa due to confining effects of the transverse steel. The strain at the ultimate strength and the ultimate strain of core concrete are $\varepsilon_{cc}=0.007$ and $\varepsilon_{ccu}=0.029$, respectively. For the steel reinforcement, the elastic modulus is $E=200000$ MPa, yield stress is $f_y=455.6$ MPa, and hardening ratio is $\alpha=0.01$. A



Figure 5.10: Dimensions of specimen 430 in the test of Lehman and Moehle [78].

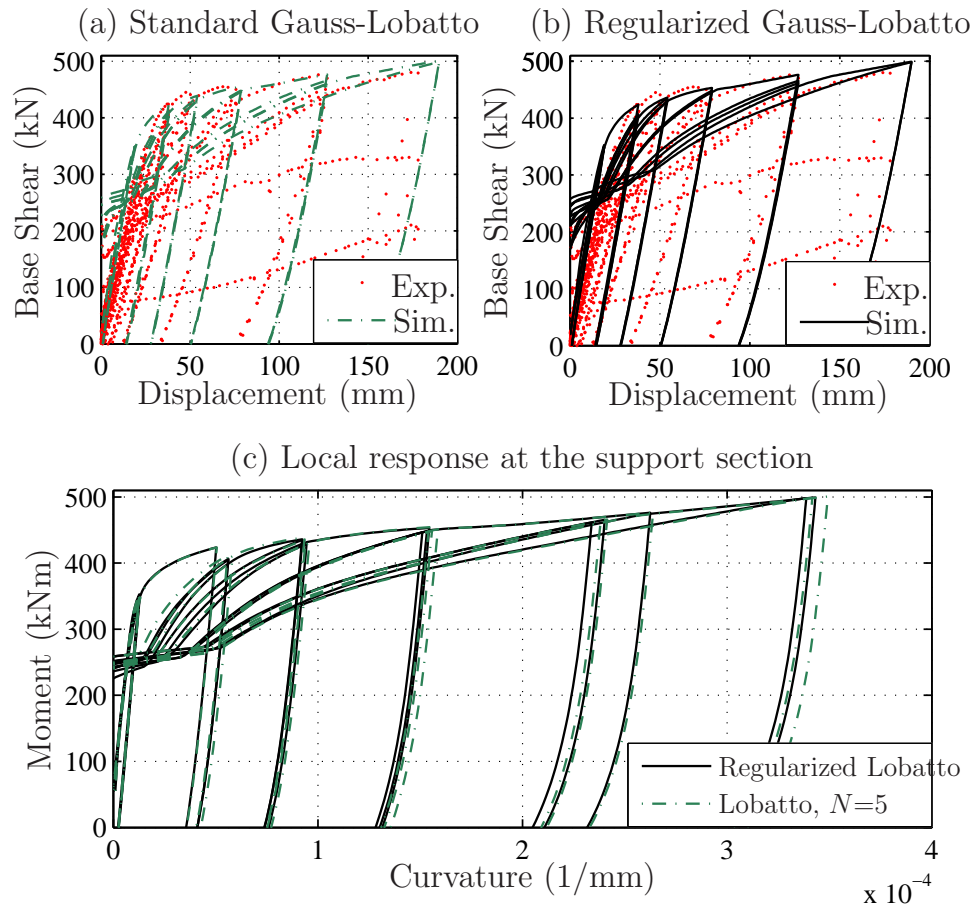


Figure 5.11: Computed global response and local moment-curvature relation at the support section of specimen 430.

relatively large compressive axial load, $P=0.231f'_cA_g$, is applied to the specimen. Using Eq. (5.16), the plastic hinge length is calculated as $l_p = 0.20L$.

The global response of the member using standard and regularized five-point Gauss-Lobatto are given in Fig. 5.13(a) and Fig. 5.13(b), respectively. As seen in the figures, the cyclic response envelope of the cantilever with the regularized integration matches the test data for strain-softening behavior. On the other hand, using standard integration, there is a significant discrepancy in the base shear envelope after the plastic hinge forms and damage localizes. Since the numerical solution is obtained by displacement control of the cantilever free end, the computed moment-curvature response in Fig. 5.13 (c) shows the increased demands imposed at the fixed end as the response localizes over the small plastic hinge length, $0.05L$, implied by the standard five-point Gauss-Lobatto integration. Upon inspection of the computed results, it is noted that the negative integration weight just above the column base does not lead to spurious behavior during cyclic loading with strain-softening section response.

5.4 Reliability Analysis of Bridge Column with Regularized Method

Numerical examples on the one degree indeterminate beam shown in Fig. 5.14 demonstrate the essential features of analytic response sensitivity for interpolatory quadrature in force-based elements. The first example verifies that the sensitivity equations are correct via comparison with finite difference computations. This is followed by an example highlighting the differences in sensitivity to regularization parameters for strain-hardening and strain-softening behavior. The final example shows the efficiency of the analytic derivatives in a first-order reliability analy-

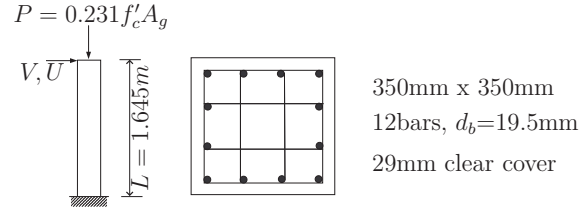


Figure 5.12: Dimensions of specimen BG-8 in the tests of Saatcioglu and Grira [128]

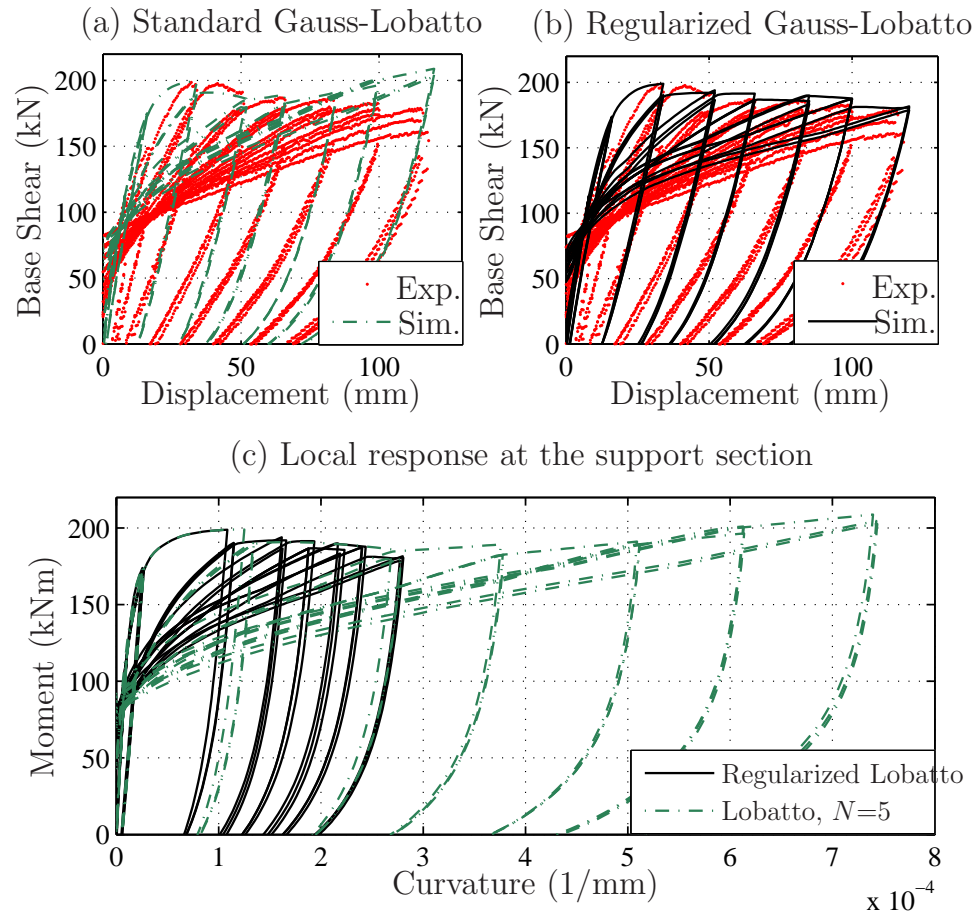


Figure 5.13: Computed global response and local moment-curvature relation at the support section of specimen BG-8.

sis, as well as demonstrating the importance of integration parameters on system reliability.

5.4.1 Verification of DDM Equations

The five-point regularized Gauss-Lobatto integration is applied in the element state determination, with $l_{pI} = l_{pJ} = 15.0$ and $\xi_I = \xi_J = 1.0$. The moment-curvature response at each integration point is bilinear with $\alpha=2\%$ strain-hardening. A concentrated moment is applied at the right end of the beam.

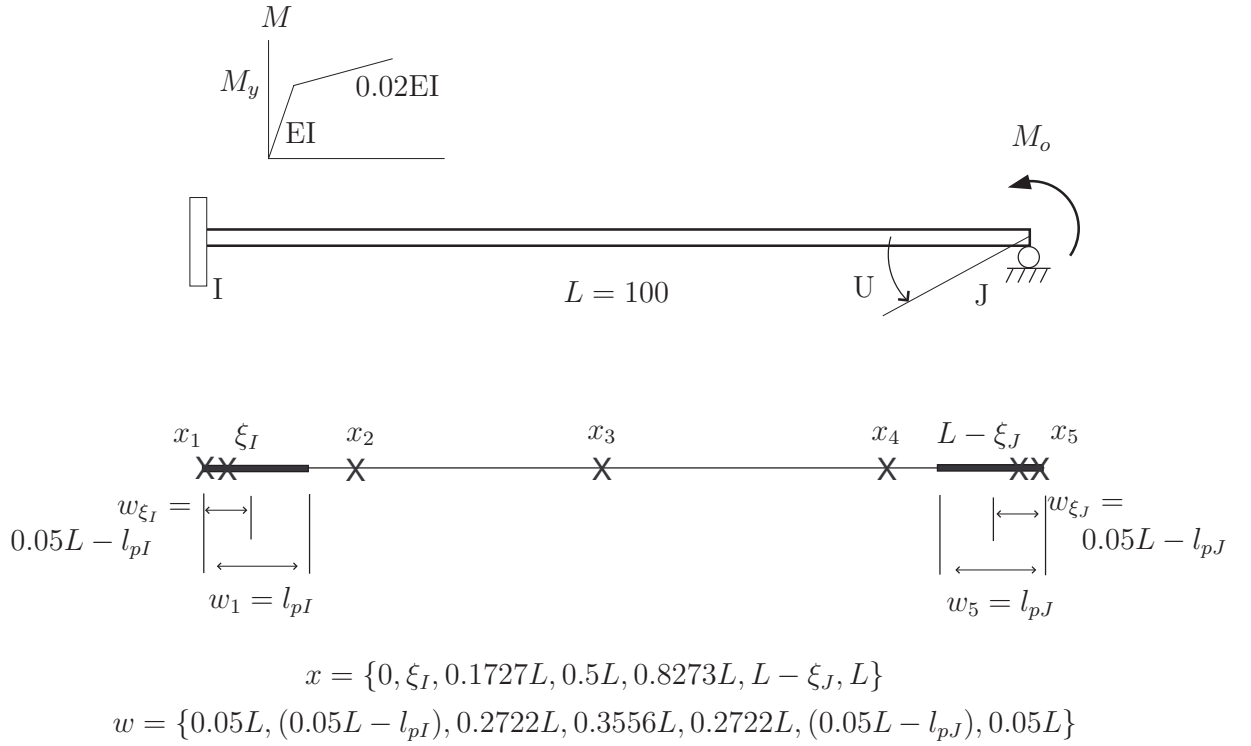


Figure 5.14: One degree indeterminate beam and the integration parameters

The sensitivity of the end rotation, U , with respect to the four integration parameters (l_{pI} , l_{pJ} , ξ_I , and ξ_J) is shown in Fig. 5.15 for monotonic increase in the applied moment to a rotation ductility (U normalized by yield value $U_y = M_y L / (4EI)$) of 20. As expected, there is zero sensitivity prior to yield at the free end of the beam. After yield, the sensitivity with respect to l_{pI} and ξ_I becomes non-zero and continues to increase until the fixed end of the beam yields and the sensitivity with respect to l_{pJ} and ξ_J becomes active. Discrete jumps in the response sensitivity occur as the constitutive model at each integration point switches from an elastic to yielding state [25]. The sensitivity of the internal bending moment at the fixed end of the beam [Fig. 5.16] shows similar trends to that for the end rotation. In both cases, the DDM results matches that obtained by finite differences with a perturbation of 0.01 times the nominal parameter value.

5.4.2 Column Reliability Example

With the DDM implementation verified, attention now turns to the difference in response sensitivity for strain-hardening and strain-softening moment-curvature response of the beam. For strain-hardening response, plasticity spreads along the beam; however, deformations localize at a single section under strain-softening response, causing the remaining portions of the beam to unload in order to maintain equilibrium.

The calculation of response sensitivity confirms that the plastic hinge length associated with the section where localized deformations occur controls the beam response under strain-softening behavior. As shown in Fig. 5.17, the sensitivity of the end rotation to l_{pJ} increases indefinitely for strain-softening behavior, as

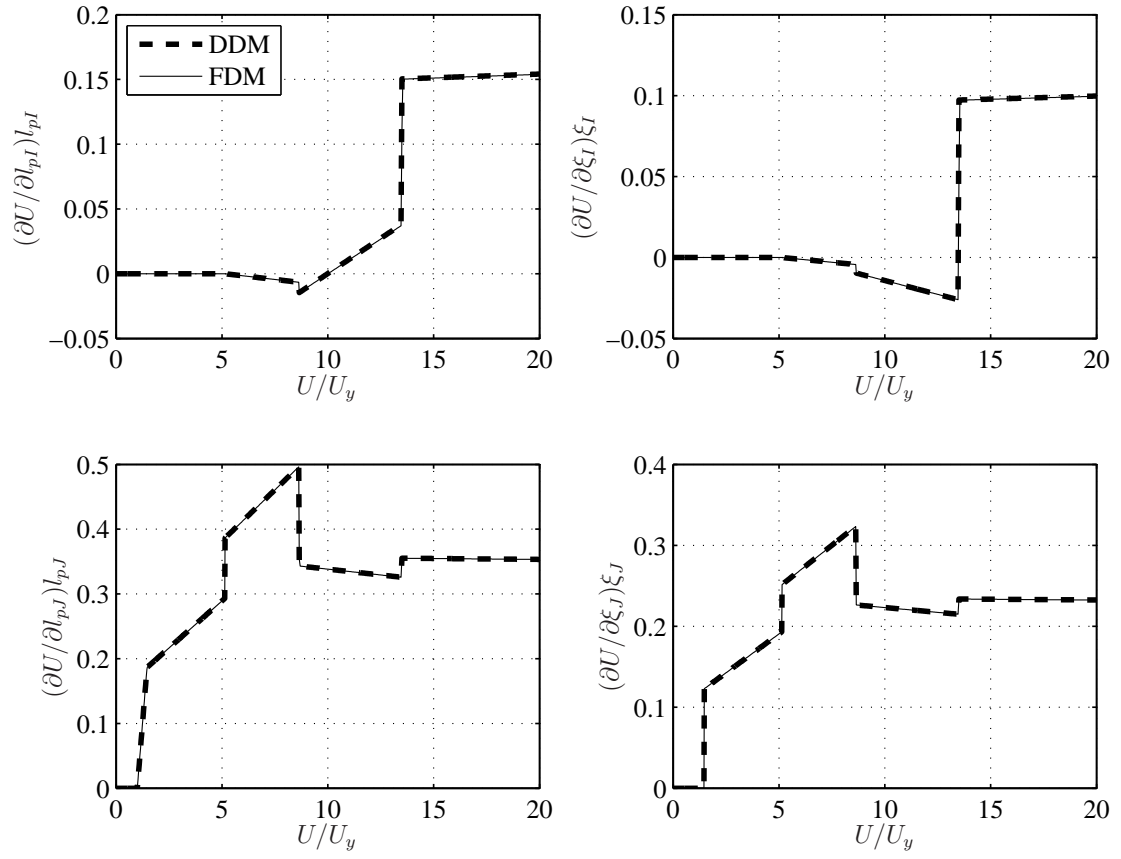


Figure 5.15: Sensitivity of end rotation to regularized integration parameters.

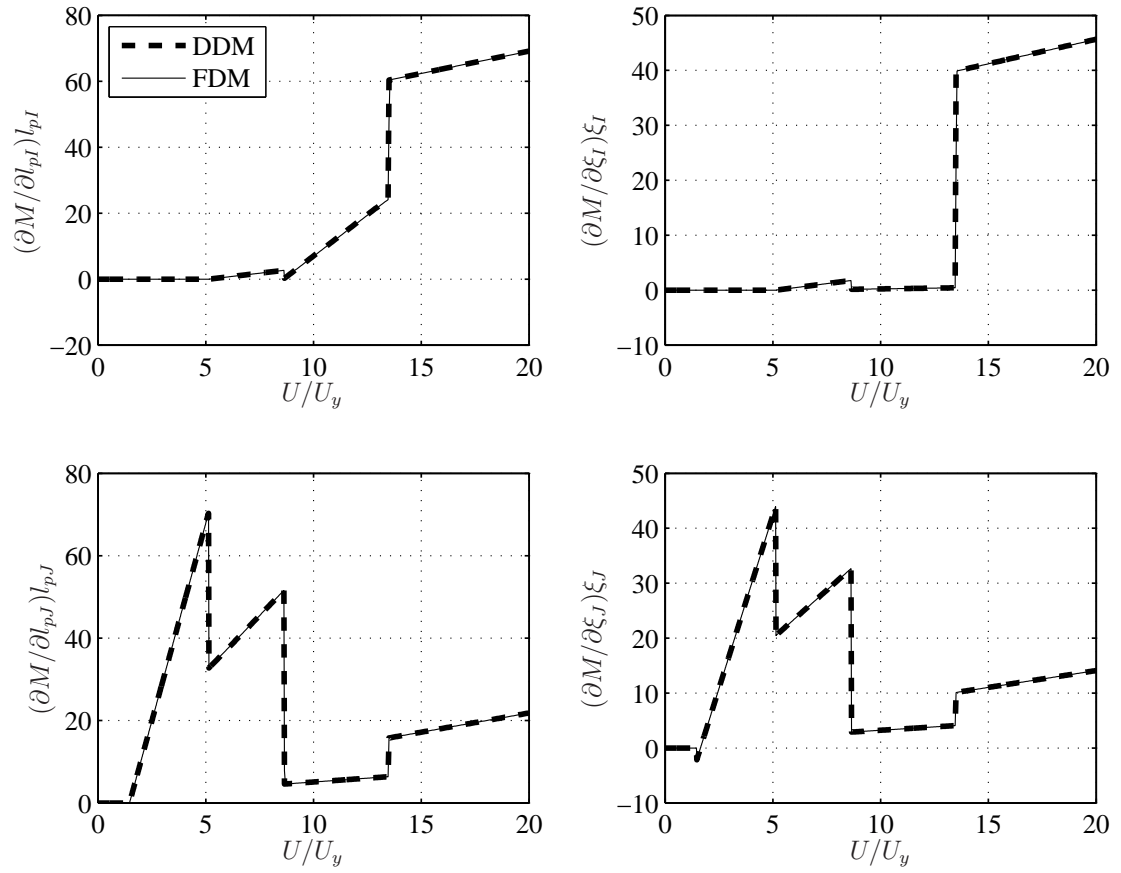


Figure 5.16: Sensitivity of reaction moment to regularized integration parameters.

compared to that for strain-hardening, which remains relatively low as yielding is able to spread across the beam and activate the sensitivity to other constitutive and integration parameters.

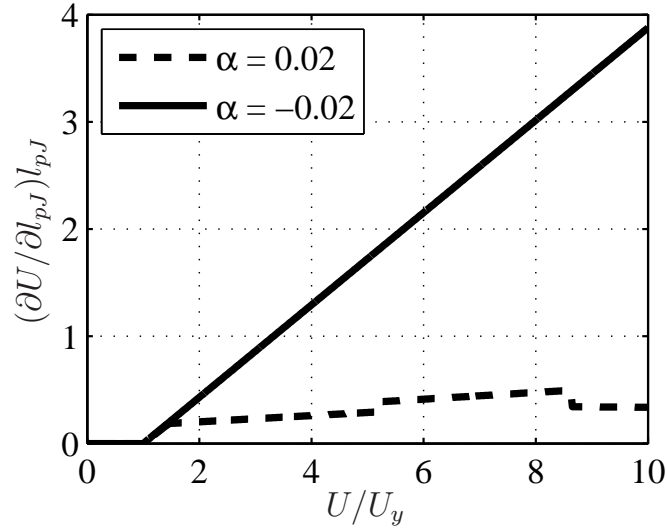


Figure 5.17: Comparison of end rotation sensitivity to plastic hinge length for strain-hardening and strain-softening behavior.

To assess the importance of the integration parameters relative to common sources of aleatory uncertainty, a first-order reliability (FORM) analysis is conducted in this example. The distribution, mean value, and coefficient of variation for each random variable are shown in Table 5.1. The plastic hinge lengths and integration parameters are each treated as pairs of correlated normal random variables, while the section yield moments at the corresponding locations are modeled as lognormal random variables with strong correlation at each end of the beam.

The performance function defines failure as the end rotation ductility exceeding

Table 5.1: Random variable distributions assigned to the uncertain parameters in reliability analysis and their values and importance measures at most probable failure point (MPP).

Parameter	Distribution	COV	Mean	Correlation	MPP	Importance
Plastic hinge length, l_{pI}	Normal	0.20	15.0	0.3	15.71	0.00039
Plastic hinge length, l_{pJ}					17.36	0.2275
Distance, ξ_I	Normal	0.20	1.0	0.3	1.005	-0.00178
Distance, ξ_J					1.020	0.02947
Yield Moment @ $x=0$	Lognormal	0.1	1000.0	0.7	943.1	-0.1632
Yield Moment @ $x=\xi_I$					960.2	0
Yield Moment @ $x=L-\xi_J$	Lognormal	0.1	1000.0	0.7	1001.0	0.5519
Yield Moment @ $x=L$					860.6	-0.7850

15 at a load of $M_o=1500$.

$$g = 15\theta_y - \theta \quad (5.17)$$

At the mean values of the random variables, the computed end rotation ductility is 10 at the specified load level. Thus, the performance function defines failure as the end rotation exceeding its nominal value by 50%. Using the DDM, the solution point is found in eight iterations to a reliability index of $\beta=2.193$, which corresponds to a 1.43% probability of failure.

The parameter values at the most probable failure point are shown in Table 5.1, along with importance measures that account for the prescribed correlation between the random variables (γ -values). The importance measures show that the yield moments at the free end of the beam have the most influence on the response at the failure point, followed by the yield moment at the beam's fixed end. Of the four integration parameters, the plastic hinge length at the free end, l_{pJ} , ranks highest in importance, while the others have relatively low importance. This quantification of uncertainty confirms the expected result that the integration pa-

rameters for the sections with the largest bending moment have the highest relative ranking.

Using analytic gradients (DDM) of the performance function to determine search directions, the FORM analysis requires 22 function evaluations to reach the solution point. On the other hand, gradients computed by finite differences require 94 function evaluations in order to converge to the same solution. Although this is a small problem for which computational cost is negligible, the reduction in function evaluations indicates the potential for significant computational savings in the finite element reliability analysis of larger systems where parameters such as plastic hinge lengths are treated as uncertain random variables.

Chapter 6 – Conclusions

FORM Analysis and Uncertainty Modeling

- The study provided a methodology for live-load finite element reliability analysis of RC bridge girders in a probabilistic software framework while treating aleatory and epistemic uncertainties simultaneously. The framework allowed analyst to use various configurations in modeling girders and combined shear-moment resistance of sections.
- A solution for bridge reliability was achieved by first-order reliability approach based on sensitivity gradients. The probability of failure due to vehicle loads was evaluated in a finite element reliability approach. The reliability index was the primary output in design and inspection procedures of bridge girders and in permit load analysis.
- As a by-product of FORM analysis, importance measures of uncertainties were obtained to distinguish parameters with respect to their influence on the failure modes. To perform accurate reliability assessments, response sensitivity was required to rank the parameters according to their importance on structural performance.
- An alternative to meshing displacement-based elements was taken in this study, where each span was considered as one force-based element where integration points coincide with critical locations of girders. It was straightforward to distribute bending moment and shear forces a coarse mesh and

link to a constitutive model while the force equilibrium was satisfied without discretization error.

- A unique contribution was the treatment of moment-shear interaction using MCFT capacity equations. The approach was to prevent non-conservative estimates of reliability when treating moment and shear separately. AASHTO-LRFD code specifications were used to calculate the capacity of the selected sections with random properties using the probabilistic model where material and geometry parameters were considered as random variables.
- To support finite element reliability analysis, analytical response sensitivities were derived with respect to uncertain material properties, girder dimensions, reinforcing details and moving loads using DDM. Consequently, the response sensitivity equations were implemented alongside the ordinary finite element response equation and computed at the same precision rate without repeated analysis. Response sensitivity modules of OpenSees to assess the reliability of bridge girders subjected to moving loads were important in computation of response gradients with respect to uncertain parameters.
- Live-load reliability analysis software provided sensitivity parameters to be treated as uncertainty. The numerical examples in this study modeled the variation of uncertainties due to measurement and fabrication errors. However, the random variables are available to modify with user-defined variation parameters so that, the Tcl scripts can command the framework to collaborate with other applications analyzing particular cases such as deterioration in material and shape, the fatigue condition and the retrofit analysis.

Finite Element Analysis with Force-Based Elements

- In finite element analysis with force-based elements, a material model comprising shear and flexural interaction was not available in OpenSees. The implementation of a fiber discretization of beam sections with coupled axial, flexural and shear deformation was a unique contribution to the analysis of bridge girders with force-based elements.
- The new material model detected the shear effect on the global behavior of the test specimens using finite element analysis with OpenSees that was not able to provide such output with current material library. Crack mapping for beam sections subjected to static loadings were available and the strain distribution along the vertical reinforcing steel was important in finite element analysis of shear dominant components.
- The definition of T-beam sections in terms of effective width and deck thickness was not available for sensitivity calculations in OpenSees. The implementation of T-beam fiber discretization and the derivation of shape sensitivity equations allowed the analyst to consider the shape parameters uncertain in reliability analysis of bridge girders.
- The Tcl scripts to program OpenSees simulated the motion of user-defined multi-axle trucks and performed a reliability analysis using proposed methodology. The framework provided moment-shear reliability indices of bridge girders and furnished a reliability assessment for special permit vehicle loads.
- While simulating the time-steps of static moving loads along the bridge component, the sensitivity modules to be implemented in the framework provided

the selected response sensitivities as a stand-alone output of finite element analysis in design procedures.

Reinforced Concrete Bridge Column Sensitivity and Reliability

- In the reliability analyses of McKenzie River Bridge girder, the reliability indices at load increments were obtained for various configurations of analysis setup. The selection of demand and resistance models caused a variation in critical reliability index. In the numerical examples, critical reliability indices converged to the same values when the biaxial and uniaxial material models were used. Uncertain moment and shear distribution factors and dynamic effects placed at highest ranks in the importance measures as well as axle weights. Albeit the mean values and variation do not affect the analysis methodology presented in the study, a further study is recommended to determine improved variations on these parameters.
- When compared to the rectangular section analysis, the T-shape provided the importance measure of two parameters b_{eff} and h_f in both resistance and finite element demand side of the performance function. However, these shape parameters were ranked significantly low. Low γ -values for these parameters indicated that the small variation of effective width and deck thickness was not influent on the design point. On the other hand the reliability index showed a variation when rectangular sections were replaced with T-shape. The difference between reliability indices with linear-elastic uniaxial and nonlinear- biaxial material models was highlighted when the contribution of deck was accounted for in the analysis.

- Variations in d and b_w were relatively small when compared to material and load parameters. Accordingly, these parameters showed lower importance in rankings. The moment- shear- controlled analysis at prismatic members converged to matching reliability indices whether the sections were modeled as rectangular or T-shape. However, the analytical sensitivity formulations allowed uncertainties in shape parameters to be quantified whether the sections were prismatic or non-prismatic in the proposed reliability software framework.
- The resistance models LC and MB were two options providing shear-moment interaction diagrams given in AASHTO-LRFD specifications. LC approach having relatively small shear strength gave conservative reliability indices for sections at shear critical locations. LC converging to the same index with MB for moment critical sections reduced the number of performance functions to evaluate in the analysis providing a continuous approximation of the capacity curve.
- MB demonstrated the general procedure of AASHTO-LRFD calculating shear-moment interaction. Simulating MCFT parameters $\beta^* - \theta^*$ for each realization of the limit state, MB provided a statistical model at the resistance side of the performance function. The five-line capacity curve was sufficient to capture critical points of MV interaction for both positive and negative bending moment.

Reinforced Concrete Bridge Column Sensitivity and Reliability

- A numerically consistent regularization method was developed to mitigate the uncertainty of selecting an integration method to use with force-based

frame elements. The integration points at the element ends took on characteristic lengths specified by an analyst in order to regularize localized response in the presence of strain-softening behavior. At the same time, a convergent solution was maintained for the spread of plasticity due to strain-hardening behavior.

- For interpolation quadrature, finite difference computations verified the implementation of the analytic sensitivity equations was correct and a first order reliability analysis demonstrated that fewer limit state function evaluations were required when using analytic gradients in the search for the most probable point of failure.
- Rankings showed integration parameters had relatively low importance in reliability analysis when compared to material constitutive parameters. These developments allowed the epistemic uncertainty of selecting a force-based integration to be quantified, as well as permitting integration points and weights to be treated as random variables in a probabilistic structural analysis.

APPENDICES

Appendix A – AASHTO-MCFT Capacity Function

The sectional shear-moment interaction diagram in MB is calculated using the spreadsheets [16] and implemented within *AASHTO-MCFT* function to OpenSees framework. This function calculates the shear strength for a beam having at least minimum amount of vertical reinforcement in it.

The nominal shear resistance of conventionally reinforced concrete members in AASHTO-LRFD is determined as the lesser of:

$$V_n = V_c + V_s \quad (\text{A.1a})$$

$$V_n = 0.25f'_c b_w d_v \quad (\text{A.1b})$$

The concrete and steel contributions are formulated as:

$$V_c = \beta^* \sqrt{f'_c} b_w d_v \quad (\text{A.2a})$$

$$V_s = \frac{A_v f_y d_v \cot(\theta^*)}{s} \quad (\text{A.2b})$$

while d_v is the effective shear depth; β^* is the factor indicating ability of diagonally cracked concrete to transmit tension and θ^* is the inclination of diagonal compressive stresses.

For sections with at least minimum stirrups, an MCFT based approach is adopted in in Article 5.8.3.4 of AASHTO-LRFD. Values of β^* and θ^* are obtained for the corresponding longitudinal strain at the mid-depth of the member when the section is subjected to ultimate section forces M_u , V_u and N_u as shown

in Fig. A.1. The method computes these forces for various values of the longitudinal strain, ε_x , to determine the shear-moment interaction diagram. The idealized section consists of three regions, flexural tension, flexural compression and web. Once the diagonal cracks occur in the web at the crack angle θ^* , the diagonal compression force causes a longitudinal force on the web $V_u \cot \theta^*$. Equilibrium is maintained with tension forces distributed on flanges equally. Table (5.8.3.4.2-1) of AASHTO-LRFD displaying the values of β^* and θ^* for corresponding shear stress and longitudinal strain is applied to the *AASHTO_MCFT* function code as shown in Fig. A.2.

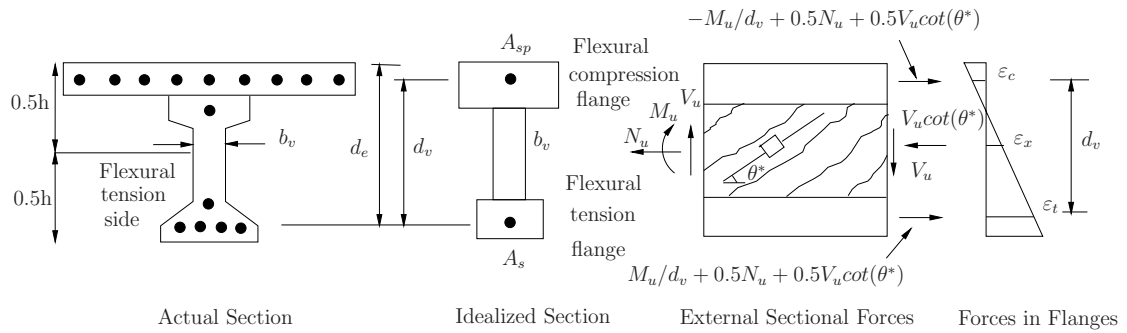


Figure A.1: AASHTO ultimate shear-moment calculation procedure

The arrays, *sxe_ex* and *v_fpc_ex*, contain the longitudinal strain values multiplied by 1000 and the shear stress ratio V_u/f'_c . The next step is computing the level of stirrups that would be required for each cell of the $\beta^* - \theta^*$ chart.

Once the required values are obtained, each $\beta^* - \theta^*$ couple is interpolated from the code charts based on the level of stirrups provided and the required level. The provided (input) stirrup is calculated in the form:

$$stirrups = \frac{A_v f_{yv}}{b_w s} \quad (A.3)$$

```

const float sxe_ex[11] = {-0.2f, -0.1f, -0.05f, 0.0f, 0.125f, 0.25f, 0.5f, 0.75f, 1.0f, 1.5f, 2.0f};
const float v_fpc_ex[8] = {0.075f, 0.1f, 0.125f, 0.15f, 0.175f, 0.2f, 0.225f, 0.25f};

const float Theta[8][11] = {
    {22.3f, 20.4f, 21.0f, 21.8f, 24.3f, 26.6f, 30.5f, 33.7f, 36.4f, 40.8f, 43.9f},
    {18.1f, 20.4f, 21.4f, 22.5f, 24.9f, 27.1f, 30.8f, 34.0f, 36.7f, 40.8f, 43.1f},
    {19.9f, 21.9f, 22.8f, 23.7f, 25.9f, 27.9f, 31.4f, 34.4f, 37.0f, 41.0f, 43.2f},
    {21.6f, 23.3f, 24.2f, 25.0f, 26.9f, 28.8f, 32.1f, 34.9f, 37.3f, 40.5f, 42.8f},
    {23.2f, 24.7f, 25.5f, 26.2f, 28.0f, 29.7f, 32.7f, 35.2f, 36.8f, 39.7f, 42.2f},
    {24.7f, 26.1f, 26.7f, 27.4f, 29.0f, 30.6f, 32.8f, 34.5f, 36.1f, 39.2f, 41.7f},
    {26.1f, 27.3f, 27.9f, 28.5f, 30.0f, 30.8f, 32.3f, 34.0f, 35.7f, 38.8f, 41.4f},
    {27.5f, 28.6f, 29.1f, 29.7f, 30.6f, 31.3f, 32.8f, 34.3f, 35.8f, 38.6f, 41.2f} };

const float Beta[8][11] = {
    {6.32f, 4.75f, 4.10f, 3.75f, 3.24f, 2.94f, 2.59f, 2.38f, 2.23f, 1.95f, 1.67f},
    {3.79f, 3.38f, 3.24f, 3.14f, 2.91f, 2.75f, 2.50f, 2.32f, 2.18f, 1.93f, 1.69f},
    {3.18f, 2.99f, 2.94f, 2.87f, 2.74f, 2.62f, 2.42f, 2.26f, 2.13f, 1.90f, 1.67f},
    {2.88f, 2.79f, 2.78f, 2.72f, 2.60f, 2.52f, 2.36f, 2.21f, 2.08f, 1.82f, 1.61f},
    {2.73f, 2.66f, 2.65f, 2.60f, 2.52f, 2.44f, 2.28f, 2.14f, 1.96f, 1.71f, 1.54f},
    {2.63f, 2.59f, 2.52f, 2.51f, 2.43f, 2.37f, 2.14f, 1.94f, 1.79f, 1.61f, 1.47f},
    {2.53f, 2.45f, 2.42f, 2.40f, 2.34f, 2.14f, 1.86f, 1.73f, 1.64f, 1.51f, 1.39f},
    {2.39f, 2.39f, 2.33f, 2.33f, 2.12f, 1.93f, 1.70f, 1.58f, 1.50f, 1.38f, 1.29f} };

```

Figure A.2: $\beta^* - \theta^*$ values for longitudinal strain ε_x

```

float Vtable[8];
for (int i = 0; i < 8; i++)
    Vtable[i] = v_fpc_ex[i]*fpc;

float RequiredStirrups[8][11];
for (int i = 0; i < 8; i++)
    for (int j = 0; j < 11; j++)
        RequiredStirrups[i][j] = (Vtable[i]-Beta[i][j]*sqrt(fpc))*tan(Theta[i][j]/57.3f);

```

Figure A.3: The level of required Stirrups for each $\beta^* - \theta^*$ cell

```

float finalTheta[11];
float yieldTheta = 0.0;
for (int i = 0; i < 11; i++) {
    // Initialize
    finalTheta[i] = 0.0;

    // Minimum value
    if (stirrups < RequiredStirrups[0][i])
        finalTheta[i] = Theta[0][i];

    // Normal values
    for (int j = 0; j < 7; j++)
        if (stirrups >= RequiredStirrups[j][i] && stirrups < RequiredStirrups[j+1][i])
            finalTheta[i] = Theta[j+1][i] - (Theta[j+1][i] - Theta[j][i]) * (RequiredStirrups[j+1][i] - stirrups)
                               / (RequiredStirrups[j+1][i] - RequiredStirrups[j][i]);

    // Maximum value
    if (stirrups > RequiredStirrups[7][i])
        finalTheta[i] = Theta[7][i];

    if (finalTheta[i] > yieldTheta)
        yieldTheta = finalTheta[i];
}

float finalBeta[11];
for (int i = 0; i < 11; i++) {
    // Initialize
    finalBeta[i] = 0.0;

    // Minimum value
    if (stirrups < RequiredStirrups[0][i])
        finalBeta[i] = Beta[0][i];

    // Normal values
    for (int j = 0; j < 7; j++)
        if (stirrups >= RequiredStirrups[j][i] && stirrups < RequiredStirrups[j+1][i])
            finalBeta[i] = Beta[j+1][i] - (Beta[j+1][i] - Beta[j][i]) * (RequiredStirrups[j+1][i] - stirrups)
                               / (RequiredStirrups[j+1][i] - RequiredStirrups[j][i]);

    // Maximum value
    if (stirrups > RequiredStirrups[7][i])
        finalBeta[i] = Beta[7][i];
}

```

Figure A.4: The interpolation of $\beta^* - \theta^*$ values

For each ε_x level, the new $\beta^* - \theta^*$ values are interpolated regarding the location of provided stirrup level in the required stirrups table. The procedure interpolating $\beta^* - \theta^*$ values are shown in Fig. A.4. The concrete and steel contributions in shear strength, V_u , are calculated using the final $\beta^* - \theta^*$ values, Eqs. (A.2a) and (A.2b). The shear strength, V_u is controlled with the limit value given in Eq. (A.1b). The corresponding moment strength, M_u is determined using the longitudinal strain

approximation in Article 5.8.3.4.2 of AASHTO-LRFD having the form:

$$\varepsilon_x = \frac{\frac{M_u}{d_v} + 0.5N_u + 0.5V_u \cot(\theta^*)}{E_s A_s} \quad (\text{A.4})$$

The extracted moment values are controlled with the moment value if the strain causes the longitudinal reinforcement yield having the form:

$$M_y = \frac{\left(A_s f_{yl} - \frac{(V_u - 0.5V_s)}{\tan(\theta_y^*)} \right)}{d_v} \quad (\text{A.5})$$

The calculation of moment strength considers three controlling points when the longitudinal yield is dominant:

- The maximum moment sustained at the shear associated with $\varepsilon_x > 0.002$.

$$M_u = M_y \quad (\text{A.6})$$

- The maximum moment sustained at a shear of $V_s/2$ is equal to the the pure flexural capacity.

$$M_u = \frac{A_s f_y}{d_v} \quad (\text{A.7})$$

- The pure flexural capacity at zero shear using the same equation Eq. (A.7).

The procedure for the computation of calculated M-V points and the extraction as an output in an array is shown in Fig. A.5. However, AASHTO has a limit that the M_u in equations not be taken as less than $V_u d_v$. In particular, at locations of low moment, only shear is providing a force in the tension and compression flange to resist. If the flexural tension demands resulting from shear are larger

than the flexural compression demands from the bending, the flexural compression side of the section can crack. This can result in the wrong flange cracking and thus the epsilon-x equation will underestimate the expected straining. To avoid this problem AASHTO limits the shear strength with a cap value where $V_u = M_u/d_v$.

```
float Vc, Vs;
float Vlim = 0.25f*fpc*bw*dv/1000.0f;
float moment, longYield, tmpFe;
float M[14];
float V[14];
float MoverV[14];
for (int i = 0; i < 11; i++) {
    Vc = finalBeta[i]*sqrt(fpc)*dv*bw/1000.0f;
    Vs = (stirrups/tan(finalTheta[i]/57.32f))*dv*bw/1000.0f;
    V[i] = (Vc+Vs < Vlim) ? Vc+Vs : Vlim;
    tmpFe = (sxe_ex[i] < 0.0f) ? 0.5f*Fe : 0.5f;
    moment = (sxe_ex[i]*EsAs/1000.0f/tmpFe-0.5f*V[i]/tan(finalTheta[i]/57.3f))*dv/12.0f;
    longYield = (Asfy-(V[i]-0.5f*Vs)/tan(yieldTheta/57.3f))*dv/12.0f;
    M[i] = (moment < longYield) ? moment : longYield;
    MoverV[i] = M[i]/V[i];
}

V[11] = V[10];
M[11] = longYield;
V[12] = Vs/2.0f + 0.1f;
M[12] = (Asfy-(0.1f)/tan(finalTheta[10]/57.3f))*dv/12.0f;
V[13] = 0.2f;
M[13] = Asfy*dv/12.0f;
```

Figure A.5: Computation of M-V points of interaction diagram

However, the shear cap value may not coincide with any computed points of the interaction diagram; thus an interpolation is needed to compute ultimate shear and moment. A procedure interpolates β^* , θ^* and ε_x values between two intervals of M/V ratio as shown in Fig. A.6. The $\beta^* - \theta^*$ values in AASHTO provide corresponding strains in shear dominant region where θ does not exceed 45° . However, M/V ratio may match d_v out of this $\beta^* - \theta^*$ interval where the behavior is controlled by yielding of longitudinal reinforcement and the interpolation of $\beta^* - \theta^*$ is not available. Thus, the procedure uses an analytical formulation that computes shear cap value in terms of the ultimate moment value and the lowest shear

strength obtained using Eq. (A.2).

```

for (int i = 0; i < 13; i++) {
    if (i < 10) {
        if (MoverV[i] < dv12 && MoverV[i+1] > dv12) {

            betastep = (finalBeta[i]-finalBeta[i+1])/50; //beta increment
            thetastep = (finalTheta[i+1]-finalTheta[i])/50; //theta increment
            exstep = (sxe_ex[i+1]-sxe_ex[i])/50; //strain increment
            cbeta = finalBeta[i]; //beta start
            ctheta = finalTheta[i]; //theta start
            cex = sxe_ex[i]; //strain start

            for (int j = 1; j < 50; j++) {
                Bp = cbeta - betastep*j; //trial beta
                Tp = ctheta + thetastep*j; //trial theta
                ep = cex + exstep*j; //trial strain
                Vcinter = Bp*sqrt(fpc)*dv*bw/1000.0f; //Vc
                Vsinter = (stirrups/tan(Tp/57.32f))*dv*bw/1000.0f; //Vs
                shear = Vcinter + Vsinter; //total shear strength
                shear = (Vcinter+Vsinter < Vlim) ? Vcinter+Vsinter : Vlim;
                //check maximum shear strenght
                tmpFe = (ep < 0.0f) ? 0.5f*Fe : 0.5f;
                moment = (ep*EsAs/1000.0f/tmpFe-0.5f*shear/tan(Tp/57.3f))*dv/12.0f; //Mu
                clongYield = (Asfy-(shear-0.5f*Vsinter)/tan(yieldTheta/57.3f))*dv/12.0f;
                //yielding moment at Vu
                moment = (moment < clongYield) ? moment : clongYield;
                //check Mu against Myielding
                float ratt = moment/shear;
                if (moment / shear > dv12){
                    break; // stop if MoverV > dv
                }
            }

        } else {

            if (MoverV[i] < dv12 && MoverV[i+1] > dv12) {
                m = (V[i]-V[i+1])/(M[i]-M[i+1]); // slope MV line
                b = ((V[i]+V[i+1])-m*(M[i]+M[i+1]))/2.0f; // interpolation step
                moment = b/(1/dv12-m); //Mu at shear cap
                shear = moment/dv12; //Vu at shear cap
            }
        }
    }
}

```

Figure A.6: Shear cap computation: Interpolation of M-V points

Appendix B – Multi-Beta (MB) Capacity Function

Five-line representation of AASHTO-MCFT interaction diagram is implemented in reliability analysis using using a Tcl procedure. The function *AASHTO_MCFT* computes the coordinates of interaction diagram of section for one direction of bending moment. The proposed Tcl procedure *getMV* employs *AASHTO_MCFT* function with two given longitudinal reinforcements, A_s^+ and A_s^- to compute nominal flexural resistance in both directions. The input variables and the output line equation are shown in Fig. B.1. The extracted parameters, cm , cn and cv are the coefficient of moment, the constant value and the coefficient of shear in M-V space line equation.

```
proc getMV {fc0 fylong0 d0 bw0 Asneg0 Av0 fytrans0 s0 Aspos0 Es0 beff0 pf} {
    :
    :
    set BetaArray "$cm $cn $cv"
    return $BetaArray
}
```

Figure B.1: The body of function *getMV*

In procedure, the operations start the with the effective depth, d_v , calculations for positive and negative moment. The distance is defined as the length between reinforcing steel and the center of rectangular concrete compression zone. However, the AASHTO code [3] requires that the value need not be taken less than 90% of the distance from the edge of the section to the location of reinforcing steel or 72% of the total depth. The procedure code for the positive and negative moment

effective depth is shown in Fig. B.2.

After the effective depth operation is completed, the Tcl procedure calls the *AASHTO_MCFT* function for negative and positive bending moment. However, two shear strength is calculated for the same section. For a logical solution the higher shear strength is considered as the shear limit. All coordinates of M-V diagram points are saved in the array *MV* as shown in Fig. B.3.

The number of points in *MV* array varies from eleven to fourteen points. MB limit state demonstrates the interaction diagram with five critical lines to reduce the computation effort of high order representation, so that a reduction in points array needs to be coded. The reduced array contain the M-V point location in critical shear and flexural points. The performance functions g_1 and g_5 are equal to positive and negative moment capacity while the shear cap is the horizontal line equation g_3 . The line g_4 connects the shear cap to the pure moment limit at $V_u/2$ where M_u is equal to the ultimate moment. The location of shear cap is decided whether it is on negative or positive x-axis regarding to the sign of strong bending moment capacity. The procedure for five line representation and extraction of the line equation parameters are shown in Fig. B.4.

```

#DvPos - Effective depth - positive moment
set ds [expr $d0-$dflange]
set al [expr $Aspos0*$fylong0/$beta/$fc0/$beff0]
if { $al > $hf } {
  set al [expr ($Aspos0*$fylong0-($beff0-$bw0)*$hf*$fc0*$beta)/$bw0/$fc0/$beta ]
  set dvposA [expr $ds - ($beff0*$hf0*$hf0+($al*$al-$hf0*$hf0)*$bw0)/($beff0*$hf0+($al-$hf0)*$bw0)]
} else {
  set dvposA [expr $ds - $al / 2 ];
}
if { $yrebar >= $al } {
  set dvposB [expr 0.90*$ds]; set dvposC [expr 0.72*$d0]
  if { $dvposA > $dvposB && $dvposA > $dvposC } {
    set dvpos $dvposA
  } elseif { $dvposB > $dvposA && $dvposB > $dvposC } {
    set dvpos $dvposB
  } elseif { $dvposC > $dvposB && $dvposC > $dvposA } {
    set dvpos $dvposC
  }
} else {
  set Acs $Asneg0
#check stress on compressed rebar
  set EpsAcs [ expr 0.003* ( $al/$beta-$yrebar ) / ( $al/$beta ) ]
  if { $fylong0 / $Es0 } {
    set fAcs $fylong0
  } else {
    set fAcs [expr $EpsAcs*$Es0]]
  }
  set a2 [expr ($Asneg0*$fylong0-$Acs*$fAcs)/($beta*$fc0*$beff0)]
  if { $a2 > $hf } {
    set a2 [expr ($Aspos0*$fylong0-($beff0-$bw0)*$hf*$fc0*$beta)/$bw0/$fc0/$beta ]
    set dvposA [expr $ds - ($beff0*$hf0*$hf0+($al*$al-$hf0*$hf0)*$bw0)/($beff0*$hf0+($al-$hf0)*$bw0)]
  } else {
    set dvposA [expr $ds - $a2 / 2 ];
  }
}
set dvnegB [expr 0.90*$ds]; set dvnegC [expr 0.72*$d0]
if { $dvposA > $dvposB && $dvposA > $dvposC } {
  set dvpos $dvposA
} elseif { $dvposB > $dvposA && $dvposB > $dvposC } {
  set dvpos $dvposB
} elseif { $dvposC > $dvposB && $dvposC > $dvposA } {
  set dvpos $dvposC
}
}

#DvNeg - Effective depth - negative moment
set ds [expr $d0-$yrebar]
set al [expr $Asneg0*$fylong0/$beta/$fc0/$bw0]
if { $dflange >= $al } {
  set dvnegA [expr $ds - $al / 2 ]; set dvnegB [expr 0.90*$ds]; set dvnegC [expr 0.72*$d0]
  if { $dvnegA > $dvnegB && $dvnegA > $dvnegC } {
    set dvneg $dvnegA
  } elseif { $dvnegB > $dvnegA && $dvnegB > $dvnegC } {
    set dvneg $dvposB
  } elseif { $dvnegC > $dvnegB && $dvnegC > $dvnegA } {
    set dvneg $dvnegC
  }
} else {
  set Acs $Aspos0
#check stress on compressed rebar
  set EpsAcs [ expr 0.003* ( $al/$beta-$yrebar ) / ( $al/$beta ) ]
  if { $fylong0 / $Es0 } {
    set fAcs $fylong0
  } else {
    set fAcs [expr $EpsAcs*$Es0]]
  }
  set a2 [expr ($Aspos0*$fylong0-$Acs*$fAcs)/($beta*$fc0*$bw0)]
  set dvposA [expr $ds - $a2 / 2 ]; set dvposB [expr 0.90*$ds]; set dvposC [expr 0.72*$d0]
  if { $dvposA > $dvposB && $dvposA > $dvposC } {
    set dvpos $dvposA
  } elseif { $dvposB > $dvposA && $dvposB > $dvposC } {
    set dvpos $dvposB
  } elseif { $dvposC > $dvposB && $dvposC > $dvposA } {
    set dvpos $dvposC
  }
}
}

```

Figure B.2: Calculation of the effective depth for positive and negative moment

```

#Combine + and - Moment capacity
set MVpos [AASHTO_MCFT $fc1 $fylongl $dv1 $bw1 $As1 $Av1 $fytrans1 $s1]
set Npos [expr [llength $MVpos]/2]
set posStart 0
set negStart 0
set dv2 [expr $dvneg/$in]
set As2 [expr $Asneg0/$in/$in]

set MVneg [AASHTO_MCFT $fc1 $fylongl $dv2 $bw1 $As2 $Av1 $fytrans1 $s1]
set Nneg [expr [llength $MVneg]/2]

set Vpos [lindex $MVpos 1]
set Vneg [lindex $MVneg 1]

if {$Vpos > $Vneg} {
    incr negStart
} else {
    incr posStart
}

set MV {}
for {set i $negStart; set j $Nneg} {$i < $Nneg} {incr i; incr j -1} {
    set M [lindex $MVneg [expr 2*$j-2]]
    set V [lindex $MVneg [expr 2*$j-1]]
    lappend MV [expr -1*$M] $V
}

for {set i $posStart} {$i < $Npos} {incr i} {
    set M [lindex $MVpos [expr 2*$i]]
    set V [lindex $MVpos [expr 2*$i+1]]
    lappend MV $M $V
}

```

Figure B.3: The Tcl code combining M^+V and M^-V capacity

```

# Reduce MV array to 6 points
set AAA {}
set length [llength $MV]
for {set z 0} {$z < 4} {incr z} {
    lappend AAA [lindex $MV $z]
}
for {set z 3} {$z < [expr $length -2]} {incr z 2} {
    set temp1 [lindex $MV [expr $z-3]]
    set temp2 [lindex $MV [expr $z-2]]
    set temp3 [lindex $MV [expr $z-1]]
    set temp4 [lindex $MV [expr $z]]
    if {($temp3 == 0.0) && ($temp4 == $temp2)} {
        lappend AAA $temp1 $temp2 $temp3 $temp4
    }
}
for {set z 3} {$z < [expr $length-2]} {incr z 2} {
    set temp1 [lindex $MV [expr $z-3]]
    set temp2 [lindex $MV [expr $z-2]]
    set temp3 [lindex $MV [expr $z-1]]
    set temp4 [lindex $MV [expr $z]]
    if {($temp1 == 0.0) && ($temp4 == $temp2)} {
        lappend AAA $temp1 $temp2 $temp3 $temp4
    }
}
for {set z 4} {$z >= 1} {incr z -1} {
    lappend AAA [lindex $MV [expr $length - $z]]
}
set MV $AAA

set pointNo [expr [llength $MV]/2]
set betaNo [expr $pointNo-1]
#figure 2 points
set xx1 [expr $kip*$ft*[lindex $MV [expr 2*$pf-2]]]
set yy1 [expr $kip*[lindex $MV [expr 2*$pf-1]]]
set xx2 [expr $kip*$ft*[lindex $MV [expr 2*$pf]]]
set yy2 [expr $kip*[lindex $MV [expr 2*$pf+1]]]
#compute m-slope of the line
if {$xx1 == $xx2} {
    if {$xx1 < 0.0} {
        set cm 1.0
        set cv 0.0
        set cn [expr -1*$xx1]
    } else {
        set cm -1.0
        set cv 0.0
        set cn $xx1
    }
} elseif {$yy1 == $yy2} {
    set cm 0.0
    set cv -1.0
    set cn $yy1
} else {
    set cm [expr ($yy2-$yy1)/($xx2-$xx1)]
    set cn [expr $yy2 - $cm * $xx2]
    set cv -1.0
}
set BetaArray "$cm $cn $cv"
return $BetaArray

```

Figure B.4: The Tcl code computing parameters of limit state line equations

Appendix C – OpenSees Uniaxial Material: Concrete02

OpenSees library presents the hysteretic concrete material with a linear tension softening [93]. The constitutive model of uniaxial *Concrete02* material is shown in Fig. C.1. The characteristic parameters are compressive strength f_{pc} , strain at peak stress eps_{c0} , crushing strength f_{pcU} , strain at crushing eps_U , λ ratio between unloading slope at eps_U and initial slope E_0 , tensile strength f_t and tension softening stiffness E_{ts} . The initial slope for this model is taken as $E_0 = 2f_{pc}/eps_{c0}$.

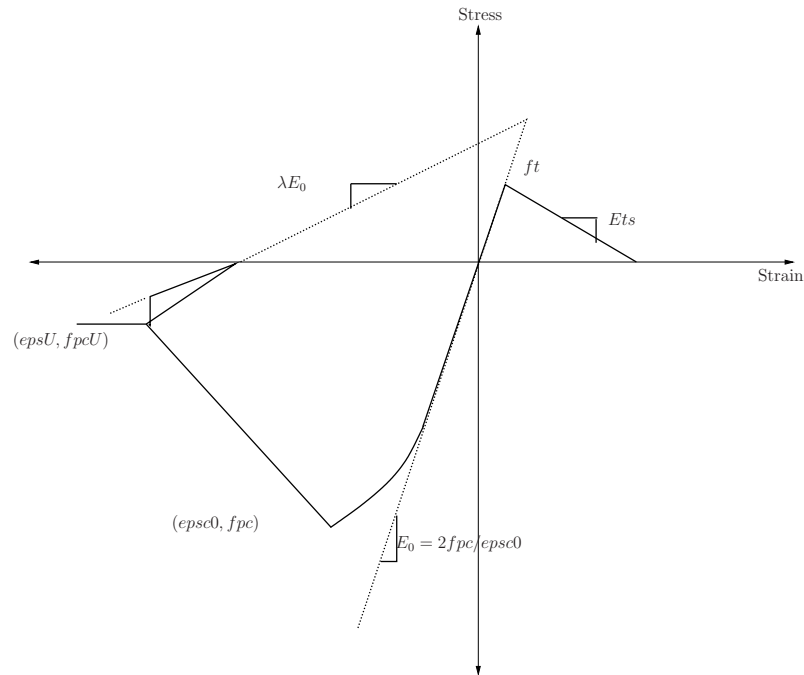


Figure C.1: Constitutive model of uniaxial Concrete02 material

Appendix D – OpenSees Uniaxial Material: Steel02

A uniaxial Giuffre-Menegotto-Pinto steel material model [34] with isotropic strain hardening is presented in OpenSees material library. The constitutive model of the uniaxial *Steel02* material is shown in Fig. D.1. The characteristic parameters are yield strength f_y , initial elastic tangent E_s , post-yield tangent E_p , the factor R controlling the transition from elastic to plastic branches. The recommended values are between 10 and 20. The value is taken as 15 in cyclic loading analysis of this study.

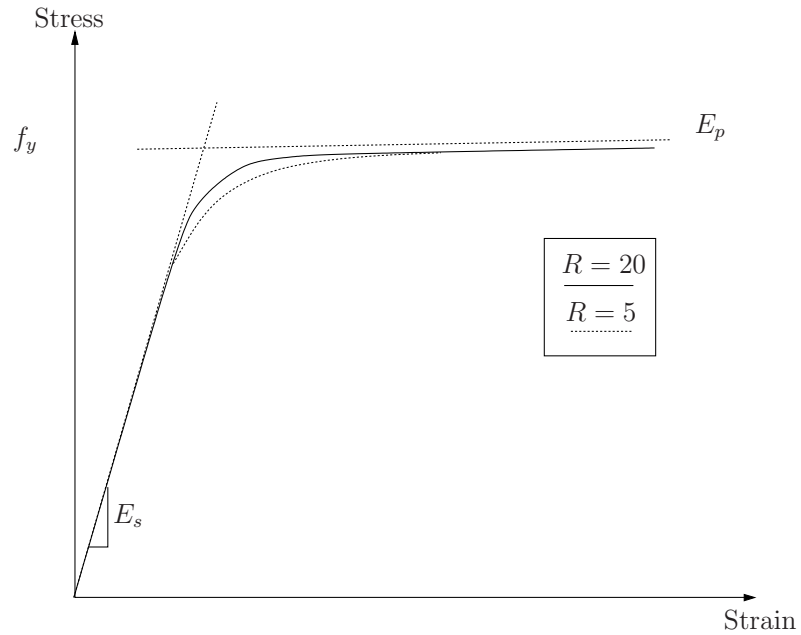


Figure D.1: Constitutive model of uniaxial Steel02 material

Appendix E – McKenzie River Bridge Girder Section Properties

In the live load reliability analysis of the McKenzie River Bridge girder, the section parameters of the interior girder are treated as uncertainties. The nominal values are taken as the mean values of variations in parameters. The section arrays shown in Fig. E.1 contains the mean values of parameter variations.

# Sections Properties #	fc (psi)	d (in)	bw (in)	fyl (ksi)	s (in)	As+ (in ²)	As- (in ²)	fyv (ksi)	Av (in ²)	beff (in)	hf (in)
#-----											
set Array_11	{3300.0	48	13.0	40	12	7.15	0.40	40	0.40	85.0	6.0 }
set Array_12	{3300.0	48	13.0	40	19	9.36	0.40	40	0.40	85.0	6.0 }
set Array_13	{3300.0	48	13.0	40	19	12.48	0.40	40	0.40	85.0	6.0 }
set Array_14	{3300.0	48	13.0	40	19	12.48	0.40	40	0.40	85.0	6.0 }
set Array_15	{3300.0	48	13.0	40	9	7.34	3.12	40	0.40	85.0	6.0 }
set Array_16	{3300.0	48	15.5	40	9	4.68	6.24	40	0.40	87.5	6.0 }
set Array_17	{3300.0	48	17.7	40	9	4.68	9.36	40	0.40	89.7	6.0 }
set Array_21	{3300.0	48	17.7	40	9	4.68	9.36	40	0.40	89.7	6.0 }
set Array_22	{3300.0	48	15.5	40	9	4.68	8.52	40	0.40	87.5	6.0 }
set Array_23	{3300.0	48	13.0	40	12	4.68	6.24	40	0.40	85.0	6.0 }
set Array_24	{3300.0	48	13.0	40	19	7.22	0.40	40	0.40	85.0	6.0 }
set Array_25	{3300.0	48	13.0	40	12	4.68	6.24	40	0.40	85.0	6.0 }
set Array_26	{3300.0	48	15.5	40	9	4.68	8.52	40	0.40	87.5	6.0 }
set Array_27	{3300.0	48	17.7	40	9	4.68	9.36	40	0.40	89.7	6.0 }
set Array_31	{3300.0	48	17.7	40	9	4.68	9.36	40	0.40	89.7	6.0 }
set Array_32	{3300.0	48	15.5	40	9	4.68	6.24	40	0.40	87.5	6.0 }
set Array_33	{3300.0	48	13.0	40	9	7.34	3.12	40	0.40	85.0	6.0 }
set Array_34	{3300.0	48	13.0	40	19	12.48	0.40	40	0.40	85.0	6.0 }
set Array_35	{3300.0	48	13.0	40	19	12.48	0.40	40	0.40	85.0	6.0 }
set Array_36	{3300.0	48	13.0	40	19	9.36	0.40	40	0.40	85.0	6.0 }
set Array_37	{3300.0	48	13.0	40	12	7.15	0.40	40	0.40	85.0	6.0 }

Figure E.1: Tcl arrays containing section properties

Bibliography

- [1] AASHTO. *LRFD Design Code for Highway Bridges*. American Association of State Highway and Transportation Officials, Washington, D.C., 1994.
- [2] AASHTO. *Manual for Condition Evaluation and Load and Resistance Factor Rating (LRFR) of Highway Bridges*. American Association of State Highway and Transportation Officials, Washington, D.C., 2003.
- [3] AASHTO. *LRFD bridge design specifications, 3rd Ed.* American Association of State Highway and Transportation Officials, Washington, D.C., 2004.
- [4] ABAQUS, Inc., Pawtucket, Rhode Island. *ABAQUS/Standard User's Manual – Version 6.6*, 2006. <http://www.hks.com>.
- [5] M. Abramowitz and C. A. Stegun, editors. *Handbook of Mathematical Functions with Formulas, Graphs, and Mathematical Tables*. Dover, New York, NY, 9th edition, 1972.
- [6] D. Addessi and V. Ciampi. A regularized force-based beam element with a plastic-damage section constitutive law. *International Journal for Numerical Methods in Engineering*, 70(5):610–629, 2007.
- [7] AISC. *Manual of Steel Construction, Load and Resistance Factor Design*. American Society of Steel Construction, Chicago, IL, 1986.
- [8] F. Akgul and D. M. Frangopol. Rating and reliability of existing bridges in a network. *Journal of Bridge Engineering*, 8(6):383–393, 2003.
- [9] B. N. Alemdar and D. W. White. Displacement, flexibility, and mixed beam-column finite element formulations for distributed plasticity analysis. *Journal of Structural Engineering*, 131(12):1811–1819, 2005.
- [10] ANSYS, Inc., Oxfordshire, UK. *ANSYS-CFX 5.6 User Manual*, 2003.
- [11] W. Aquino and I. Erdem. Implementation of the modified compression field theory in a tangent stiffness-based finite element formulation. *Journal of Steel and Composite Structures*, 7(4):263–278, 2007.

- [12] F. Armero and D. Ehrlich. Numerical modeling of softening hinges in thin euler-bernoulli beams. *Computers and Structures*, 84(10-11):641–656, 2006.
- [13] ASTM. *Standard specifications for highway weight-in-motion (WIM) systems with user requirements and test method (ASTM E 1318-02)*. American Society for Testing and Materials, Philadelphia, Pennsylvania, 2002.
- [14] Z. P. Bazant and B. H. Oh. Crack band theory for fracture of concrete. *Materials and Structures, RILEM*, 16:155–177, 1983.
- [15] Z. P. Bazant, J. Pan, and G. Pijaudier-Cabot. Softening in reinforced concrete beams and frames. *Journal of Structural Engineering*, 113(12):2333–2347, 1987.
- [16] E. C. Bentz. *Sectional Analysis of Reinforced Concrete Members*. PhD thesis, University of Toronto, Toronto, Canada, 2000.
- [17] P. Bjerager. Probability integration by directional simulation. *Journal of Engineering Mechanics*, 114(8):1285–1302, 1988.
- [18] G. Booch, J. Rumbaugh, and I. Jacobson. *The Unified Modeling Language User Guide*. Addison-Wesley, Reading, MA, 1998.
- [19] A. Borri and E. Speranzini. Structural reliability analysis using a standard deterministic finite element code. *Journal of Structural Safety*, 19(4):361–382, 1997.
- [20] CEC. *Eurocode 3: Steel Structuresm, Draft for National Comment (Report EUR 8849)*. Commission of the European Communities, 1984.
- [21] V. Ciampi and L. Carlesimo. A nonlinear beam element for seismic analysis of structures. In *8th European Conference on Earthquake Engineering*, Lisbon, Portugal, 1986.
- [22] R. W. Clough, K. L. Benuska, and E. L. Wilson. Inelastic earthquake response of tall buildings. In *Third World Conference on Earthquake Engineering*, Wellington, New Zealand, 1965.
- [23] J. Coleman and E. Spacone. Localization issues in force-based frame elements. *Journal of Structural Engineering*, 127(11):1257–1265, Nov. 2001.

- [24] Computers and Structures, Inc., Berkeley, California. *SAP2000 User's Manual – Version 10*, 2000.
- [25] J. P. Conte, P. K. Vijalapura, and M. Meghalla. Consistent finite-element response sensitivity analysis. *Journal of Engineering Mechanics*, 129(12):1380–1393, 2003.
- [26] C. A. Cornell. A probability-based structural code. *Journal of American Concrete Institute*, 66(12):974–985, 1969.
- [27] R. De Borst and H. B. Muhlhaus. Gradient-dependent plasticity: Formulation and algorithmic aspects. *International Journal for Numerical Methods in Engineering*, 35:521–539, 1992.
- [28] H. M. Deitel and P. J. Deitel. *C++ How to program*. Prentice-Hall, Upper Saddle River, NJ, 1998.
- [29] A. Der Kiureghian and M. De Stafano. Efficient algorithm for second-order reliability analysis. *Journal of Engineering Mechanics*, 117(12):2904–2923, 1991.
- [30] A. Der Kiureghian, T. Haukaas, and K. Fujimura. Structural reliability software at the university of california, berkeley. *Journal of Structural Safety*, 28:44–67, 2006.
- [31] A. Der Kiureghian and J. B. Ke. The stochastic finite element method in structural reliability. *Probabilistic Engineering Mechanics*, 3:83–91, 1988.
- [32] O. Ditlevsen and O. H. Madsen. *Structural Reliability Methods*. John Wiley & Sons, 1996.
- [33] C. E.-I. du Beton CEB. *CEB-FIB Model Code*. Thomas Telford Services, London, 1993.
- [34] C. E.-I. du Beton CEB. *RC elements under cyclic loading- State-of-the-art report*. Thomas Telford Services, Paris, 1996.
- [35] S. El-Tawil and G. G. Deierlein. Stress-resultant plasticity for frame structures. *Journal of Engineering Mechanics*, 124(12):1360–1370, 1998.

- [36] B. Ellingwood, T. V. Galambos, J. G. MacGregor, and C. A. Cornell. Development of a probability based load criterion for american national standard A58, NBS special publications SP577. Technical report, National Bureau of Standards, Washington, D.C, 1980.
- [37] M. P. Enright and D. M. Frangopol. Reliability-based condition assessment of deteriorating concrete bridges considering load redistribution. *Journal of Structural Safety*, 21:159–195, 1999.
- [38] A. C. Estes and D. M. Frangopol. Load rating versus reliability analysis. *Journal of Structural Engineering*, 131(5):843–847, 2005.
- [39] F. C. Filippou and A. Saritas. A beam finite element for shear-critical rc beams. *ACI Special Publication*, 237(19):295–310, 2006.
- [40] D. M. . Frangopol, Y. Ite, E. Spacone, and I. Iwaki. A new look at reliability of reinforced concrete columns. *Journal of Structural Safety*, 18(2):123–150, 1996.
- [41] E. Gamma, R. Helm, R. Johnson, and J. Vlissides. *Design Patterns: Elements of Reusable Object-Oriented Software*. Addison-Wesley, Reading, MA, 1995.
- [42] W. Gautschi. *On the construction of gaussian quadrature rules from modified moments*. Mathematics of Computation, 1970.
- [43] M. . Ghosn and F. Moses. Markov renewal model for maximum bridge loading. *Journal of Engineering Mechanics*, 111(9):1093–1104, 1985.
- [44] M. Ghosn, F. Moses, and J. Wang. Design of highway bridges for extreme events. Technical Report NCHRP 489, National Cooperative Highway Research Program, New York, NY, 2003.
- [45] M. F. Giberson. *The Response of Nonlinear Multistory Structures Subjected to Earthquake Excitation*. PhD thesis, California Institute of Technology, Pasadena, CA, 1967.
- [46] G. H. Golub and C. F. Van Loan. *Matrix Computations*. Johns Hopkins University Press, 3rd edition, 1996.
- [47] G. H. Golub and J. H. Welsch. *Calculation of gauss quadrature rules*. Mathematics of Computation, 1969.

- [48] N. T. Gridgeman. Lamé ovals. *Math. Gaz.*, 54:31–37, 1970.
- [49] K. R. Gurley, A. Kareem, and M. A. Tognarelli. Simulation of a class of non-normal random processes. *International Journal of Nonlinear Mechanics*, 31(5):601–617, 1996.
- [50] I. Hacking. *The Emergence of Probability*. Cambridge University Press, Cambridge, 1975.
- [51] A. Haldar and S. Mahadevan. *Reliability Assessment Using Stochastic Finite Element Analysis*. John Wiley & Sons, 2000.
- [52] O. M. Hamutcuoglu and M. H. Scott. Finite element reliability analysis of bridge girders considering moment-shear interaction. *Journal of Structural Safety*, 31(5):356–362, 2009.
- [53] S. M. Hashemiparast, M. Masjed-Jamei, and M. Deghan. On selection of the best coefficients in interpolatory quadrature rules. *Applied Mathematics and Computations*, 182(1):1240–1246, 2006.
- [54] A. Hasofer and N. Lind. An exact and invariant first-order reliability format. *Journal of Engineering Mechanics ASCE*, 100(1):111–121, 1974.
- [55] T. Haukaas and A. Der Kiureghian. Parameter sensitivity and importance measures in nonlinear finite element reliability analysis. *Journal of Engineering Mechanics*, 131(10):1013–1026, 2005.
- [56] T. Haukaas and A. Der Kiureghian. Strategies for finding the design point in non-linear finite element reliability analysis. *Probabilistic Engineering Mechanics*, 21(2):133–147, 2006.
- [57] T. Haukaas and A. Der Kiureghian. Methods and object-oriented software for fe reliability and sensitivity analysis with application to a bridge structure. *Journal of Computing in Civil Engineering*, 21(3):151–163, 2007.
- [58] T. Haukaas and A. D. Kiureghian. Finite element reliability and sensitivity methods for performance-based earthquake engineering. Technical Report PEER-2003/14, Pacific Earthquake Engineering Research Center, University of California, Berkeley, 2004.

- [59] T. Haukaas and M. H. Scott. Shape sensitivities in the reliability analysis of nonlinear frame structures. *Computers and Structures*, 84(15–16):964–977, 2006.
- [60] C. Higgins, T. K. Daniels, D. V. Rosowsky, T. H. Miller, and S. C. Yim. Assessment and risk ranking of conventionally reinforced concrete bridges for shear. *Journal of the Transportation Research Board*, 1928:110–117, 2005.
- [61] C. Higgins, T. H. Miller, D. Rosowsky, S. C. Yim, T. Potisuk, T. K. Daniels, B. S. Nicholas, M. J. Robelo, A.-Y. Lee, and R. W. Forrest. Assessment methodology for diagonally cracked reinforced concrete deck girders. Technical Report Rep. No. FHWA-OR-RD-05-04, Federal Highway Administration, Washington, D. C., 2004.
- [62] K. D. Hjelmstad and E. Taciroglu. Variational basis of nonlinear flexibility methods for structural analysis of frames. *Journal of Engineering Mechanics*, 131(11):1157–1169, 2005.
- [63] H. T. Hu and W. C. Schnobrich. Nonlinear analysis of cracked reinforced concrete. *ACI Structural Journal*, 87(2):199–207, 1990.
- [64] E. S. Hwang and A. S. Nowak. Simulation of dynamic load for bridges. *Journal of Structural Engineering*, 117(5):1413–1434, 1991.
- [65] L. F. Ibarra, R. A. Medina, and H. Krawinkler. Hysteretic models that incorporate strength and stiffness deterioration. *Earthquake Engineering and Structural Dynamics*, 34(12):1489–1511, 2005.
- [66] S. S. Isukapalli. *Uncertainty Analysis of Transport-Transformation Models*. PhD thesis, Rutgers Univ., Piscataway, NJ, 1999.
- [67] B. Jaishi and W. X. Ren. Structural finite element model updating using ambient vibration test results. *Journal of Structural Engineering*, 131(4):617–628, 2005.
- [68] M. Jirásek. Analytical and numerical solutions of localization in frame members with plastic hinges. *Journal of Engineering Mechanics*, 123(1):8–14, 1997.
- [69] A. J. Katz and H. Rakha. Field and modeling framework and case study of truck weight station operations. Technical report, University Transportation Center, Virginia Tech Transportation Institute, Blacksburg, VA, 2002.

- [70] D. C. Kent and R. Park. Flexural members with confined concrete. *Journal of the Structural Division, ASCE*, 97(7):1969–1990, 1971.
- [71] A. Kidarsa. Analysis of moving loads using force-based finite element, master's thesis, 2006.
- [72] A. Kidarsa, M. H. Scott, and C. C. Higgins. Analysis of moving loads using force-based finite elements. *Finite Elements in Analysis and Design*, 44(4):214–224, 2008.
- [73] W. Kijawatworawet, H. J. Pradlwarter, and G. I. Schuëller. Structural reliability estimation by adaptive importance directional sampling. In *Proceedings ICOSSAR 97 Structural Safety and Reliability*, Balkema, Rotterdam, 1998.
- [74] S. Kim and A. S. Nowak. Load distribution and impact factors for i-girder bridges. *Journal of Bridge Engineering*, 2(3):97–104, 1997.
- [75] T. H. Kim, Y. J. Kim, and H. M. Shin. Seismic performance assessment of reinforced concrete bridge columns under variable axial load. *Magazine of Concrete Research*, 59(2):87–96, 2007.
- [76] M. Kleiber, H. Antunez, T. D. Hien, and P. Kowalczyk. *Parameter Sensitivity in Nonlinear Mechanics*. John Wiley & Sons, 1997.
- [77] S. D. Koduru and T. Haukaas. Uncertain reliability index in finite element reliability analysis. *International Journal of Reliability and Safety*, 1(1/2):77–101, 2006.
- [78] D. E. Lehman and J. P. Moehle. Seismic performance of well-confined concrete bridge columns. Technical Report PEER 1998/01, Pacific Earthquake Engineering Research Center, Berkeley, CA, 2000.
- [79] I. Lichtenstein Consulting Engineers. Manual for condition evaluation and load rating of highway bridges using load and resistance factor philosophy. Technical Report Transportation Res. Board Project No. Report 12-46, Paramus, NJ, 2000.
- [80] S. Limkatanyu and E. Spacone. Reinforced concrete frame element with bond interfaces (ii): State determinations and numerical validation. *Journal of Structural Engineering*, 128(3):356–364, 2002.

- [81] P. L. Liu and A. Der Kiureghian. Multivariate distribution models with prescribed marginals and covariances. *Probabilistic Engineering Mechanics*, 1(2):105–112, 1986.
- [82] P. L. Liu and A. Der Kiureghian. Optimization algorithms for structural reliability. *Structural Safety*, 9(3):161–177, 1991.
- [83] Livermore Software Technology Corporation, Livermore, CA. *LS-DYNA Keyword Users Manual, Volumes 1 and 2, Version 970*, 2003.
- [84] D. G. Luenberger. *Introduction to Linear and Nonlinear Programming*. Addison Wesley, Reading, MA, 1986.
- [85] G. Lupoi, P. Franchin, A. Lupoi, and E. Pinto. Seismic fragility analysis of structural systems. *Journal of Engineering Mechanics*, 132(4):385–395, 2006.
- [86] A. C. Lynn, J. P. Moehle, S. A. Mahin, and W. T. Holmes. Seismic evaluation of existing reinforced concrete building columns. *Earthquake Spectra*, 12(4):715–739, Nov. 1996.
- [87] J. B. Mander, M. J. N. Priestley, and R. Park. Theoretical stress-strain model for confined concrete. *Journal of Structural Engineering*, 114(8):1804–1826, Aug. 1988.
- [88] M. E. Marante, R. Picon, and J. Florez-Lopez. Analysis of localization in frame members with plastic hinges. *International Journal of Solids and Structures*, 41:3961–3975, 2004.
- [89] A. Marini and E. Spacone. Analysis of reinforced concrete elements including shear effects. *ACI Structural Journal*, 103(5):645–655, 2006.
- [90] L. M. Massone, K. Orakcal, and J. Wallace. Shear - flexure interaction for structural walls. *ACI Special Publication SP-236 Deformation Capacity and Shear Strength of Reinforced Concrete Members Under Cyclic Loading*, pages 127–150, 2006.
- [91] S. Mazzoni, F. McKenna, M. H. Scott, and G. L. Fenves. *Open System for Earthquake Engineering Simulation User Command-Language Manual – Version 1.7.3*. University of California, Berkeley, CA, 2006. <http://opensees.berkeley.edu/OpenSees/manuals/usermanual/>.

- [92] M. D. McKay, R. J. Backman, and W. J. Conover. A comparison of three methods for selecting values of input variables in the analysis of output from a computer code. *Technometrics*, 21(2):239–245, 1979.
- [93] F. McKenna, G. L. Fenves, and M. H. Scott. *Open System for Earthquake Engineering Simulation*. University of California, Berkeley, CA, 2000. <http://opensees.berkeley.edu>.
- [94] R. E. Melchers. Importance sampling in structural systems. *Journal of Structural Safety*, 6:3–10, 1989.
- [95] M. Menegotto and P. E. Pinto. Method of analysis for cyclically loaded R.C. plane frames including changes in geometry and non-elastic behaviour of elements under combined normal force and bending. In *Symposium on the Resistance and Ultimate Deformability of Structures Acted on by Well Defined Repeated Loads*, pages 15–22, Zurich, Switzerland, 1973. International Association for Bridge and Structural Engineering.
- [96] C. Minervino, B. Sivakumar, F. Moses, D. Mertz, and W. Edberg. New aashto guide manual for load and resistance factor rating of highway bridges. *Journal of Bridge Engineering*, 9(1):43–54, 2004.
- [97] S. A. Mirza, M. Hatzinikolas, and J. G. MacGregor. Statistical descriptions of strength of concrete. *Journal of Structural Engineering*, 105(6):1021–1037, 1979.
- [98] S. A. Mirza and J. G. MacGregor. Variability of mechanical properties of reinforcing bars. *Journal of Structural Engineering*, 105(5):921–937, 1979.
- [99] S. A. Mirza and J. G. MacGregor. Variations in dimensions of reinforced concrete members. *Journal of Structural Engineering*, 105(4):751–766, 1979.
- [100] M. R. Moarafzadeh and R. E. Melchers. Directional importance sampling for ill-proportioned spaces. *Journal of Structural Safety*, 21:1–22, 1999.
- [101] Y. Mori and B. R. Ellingwood. Reliability-based service-life assessment of aging concrete structures. *Journal of Structural Engineering*, 119(5):1600–1621, 1993.
- [102] F. Moses. Bridge reliability concepts and methods. In *Bridge Safety and Reliability*, pages 1–22, Reston, VA, 1999. ASCE Publications.

- [103] A. Neuenhofer and F. C. Filippou. Evaluation of nonlinear frame finite-element models. *Journal of Structural Engineering*, 123(7):958–966, July 1997.
- [104] J. Nie and B. R. Ellingwood. Directional methods for structural reliability analysis. *Journal of Structural Safety*, 22:233–249, 2000.
- [105] B. G. Nielson and R. DesRoches. Seismic fragility methodology for highway bridges using a component level approach. *Earthquake Engineering and Structural Dynamics*, 36:823–839, 2007.
- [106] A. S. Nowak. Live load model for highway bridges. *Journal of Structural Safety*, 13.
- [107] A. S. Nowak. Calibration of lfrd bridge design code. Technical Report NCHRP 368, National Cooperative Highway Research Program, 1999.
- [108] A. S. Nowak and N. C. Lind. Practical bridge code calibration. *ASCE Journal of the Structural Engineering*, 5(12):2497–2510, 1979.
- [109] A. S. Nowak and J. Zhou. System reliability models for bridges. *Journal of Structural Safety*, 7:247–254, 1990.
- [110] M. of Transportation and Communications. *Ontario Highway Bridge Design Code*. Downsview, Ontario, Canada, 1983.
- [111] M. Ohue, H. Morimoto, S. Fujii, and S. Morita. The behavior of rc short columns failing in splitting bond-shear under dynamic lateral loading. *Transactions of the Japan Concrete Institute*, 7:293–300, 1985.
- [112] J. K. Ousterhout. *Tcl and the Tk Toolkit*. Addison-Wesley, 1994.
- [113] J. E. Padgett and R. DesRoches. Sensitivity of seismic response and fragility to parameter uncertainty. *Journal of Structural Engineering*, 133(12):1710–1718, 2007.
- [114] M. D. Patrick, X. S. Huo, J. A. Puckett, M. Jablin, and D. Mertz. Sensitivity of live load distribution factors to vehicle spacing. *Journal of Bridge Engineering*, 11:131–134, 2006.
- [115] T. Paulay and M. J. N. Priestley. *Seismic Design of Reinforced Concrete and Masonry Buildings*. Wiley, New York, NY, 1992.

- [116] M. Petrangeli and V. Ciampi. Equilibrium based iterative solutions for the nonlinear beam problems. *International Journal for Numerical Methods in Engineering*, 40:423–437, 1997.
- [117] M. Petrangeli, P. E. Pinto, and V. Ciampi. Fiber element for cyclic bending and shear of rc structures i: Theory. *Journal of Engineering Mechanics*, 125(9):994–1009, 1999.
- [118] J. A. Pincheira, F. S. Dotiwala, and J. T. D’Souza. Seismic analysis of older reinforced concrete columns. *Earthquake Spectra*, 15(2):245–272, May 1999.
- [119] E. Polak. *Optimization, Algorithms and Consistent Approximations (Applied Mathematical Sciences)*, volume 124. Springer, New York, NY.
- [120] S. Popovics. A numerical approach to the complete stress-strain curve of concrete. *Cement and Concrete Research*, 3(5):583–599, 1973.
- [121] T. Potisuk and C. Higgins. Field testing and analysis of crc deck girder bridges. *Journal of Bridge Engineering*, 12(1):53–63, 2007.
- [122] G. H. Powell and P. F. Chen. 3d beam-column element with generalized plastic hinges. *Journal of Engineering Mechanics*, 112:627–641, 1986.
- [123] J. A. Prozzi and F. Hong. Effect of weigh-in-motion system measurement errors on load pavement impact estimation. *Journal of Transportation Engineering*, volume = 133, number = 1, pages = 1–10, year = 2007.
- [124] R. Rackwitz and B. Fiessler. Structural reliability under combined random load sequence. *Computers and Structures*, 9:489–494, 1978.
- [125] G. Ranzo and M. Petrangeli. A fibre finite beam element with section shear modelling for seismic analysis of RC structures. *Journal of Earthquake Engineering*, 2(3):443–473, July 1998.
- [126] Research Engineers International, Bentley Solutions Center, Yorba Linda, California. *STAAD.Pro 2007 User’s Manual*, 2007.
- [127] M. Rosenblatt. Remarks on a multivariate transformation. *Annals of Mathematical Statistics*, 23:470–472, 1952.

- [128] M. Saatcioglu and M. Grira. Confinement of reinforced concrete columns with welded reinforcement grids. *ACI Structural Journal*, 1999(1):29–39, 1999.
- [129] M. H. Scott and G. L. Fenves. Plastic hinge integration methods for force-based beam-column elements. *Journal of Structural Engineering*, 132(2):244–252, Feb. 2006.
- [130] M. H. Scott, G. L. Fenves, F. T. McKenna, and F. C. Filippou. Software patterns for nonlinear beam-column models. *Journal of Structural Engineering*, 134(4):562–571, 2008.
- [131] M. H. Scott, P. Franchin, G. L. Fenves, and F. C. Filippou. Response sensitivity for nonlinear beam-column elements. *Journal of Structural Engineering*, 130(9):1281–1288, Sept. 2004.
- [132] H. Sezen. *Seismic Behavior and Modeling of Reinforced Concrete Building Columns*. PhD thesis, University of California, Berkeley, CA, 2002.
- [133] M. Software. *MSC.NASTRAN*. Santa Ana, CA, 2003. <http://www.mscsoftware.com>.
- [134] E. Spacone, V. Ciampi, and F. C. Filippou. Mixed formulation of nonlinear beam finite element. *Computers and Structures*, 58(1):71–83, 1996.
- [135] M. G. Stewart, D. V. Rosowsky, and D. V. Val. Reliability-based bridge assessment using risk-ranking decision analysis. *Journal of Structural Safety*, 23:397–405, 2001.
- [136] J. Stoer and R. Bulirsch. *Introduction to Numerical Analysis*. Springer-Verlag, New York, NY, 2nd edition, 1993.
- [137] B. Stroustrup. *The C++ Programming Language*. Addison-Wesley, 3rd edition, 1997.
- [138] Structural Research and Analysis Corporation, Los Angeles, CA. *Theoretical Manual*, 2001.
- [139] S. W. Tabsh and A. S. Nowak. Reliability of highway girder bridges. *ASCE Journal of Structural Engineering*, 117(8):2372–2388, 1991.

- [140] R. L. Taylor. FEAP: A finite element analysis program, version 7.5 user manual. Technical report, Structural Engineering, Mechanics and Materials, University of California, Berkeley, 2004. <http://www.ce.berkeley.edu/~rlt/feap>.
- [141] R. L. Taylor, F. C. Filippou, A. Saritas, and F. Auricchio. A mixed finite element method for beam and frame problems. *Computational Mechanics*, 31:192–203, 2003.
- [142] R. L. Taylor, J. C. Simo, O. C. Zienkiewicz, and A. C. Auricchio. The patch test: A condition for assessing finite element convergence. *International Journal for Numerical Methods in Engineering*, 22:39–62, 1986.
- [143] J. G. Teigen, D. M. Frangopol, S. Sture, and C. A. Felippa. Probabilistic fem for nonlinear concrete structure. i: Theory. *Journal of Structural Engineering*, 278(3):2674–2689, 1991.
- [144] P. Thoft-Christensen and M. J. Baker. *Structural Reliability Theory and Its Applications*. Springer-Verlag, 1982.
- [145] TNO DIANA, Rijswijk, the Netherlands. *DIANA Programmer's Manual – Version 9.2*, 2003.
- [146] O. T. Turan and C. Higgins. Statistical modeling of coupled shear-moment resistance for rc bridge girders. *Journal of Bridge Engineering*, 13:351–361, 2008.
- [147] J. F. Unger, A. Teughels, and G. D. Roeck. System identification and damage detection of a prestressed concrete beam. *Journal of Structural Engineering*, 132(11):1691–1698, 2006.
- [148] D. Val, F. Bljager, and D. Yankelevsky. Reliability evaluation in nonlinear analysis of reinforced concrete structures. *Journal of Structural Safety*, 19(2):203–217, 1997.
- [149] F. J. Vecchio. Towards cyclic load modeling of reinforced concrete. *ACI Structural Journal*, 96(2):193–203, 1999.
- [150] F. J. Vecchio. Disturbed stress field model for reinforced concrete: Formulation. *ASCE Journal of Structural Engineering*, 126(9):1070–1077, 2000.

- [151] F. J. Vecchio and M. P. Collins. The modified compression-field theory for reinforced concrete elements subjected to shear. *ACI Structural Journal*, 83(22):219–231, 1986.
- [152] F. J. Vecchio and M. P. Collins. Predicting the response of reinforced concrete beams subjected to shear using the modified compression field theory. *ACI Structural Journal*, 85(S27):258–268, 1988.
- [153] F. J. Vecchio and P. Wong. *VecTor2 and Formworks Manual*. Department of Civil Engineering, University of Toronto, Toronto, Ontario, Canada.
- [154] B. B. Welch. *Practical Programming in Tcl and Tk*. Prentice-Hall, 2000.
- [155] G. N. Wells, L. J. Sluys, and R. de Borst. Simulating the propagation of displacement discontinuities in a regularized strain-softening medium. *International Journal for Numerical Methods in Engineering*, 53:1235–1256, 2002.
- [156] S. Winterstein and P. Bjerager. The use of higher moments in reliability estimation. In *International Conference on Applications of Statistics and Probability*, number 2, pages 1027–1036, 1987.
- [157] Y. G. Zhao and Z. H. Lu. Fourth-moment standardization for structural reliability assessment. *Journal of Structural Engineering*, 133(7):916–924, 2007.
- [158] Y. G. Zhao, T. Ono, and M. Kato. Second-order third-moment reliability method. *Journal of Structural Engineering*, 128(8):1087–1090, 2002.
- [159] O. C. Zienkiewicz and R. L. Taylor. *The Finite Element Method: Volume 1, The Basis*. Butterworth-Heinman, Stoneham, MA, 5th edition, 2000.
- [160] T. Zimmermann, T. Simmermacher, and M. Kaouk. Model correlation and system health monitoring using frequency domain measurements. *Structural Health Monitoring*, 4(3):213–227, 2005.

